Measurement of the $t\bar{t}$ Production Cross Section in the Lepton Plus Jets Channel in $\bar{p}p$ Collisions at $\sqrt{s} = 1.8$ TeV

by

Chyi-Chang Miao

A dissertation submitted in partial fulfillment
of the requirements for the degree of
Doctor of Philosophy
(Physics)
in The University of Michigan
1997

Doctoral Committee:

Professor J. Wehrley Chapman, Chair
Associate Professor Dante Amidei
Professor Timothy Chupp
Professor Douglas O. Richstone
Professor York-Peng E. Yao

UMI Number: 9722041

To my family

ii

Acknowledgments

The writing of this dissertation would not have been possible without the effort made by members of CDF and the Fermilab Accelerator Division. They have my deep thanks.

I am very grateful to my advisor, J. Chapman, for his guidance throughout my graduate years. I appreciate the way that I have been educated and it sets a model for me to follow. My sincerest thanks go to Dan Amidei for introducing me to the top analysis. I was always benefited by his keen thoughts. I would also like to thank Dave Gerdes, who kindly and patiently guided me into the world of CDF. I feel I was so lucky to have had him here to work with on the XCES projects, and the early stages of my analysis.

My many thanks go to all the people in the Michigan/CDF/SDC group. Without them I wouldn't have felt in my graduate years to be as fruitful as they were. I would like to thank many colleagues of CDF: Paul, Karen, Weiming, Tony, Guillaume, Rob, and those in the b-tag and top cross section groups, who kindly shared the analysis experience to me in their own ways.

Thanks to Mom and Dad, who live far away but always support me with their love though I have not been able to comfort them in the years since I came to the States. Thanks to grandmom with whom I cannot share the joy of my graduation. My deep appreciation is due to my lovely wife Shwujing, who has been at my side during the happy and dark days in these years. Thanks to Vincent for pushing me forward in the final stage of my thesis. At the age of thirty, I am very fortunate to have been given so much to be thankful for.

iii

Table of Contents

v

List of Tables

List of Figures

xi

List of Appendices

Appendix

xiii

Chapter 1

Introduction

One of the most important experimental foundations of the Standard Model [1][2] was achieved with the direct observation of the top quark at the Tevatron proton-antiproton collider detectors [3][4]. The discovery of the top quark preserves the consistency of the orthodoxy of particle physics with the completion of the third generation fermion sector where the top quark is expected to accompany the bottom quark as the weak isospin doublet. Existence of the top quark was also inferred by several precision electroweak experiments made in the past decades. These include measurements of the forward backward asymmetry in $Z \to b\bar{b}$ using L3 detector at the CERN electron-positron collider LEP [5] and the absence of the flavor-changing neutral-current decays of the bottom quark using the CLEO detector at CESR [6]. Therefore, the search for the top quark became one of the major goals in particle physics.

In pursuit of the detection of the top quark, numerous efforts were made by independent experiments. A series of studies at the PEP and PETRA e^+e^- machines showed no evidence for the top quark in 1980s [7][8]. A Search for the decay $W \to t\bar{b}$ by the UA1 collaboration at the CERN $p\bar{p}$ collider [9] found no significant signals and set the lower limit of the top mass up to 44 GeV/c^2. The top quark remained unobserved in the early 1990s leading to an extension of the lower limit to 91 GeV/c^2 and 131 GeV/c^2 at the Tevatron colliders at Fermilab by the CDF and D0 groups respectively [10][11]. An upper limit for the top quark mass was also obtained by comparing all available data with electroweak

1

calculations under the Standard Model structure. Consideration of higher order corrections to ρ ($= M_W/M_Z cos\theta_W$) in the minimal Higgs model [12] gives an upper limit of 200 GeV/c^2. All of these indicate that if the top mass really lies in the allowed region implied by the previous experiments and calculations, many top quarks may be detected at Fermilab. Indeed in the spring of 1994, the Collider Detector at Fermilab reported the first direct evidence for the top quark, followed by the confirmation of the observation a year later with the top mass measured to be 176 GeV/c^2.

The top quark, as a result of its large mass provides not only tests of its properties, such as production rate, mass and V_{tb} element in the CKM matrix *etc.*, but also a powerful probe into several interesting phenomena. These include the searches for exotic decay modes with scalars as in multiple Higgs doublet schemes of the supersymmetric models, and signals of new resonances or gauge bosons which may favor strong coupling to the top quark. Among the quantities which can be measured at the Tevatron with the current data size, the top quark production cross section is one of the most inclusive quantities available to directly test the production mechanism modeled by the Standard Model.

The top quark search in the Collider Detector at Fermilab is established within the framework of the Standard Model assuming charged-current decays. Parton-parton collisions at the Tevatron produce top quark pairs with each subsequently decaying into a W boson and a b quark. For top quark mass greater than the sum of the masses of the W boson and the b quark, the W boson is real and decays either to a lepton and a neutrino, or a quark and an antiquark. Observation of the top quark can be categorized by the decay mode of the final state W^+W^- pair as shown in table 1.1. The fully hadronic final state, $t\bar{t}$ $\rightarrow$ $(q\bar{q}'b)(q\bar{q}'\bar{b})$, resulting from both W bosons decaying to a quark-antiquark pairs occurs 44% of the $t\bar{t}$ decays but is hard to detect due to huge QCD multijet background[13]. The second largest branching ratio, about 30% of the $t\bar{t}$ decays, corresponds to events in which one of the W boson decays leptonically to an e or μ, and the other hadronically, i.e., $t\bar{t}$ $\rightarrow$ $(q\bar{q}'b)(e\nu\bar{b})$, or $t\bar{t}$ $\rightarrow$ $(q\bar{q}'b)(\mu\nu\bar{b})$. The final state then includes a charged lepton with high transverse momentum and an energy imbalance from the undetected neutrino. The

2

Decay mode	Branching Ratio
$t\bar{t} \longrightarrow (q\bar{q}'b)(q\bar{q}'\bar{b})$	36/81
$t\bar{t} \longrightarrow (q\bar{q}'b)(e\nu\bar{b})$	12/81
$t\bar{t} \longrightarrow (q\bar{q}'b)(\mu\nu\bar{b})$	12/81
$t\bar{t} \longrightarrow (q\bar{q}'b)(\tau\nu\bar{b})$	12/81
$t\bar{t} \longrightarrow (e\nu b)(\mu\nu\bar{b})$	2/81
$t\bar{t} \longrightarrow (e\nu b)(\tau\nu\bar{b})$	2/81
$t\bar{t} \longrightarrow (\mu\nu b)(\tau\nu\bar{b})$	2/81
$t\bar{t} \longrightarrow (e\nu b)(e\nu\bar{b})$	1/81
$t\bar{t} \longrightarrow (\mu\nu b)(\mu\nu\bar{b})$	1/81
$t\bar{t} \longrightarrow (\tau\nu b)(\tau\nu\bar{b})$	1/81

Table 1.1: $t\bar{t}$ decay modes and approximate branching ratios in lowest order calculations. The symbol q stands for a light quark: u, d, c, s. The above table first appeared in published form in reference [3].

associated background in this channel can be reduced for events where either the b or $\bar{b}$ is identified by observation of a secondary vertex due to the nonzero b quark lifetime. This event topology is referred to as the "lepton plus jets" mode for the top quark search.

A measurement of $t\bar{t}$ production cross section described in this dissertation,

$$\sigma(p\bar{p} \longrightarrow t\bar{t} \longrightarrow W^{+}bW^{-}\bar{b} \longrightarrow l\nu bjj b)$$

is calculated using the relation:

$$\sigma = \frac{N - B}{\epsilon \cdot \int \mathcal{L} dt}$$

where N is the number of observed $t\bar{t}$ candidate events in the "lepton plus jets" channel produced in $p\bar{p}$ Collisions at $\sqrt{s} = 1.8\ TeV$, B is the expected background, ϵ is the total acceptance and $\int \mathcal{L} dt$ is the integrated luminosity. New physics would be indicated should any significant discrepancy between the theoretical calculations and experimental results be observed.

3

1.1 Motivation for Measurements

The theoretical prediction of the total cross section for the inclusive production of a top quark pair ($p\bar{p} \rightarrow t\bar{t}X$) is given by the formula [14]

$$\sigma(s) = \sum_{i,j} \int dx_1 dx_2 \hat{\sigma}_{ij}(x_1 x_2 s, m^2, \mu^2) F_i^p(x_1, \mu) F_j^{\bar{p}}(x_2, \mu)$$

where $F_{i(j)}^p$ are the densities of partons $i(j)$ in the proton, m is the top quark mass, $\sqrt{s}$ is the center-of-mass energy of the colliding hadrons p and $\bar{p}$, and μ is the factorization scale taken as coincident with the renormalization scale. The partonic cross section $\hat{\sigma}$, for inclusive production of a top quark pair from partons i, j can be written as,

$$\hat{\sigma}_{ij}(s, m^2, \mu^2) = \frac{\alpha_s^2(\mu^2)}{m^2} f_{ij}(\rho, \frac{\mu^2}{m^2})$$

with $\rho = 4m^2/s$. s is the square of the partonic center-of-mass energy. This is calculable using perturbative QCD (pQCD) due to the large value of the top quark mass. The dimensionless functions f_{ij} have the following perturbative expansion,

$$f_{ij}(\rho, \frac{\mu^2}{m^2}) = f_{ij}^{(0)}(\rho) + 4\pi\alpha_s(\mu^2)[f_{ij}^{(1)}(\rho) + \bar{f}_{ij}^{(1)}(\rho) ln(\mu^2/m^2)] + O(\alpha_s^2)$$

At lowest order of the strong coupling constant, the first term in the perturbative series corresponds to the Born contribution, i.e., the order $O(\alpha_s^2)$ contribution to the cross section. At this order there are two parton-parton subprocesses, quark-antiquark annihilation and gluon-gluon fusion, associated with non-zero functions $f_{q\bar{q}}^{(0)}$ and $f_{gg}^{(0)}$,

$$q + \bar{q} \rightarrow t + \bar{t}$$

and

$$g + g \rightarrow t + \bar{t}$$

where the Feynman diagrams are shown in figure 1.1. With a top mass above 100 GeV/c^2 in the range relevant to the Fermilab Tevatron energy, the total cross section for the $q\bar{q}$ annihilation process is expected to be much larger than that for gg fusion.

4
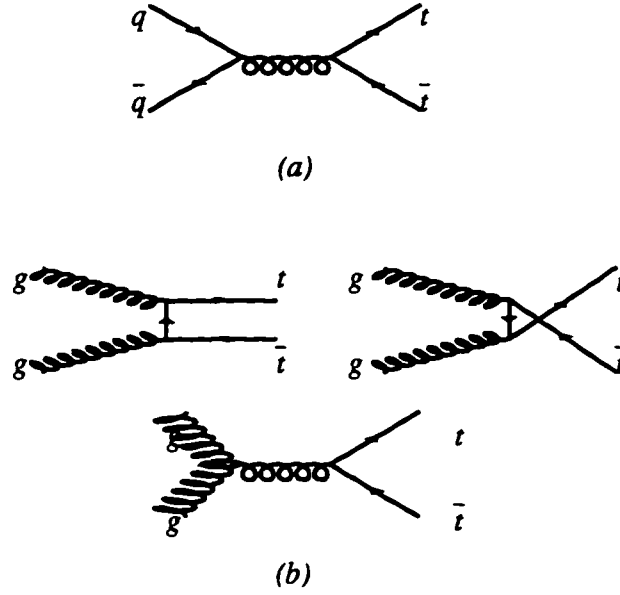
Figure 1.1: Feynman diagrams for the $t\bar{t}$ production via lowest order parton-parton subprocesses. (a) $q + \bar{q} \to t + \bar{t}$ (b) $g + g \to t + \bar{t}$

Next-to-leading (NLO) order $O(\alpha_s^3)$ contributions to the inclusive cross section have been taken into account with full $f^{(1)}$ and $\bar{f}^{(1)}$ calculations performed. This requires an examination of the cross section for the following parton-parton subprocesses:

$$q + \bar{q} \to t + \bar{t} + g$$

$$g + g \to t + \bar{t} + g$$

$$g + q \to t + \bar{t} + q$$

$$g + \bar{q} \to t + \bar{t} + \bar{q}$$

Throughout the top mass range relevant to Tevatron, it has been shown that $O(\alpha_s^3)$ in the gq and $\bar{q}g$ channels give negligible contributions, whereas those in the $q\bar{q}$ and gg channels should be included in the theoretical calculations [15]. Studies also show that the radiative corrections attributed to the gg channel are numerically as important as the lowest order $O(\alpha_s^2)$ contribution. Higher order contributions associated to the emission of multiple soft

5
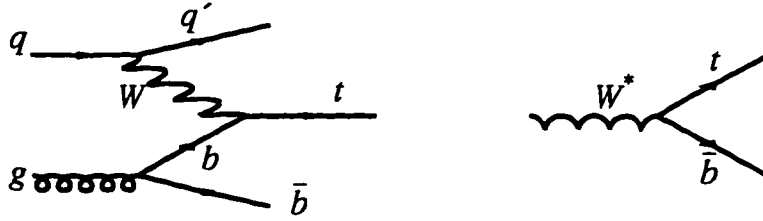
Figure 1.2: Feynman diagrams for single top production via Wg fusion and W^* decays.

gluons from the initial state have been also studied using resummation method to improve the calculations[16]. The current theoretical prediction for the $t\bar{t}$ production cross section at Tevatron is [17]

$$\sigma_{t\bar{t}} = 4.75^{+0.63}_{-0.68} \ pb \quad (M_{top} = 175\,GeV/c^2)$$

Experimental verification of this prediction is the primary topic of this dissertation.

Single top production at the Tevatron via W-gluon fusion $qg(W^+g) \to t\bar{b}X$ or W^* decays is also expected to occur[18] . The Feynman diagrams for the processes are shown in figure 1.2. Kinematic features of these events are W signal plus a central energetic b jet from top decay, another energetic jet from the recoiling light quark and a much softer b jet from the initial-state gluon-splitting. With the method of the search for $t\bar{t}$ signal described in this dissertation, it will be shown that the $t\bar{b}$ production rate is small and the contribution is less than at least one of the backgrounds for top masses accessible at Tevatron. Therefore the single top production via W-gluon fusion is not explicitly included in the following measurement for the $t\bar{t}$ production cross section.

1.2 Outline

This thesis summarizes the measurement of the $t\bar{t}$ production cross section using 110 pb^{-1} of $\bar{p}p$ Collisions at $\sqrt{s} = 1.8\ TeV$ collected with the Collider Detector at Fermilab between August of 1992 and February of 1996. The measurement focuses on the $t\bar{t}$ produc-

6

tion in the "lepton plus jets" decay mode where b-tagging is used to enhance the signal for $t\bar{t}$ events relative to the backgrounds by identification the bottom quark from the decay.

The remainder of this thesis is organized as follows. Chapter 2 describes briefly the experimental apparatus. An overview of both the CDF detector and Tevatron accelerator is presented. Among systems more attention will be given to the Silicon Vertex Detector which provides tracking information for reconstruction of the secondary vertices used to identify the b quark from the top quark decay.

The following chapters will be devoted to complete descriptions of the important steps leading to the top cross section measurement. Selection of the "lepton plus jets" events in $p\bar{p}$ collisions is described in the chapter 3. Chapter 4 details the tagging algorithm which is used to identify the b quark and the result of its application on the data sample. The efficiencies of the algorithm in both semileptonic and inclusive b decay modes are examined. An improved Monte Carlo program is then shown to be able to reproduce the tagging performance. Acceptance computation for the cross section measurement in the "lepton plus jets" channel and the integrated luminosity measurement are shown in chapter 5. Estimation of backgrounds to the $t\bar{t}$ production is reported in chapter 6. Results of the $t\bar{t}$ production cross section measurement described in this dissertation are summarized in chapter 7.

7

Chapter 2

Experimental Apparatus

The most energetic facility in the world for studies of particle interactions is located at the Fermi National Accelerator Laboratory (Fermilab) near Batavia, Illinois. The powerful Tevatron synchrotron [19] provides beams of particles used in a variety of experiments, both fixed-target and collider physics. During the period from June 1992 to February 1996, the Tevatron was committed to a collider run of $p\bar{p}$ collisions using its two collider detectors. The data collected at the Collider Detector at Fermilab during the period is used in this thesis.

An overview of the Tevatron and associated accelerators which provide the colliding beams is given below. Separately, the individual sub-systems of the detector are described, with particular emphasis on details of the components relating to the b quark identification used in the studies of $t\bar{t}$ decay.

2.1   Accelerators at Fermilab

Beams of protons and antiprotons can be accelerated to a laboratory frame energy of 900 GeV before being directed into collisions at the designed interaction regions. Production and acceleration of the particles takes place in several stages using different devices. Figure 2.1 shows the schematic view of these accelerators.

The beam of particles begin as charged hydrogen ions with one extra electron in a

8
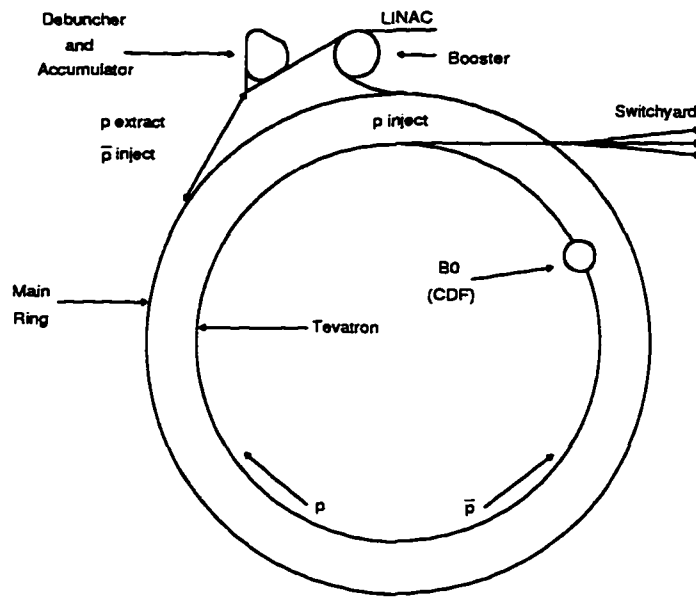
Figure 2.1: Schematic view of the accelerators at the Fermi National Accelerator Laboratory.

Cockcroft-Walton apparatus at the base of the Linac. The device provides the first stage of acceleration to an energy of 750 KeV by attracting the negative ions to a positive voltage. The negative ions then attain an energy of 400 MeV by the application of a periodic electric field inside spaced drift tubes of the 500 foot long linear accelerator (Linac) as indicated in the figure 2.1. A proton beam is obtained after the ions leave the Linac and pass through a carbon foil which removes their electrons. The Booster, a rapid cycling synchrotron located nearly 20 feet below ground, boosts the protons to an energy of 8 GeV. With several cycles in rapid succession, the Booster also separates the protons into discrete bunches and loads the pulses into the Main Ring.

The Main Ring is the upper ring of 1,000 conventional magnets located in the 6.3 km accelerator tunnel at Fermilab. In the Main Ring the protons can either be accelerated up to 150 GeV and injected into the final stage of acceleration process, the Tevatron, or be extracted from the ring after attaining an energy of 120 GeV in order to be used for

9

antiproton production. Antiprotons are among the secondary particles from the collisions between protons and a tungsten-rhenium target. Using the stochastic cooling process, these antiprotons are debunched and reduced in phase space. They are thus transferred to the Accumulator ring for storage and later injection back to the Main Ring.

The same tunnel which houses the Main Ring also contains a lower ring of super-conducting magnets, the Tevatron synchrotron. Superconducting magnets operated in the temperature range of liquid helium (-450°F) produce large magnetic fields required by the synchrotron. Both proton and antiproton which are passed down in bunches from the Main Ring are orbited and accelerated in opposite directions ($\bar{p}$ counter clockwise, p clockwise) to an energy of 900 GeV. The $p\bar{p}$ collisions take place at the B0 and D0 interaction regions where resides the two collider detectors at Fermilab.

2.2 Collider Detector at Fermilab

Located at the B0 interaction region on the accelerator ring, the Collider Detector at Fermilab (CDF) [20] is the first general-purpose detector built to explore the physics of $p\bar{p}$ collisions at a center-of-mass energy of 1.8 TeV. The collisions occur near the center of the CDF detector whose cylindrically symmetric design surrounds the colliding beams. Figure 2.2 shows a perspective view of the apparatus.

To accomplish the task of collecting the collision information as completely as possible, the interaction region is surrounded by layers of different detector components. A sideview [21] of the upper-east quadrant of the CDF detector is shown in figure 2.3. Detector components ordered by increasing distance from the interaction point are tracking systems, sampling calorimeters and muon detectors. Because the central region of the detector captures the fragments of the most interesting collisions, the highest resolution components are located in this area.

CDF uses a conventional right-handed coordinate system with the origin at the center of the detector. With the choice of the beamline as the Z axis, the azimuthal angle (ϕ) of the cylindrical system is measured from the north-pointing horizontal and the polar

10
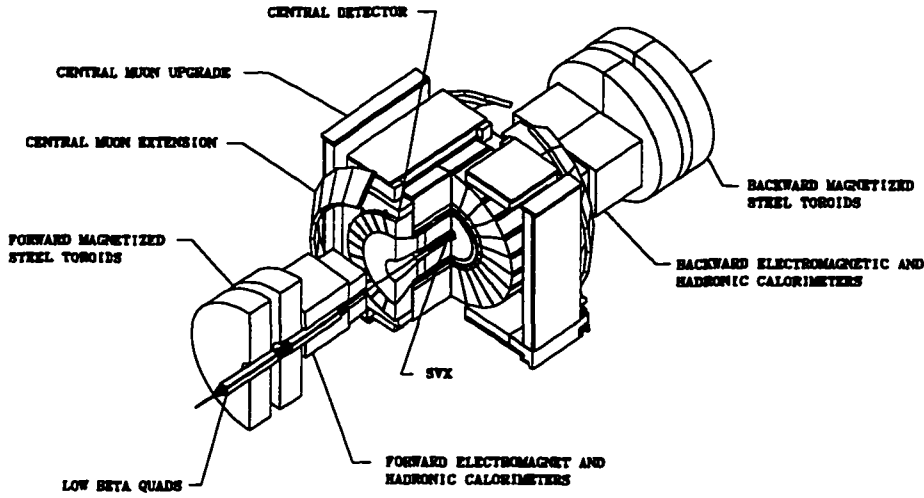
Figure 2.2: A perspective view of CDF detector.

angle (θ) is defined as the angle relative to the proton direction. An alternate form for the polar angle used in the description of energetic hadron collisions is defined as

$$\eta = -\ln(\tan \frac{\theta}{2})$$

As described below, an approximately cylindrically symmetric layout of detector components with roughly uniform segmentation in pseudorapidity (η) and azimuth (ϕ) is chosen.

2.2.1 Tracking Systems

As indicated in the figure 2.3 there are three separate tracking components embedded in a solenoidal magnet which produces a 1.4 *Tesla* field roughly along the incident beam direction. The tracking systems provide information at the level of single charged particle with precise measurement of the track parameters. The trajectories of the particles in the transverse plane, the ($r - \phi$) plane, are determined using the Silicon Vertex Detector (SVX, SVX') [22][23] and the Central Tracking Chamber (CTC) [24]. Between the two components

11
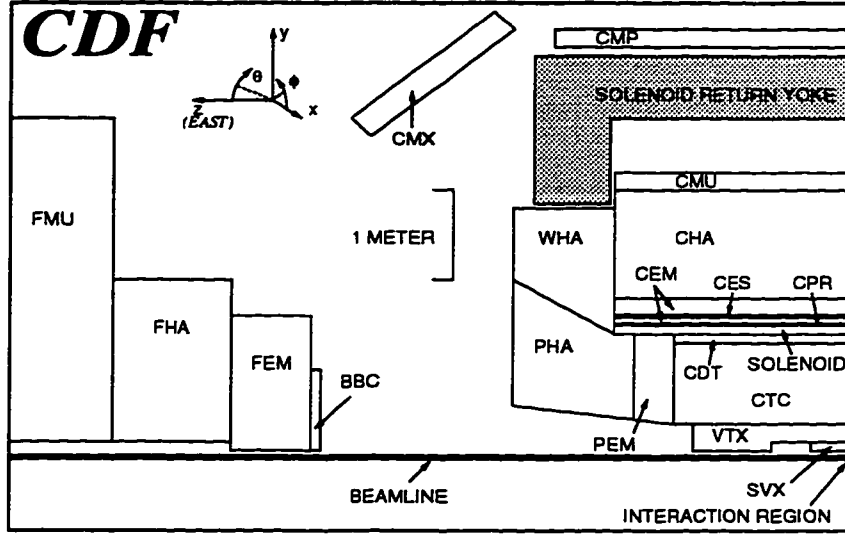
Figure 2.3: A sideview cross section of the CDF detector.

is the CDF Vertex Detector (VTX) [25] which is designed to measure the z-coordinate of the original $p\bar{p}$ collision on an event-by-event basis.

Immediately outside the interaction point the SVX detector and its upgrade, SVX', utilize silicon microstrip technology to measure the asymptotic impact parameters of the tracks in the $(r - \phi)$ plane. With the achievement of higher resolution, on the order of tens of microns, the silicon vertex detectors are able to resolve the event vertices to exploit the potential for interesting physics provided by the observation of sequential decay vertices of short-lived particles such as B hadrons. The algorithm used in this thesis to identify the B hadrons from top quark decay relies heavily on the impact parameter information provided by the SVX. A relatively detailed description of the device is presented in section 2.4.

Further out from the SVX is the Vertex Detector VTX consisting of 24 time-projection chambers. Covering from $+1.5\ m$ to $-1.5\ m$ along the z axis, the VTX is designed to measure the track coordinates in $(r - z)$ plane in order to reconstruct the z

12
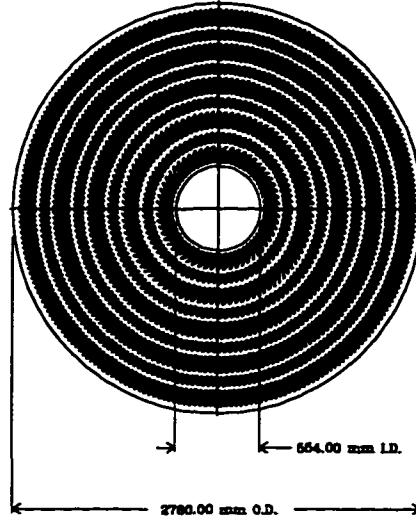
Figure 2.4: End view of the Central Tracking Chamber showing the location of the slots in the aluminum endplates.

position of the primary event vertex. Studies using the VTX information show that a one mm vertex-finding resolution is obtained and the interaction region of the $p\bar{p}$ collisions along the z axis. The distribution of event vertices can be well described by a gaussian of width $\sim$ 30 cm which is also modeled in the Monte Carlo detector simulation program.

The Central Tracking Chamber (CTC) shown in figure 2.4 is a cylindrical drift chamber with a total of 6152 sense wires arranged in 5 axial superlayers and 4 stereo superlayers. The axial superlayers which contain 12 sense wires parallel to the beam line are interleaved with the stereo superlayers each of which contain 6 sense wires tilted $\pm$ 3° with respect to the beam axis. This design provides good reconstruction precision both in the $(r - \phi)$ and $(r - z)$ planes. Pattern recognition is done using only the axial layer data. Each sense wire is also connected to a multiple hit TDC (time digital converter). Using the hit timing information the CTC provides momentum resolution of $\delta P_T/P_T = 0.0011 \cdot P_T$.

13

Both position and momentum of charged tracks can be measured with good resolution in the central region of the detector by CTC.

2.2.2 Solenoid Magnet Coil

The tracking volume of the detector is surrounded by the solenoidal magnet of 4.8 m in length, 3 m in diameter and 0.85 radiation lengths in thickness. A 1.4 *Tesla* magnetic field is produced by 1164 turns of an aluminum-stabilized NbTi/Cu superconductor fabricated using extrusion with the front tension method. The transverse momentum of each charged particle is derived from its curvature as measured by the tracking systems.

2.2.3 Calorimetry

Outside the tracking chambers and the solenoid are the calorimeters. The calorimeters at CDF with total geometric coverage of 2π in azimuth and from -4.2 to 4.2 in pseudorapidity η are separated into three η regions, the central, the end-plug, and the forward. Each region has an electromagnetic calorimeter in front of a corresponding hadron calorimeter. With a projective tower geometry instrumented, a detailed comparison of electromagnetic to hadronic energy on a tower-by-tower basis can be made. A summary of the different components is given in table 2.1.

The central electromagnetic calorimeter (CEM) [26] is divided into ten projective towers, each subtending 0.11 units of η and 15° in ϕ. Energy flow through the CEM is measured using a hybrid design of wavelength shifter and polystyrene scintillator interleaved with lead absorber. Energy resolution is determined to be $\sigma(E)/E = 13.5\%/\sqrt{E \sin \theta}$ using a 50 GeV electron test beam. A proportional strip chamber (CES) is inserted at the depth corresponding to maximum average transverse shower development for the determination of position by measuring of the charge deposition on orthogonal strips and wires. Position resolution of 2 mm at 50 GeV has been achieved.

The central hadronic calorimeter (CHA) [27] and the endwall hadron calorimeter (WHA) cover the polar region between 30° and 150° with cylindrical symmetry. Both CHA

14

Calorimeter Subsystem	Geometric Coverage η Range	Energy Resolution	Absorption Thickness
CEM	$0.0 < |\eta| < 1.1$	$13.7\%/\sqrt{E_T} \oplus 2\%$	$18\ X_0$
PEM	$1.1 < |\eta| < 2.4$	$22\%/\sqrt{E} \oplus 2\%$	$18\text{-}21\ X_0$
FEM	$2.2 < |\eta| < 4.2$	$26\%/\sqrt{E} \oplus 2\%$	$18\ X_0$
CHA	$0.0 < |\eta| < 0.9$	$50\%/\sqrt{E_T} \oplus 3\%$	$4.5\ \lambda_0$
WHA	$0.7 < |\eta| < 1.3$	$75\%/\sqrt{E} \oplus 4\%$	$4.5\ \lambda_0$
PHA	$1.3 < |\eta| < 2.4$	$106\%/\sqrt{E} \oplus 6\%$	$5.7\ \lambda_0$
FHA	$2.4 < |\eta| < 4.2$	$137\%/\sqrt{E} \oplus 3\%$	$7.7\ \lambda_0$

Table 2.1: A summary of the CDF calorimetry components. Thicknesses are given in radiation lengths (X_0) for the electromagnetic calorimeters and in pion interaction lengths (λ_0) for the hadronic calorimeters.

and WHA consist of 48 scintillators sandwiched between iron absorbers with 2.5 cm and 5.0 cm sampling respectively. They are divided into projective towers, each covering approximately 0.1 unit in pseudorapidity and $15°$ in azimuth angle. The transverse segmentation of the hadron calorimeter is chosen to match that of the electromagnetic calorimeter located in front of it. The WHA plugs into cavities in the magnet yoke and also serves as part of the flux return path. Calorimeter response has been studied using muon, pion test beams at 50 GeV and cosmic-ray data.

The plug electromagnetic calorimeter (PEM) [28] is a 2.8 m diameter and 50 cm deep disc-shaped detector with conductive-plastic proportional tube arrays interleaved with lead absorber panels. It covers both ends of the solenoid but leaves a concentric conical hole with an opening angle of $10°$ with respect to the beamline in either direction. An argon-ethane gas mixture is used in the system. Strips of four to five times finer intervals are implemented at the shower maximum. This additional resolution permits the identification of the copious background from $\pi°$'s, low energy electrons or γ's overlapping with high momentum hadrons. The plug hadronic calorimeter (PHA) [29] uses similar conductive-plastic proportional tubes with cathode pad readout. With the same projective geometry and segmentation as the PEM, the PHA provides an additional 5.7 pion absorption lengths of material.

15

Chamber	Geometric Angular Range	Radial Position	Typical Resolution
CMU	$0.03 < |\eta| < 0.63$	$347\ cm < r < 358\ cm$	$250\ \mu m$
CMP	$0.00 < |\eta| < 0.55$	$470\ cm < r < 550\ cm$	$300\ \mu m$
CMX	$0.65 < |\eta| < 1.00$	$440\ cm < r < 520\ cm$	$250\ \mu m$
FMU	$2.40 < |\eta| < 4.20$	$1.0\ m < r < 7.6\ m$	—

Table 2.2: Coverage and resolution of muon chambers.

The forward electromagnetic calorimeters (FEM) [30] are located in the small angle regions in both the proton and antiproton beam directions. They are positioned approximately 6.5 m from the interaction point and enclose the beam pipe at either end of the detector. FEM consists of 30 sampling layers of proportional tube chambers with cathode pad readout similar to the PEM. The tower segmentation is $\Delta\phi \sim 5°$ and $\Delta\eta \sim 0.1$. The position resolution for single electrons ranges from 1 mm to 4 mm depending on location in the calorimeter. The forward hadronic calorimeter (FHA) [31] has the same coverage of 2.2 to 4.2 in pseudorapidity as FEM. The FHA uses steel plates as absorber, with a similar tube chamber and tower geometry design.

2.2.4 Muon Chambers

Beyond the calorimeters are the muon detectors. The chambers used for the muon detection consist of four components, Central Muon chambers (CMU) [32], Central Muon Upgrade (CMP) [33], Central Muon Extension (CMX), and Forward Muon system (FMU). Geometric coverage and position resolution for each component is summarized in table 2.2. Note there are gaps in the η and ϕ coverage in the central region of the CDF detector. Figure 2.5 shows the profile of the central muon chambers in $(\eta - \phi)$ view.

The CMU chambers are separated at $\theta = 90°$ into east and west halves. Each half is divided into 24 wedges each containing 4 layers of muon chambers radially. The small azimuthal staggering of the sense wires within muon chambers permit left-right ambiguity resolution and measures the $(r - \phi)$ position of the track. A muon candidate track is formed

16

CDF η-φ Map for Central Muons

■ - CMX   ▨ - CMP   ⊟⊟ - CMU
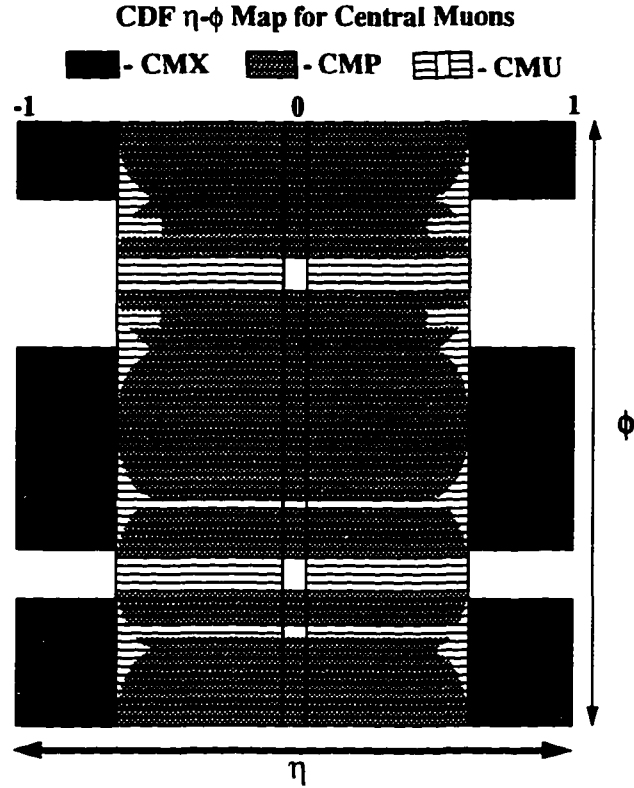
Figure 2.5: η − φ profile of the CDF central muon chambers.

by measuring three or four points along the trajectory matched both in position and angle to the track found in CTC. The CMU chamber wires are read at both ends as a means to determine the z position of the track from charge division. The CMP chambers were installed as an upgrade to the central muon chambers and are of a similar design with the exception that the cells are staggered at 1/2 of their width and the charge deposition on the wires is not instrumented. Therefore no z information is available from the CMP. Coverage of the central muon systems is extended to η = 1.0 using Central Muon Extension (CMX) drift chambers in order to increase the muon acceptance. As shown in figure 2.2, the conical chambers are angled and occupy the surface of a cone in order to point back at the pp̄ interaction point. Like the CMP, the CMX chambers are 1/2 cell staggered.

The CDF forward muon system measures muon position and momentum in the polar region $3° \sim 16°$ and $164° \sim 177°$. With disk-shaped radial symmetry location behind

17

the forward calorimeter, the FMU consists of a pair of magnetized iron toroid, instrumented with three sets of drift chambers and two plans of scintillation trigger counters.

2.2.5 Beam-Beam Counters

Beam-Beam Counters (BBC) are located on the front face of each of the forward and the backward electromagnetic calorimeters, covering the range $3.24 < |\eta| < 5.88$. The BBC consist of two planes of scintillation counters which provide a non-selective interaction trigger (called a "minimum-bias" trigger) and a luminosity monitor for the detector.

2.3 Trigger Systems

The first task to be accomplished for the CDF detector is to decide which of the collisions is worth recording. The physics processes which result from the highly inelastic collisions are selected for recording using a trigger system to determine which events are most interesting. To achieve a reduction of the event rate from the 286 kHz collision rate down to the tape writing speed limit of about 6 Hz, the trigger system is designed as largely dictated by two considerations: (1) the need to extract interesting physics events while minimizing dead time. (2) a desire to be highly flexible and programmable. These are accomplished by using a three-level trigger system [34] in CDF.

2.3.1 Level 1 Trigger

The Level 1 trigger decision is made within the 3.5 μsec interval between crossings. No single Level 1 trigger contributes all the data used in the measurement described in this dissertation but several provide the events for the following Level 2 and Level 3 triggers. Less sophisticated but vital criteria listed below are used to determine whether the event is accepted by the Level 1 trigger.

- Coincidence Hits in the East and West BBCs

18

- Single Hadronic or Electromagnetic Calorimeter Towers Over Transverse Energy Threshold

- Muon Chamber Track Stubs Over Transverse Momentum Threshold

The BBC coincidence requirement, the minimum bias trigger, was required in the lower instantaneous luminosity environment to reduce the rate of false triggers from noises, such as false phototube firings or cosmic rays, which are not usually in coincidence. However, because the spectator quarks from the inelastic collisions can cause the minimum bias trigger to fire, the BBC trigger was nearing saturation as the instantaneous luminosity increased. The requirement was dropped later in the run.

The calorimeter trigger is determined using the information from projective towers segmented in $(\eta - \phi)$ plane by $\Delta\phi = 15°$ and $\Delta\eta = 0.2$. After calibration for pedestal offsets and gain variations, signals from the 2048 electromagnetic and hadronic trigger towers are processed into fast analog sums for groups of 4 towers. Transverse energy in the tower is calculated as $E_T = E \sin\theta$ where θ is measured assuming collisions occurred at $z = 0$. Various energies are compared to thresholds for different systems to determine if the event is to be selected.

The muon trigger [35] makes a fast determination if the transverse momentum of CMU muons exceed the threshold. A simple CMP hit coincidence can also fire the trigger. The combined Level 1 CMU and CMP inclusive muon trigger rate is around 300 to 500 Hz.

2.3.2 Level 2 Trigger

All detector data are held after the event passes the Level 1 trigger. The Level 2 decision is determined in about ~ 20 μsec [36] by more sophisticated trigger operation list below.

- Fast CTC Track Pattern Recognition (CFT)

- Hadronic and Electromagnetic Calorimeter Clustering

19

- Matching CFT Tracks to Muon Hits

- Matching CFT Tracks to Calorimeter Clusters

- Global Energy Sums

The timing and ϕ position of all hits on the five axial superlayers of the CTC are used in the Central Fast Tracker (CFT) [37] to identify tracks curving in the solenoidal field. Through a pattern recognition look-up table, the CFT measures the transverse momentum of found tracks with a resolution of $\delta P_T/P_T \sim 0.035 P_T$. The P_T of the tracks is then quantized into eight bins with central values from 3.3 to 30.0 GeV/c. P_T and ϕ information of the found tracks is also used in association with the Level 1 Muon trigger hits to reduce the muon trigger rate. The match is done using the P_T and ϕ values of the CFT track to project to the muon chambers followed by the requirement that muon stub be found within a certain $\Delta\phi$ window.

The Level 2 trigger system has the ability to perform calorimeter clustering. The signals from segmented electromagnetic and hadronic calorimeters are used to locate clusters which can also be matched to the CFT track list. Both jet clustering (hadronic and electromagnetic combined) and electron/photon clustering (electromagnetic only) information are available at Level 2 trigger. Several global energy sums can be obtained at Level 2. The total transverse energy, the total missing transverse energy and the total clustered energy information are either used alone or in conjunction with other Level 2 data to make the trigger decision.

2.3.3 Level 3 Trigger

After the receipt of a Level 2 trigger, all channels in the detector are digitized and read within 2 - 3 ms. The Level 1 and Level 2 triggers are then reset and enabled for subsequent beam crossings while the Level 3 trigger system [38] processes the event. Global event reconstruction is undertaken with tests applied to events by Level 3 code which takes place in a cluster of 48 Silicon Graphics computers. Most of the event analysis is done by

20

programs written in the Fortran language which permits potentially elaborate identification. The Level 3 system is capable of filtering on objects such as electrons, muons, taus, dimuons, multi-jets, etc., and can process data into several trigger output streams. With the trigger rate reduced to 6 - 8 Hz the raw data can be recorded on disk drives and/or written to 8 mm tape drives.

2.4 The Silicon Vertex Detector

A silicon microstrip vertex detector designed for the CDF was commissioned during the Tevatron run and achieved excellent tracking and secondary vertex identification with high precision. The detector (SVX) was installed and began to collect data in 1992. The first version was replaced by an upgrade, referred as SVX', as a result of radiation damage encountered by its first unit. The remainder of data-taking between 1993-1995 was done with the SVX'. The detector hardware and the tracking performance for both devices are described below.

2.4.1 Geometry

SVX and SVX' have the same overall geometric design. Both consist of two 12-sided electrically independent barrels of equal length as shown in figure 2.6. The barrels are aligned coaxially with the beamline and symmetrically about the interaction point with a 2.15 cm gap centered at $z = 0$. The active length of both devices is 51 cm which results in an acceptance of $\sim$ 60% of the $p\bar{p}$ collisions.

Each barrel is made of four concentric layers, numbered from 0 to 3 in increasing radius. The basic building block of the layers is a ladder, shown in figure 2.7, composed of three 8.5 cm DC-coupled (for SVX) or AC-coupled (for SVX') singled-sided silicon microstrip sensors. The sensors are wired-bounded end to end to form the primary mechanical and electrical units. Each ladder is rotated 3° about its longitudinal axis in order to provide overlap between adjacent ladders. Their strip pitches are 60 μm for the inner three layers

21
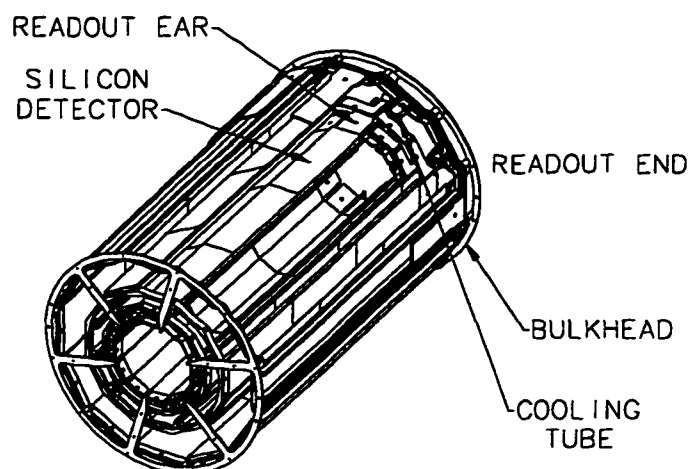
Figure 2.6: A cutaway view of half of the Silicon Vertex Detector.

and 55 μm for the outermost layer. The readout end of the ladder is microbounded to an off-board custom thick-film hybrid referred as an "ear". The ear carries 2, 3, 4, or 6 SVXD (for SVX) or SVXH3 chips (for SVX') for layer 0 to 3 respectively. The SVXH3 chip has 20% less noise and 30% more gain compared to the SVXD. A copper-Kapton cable known as a "pigtail" connects the ear to the data acquisition system. Two reference holes are located at the opposite end of the ladder for alignment.

Corresponding layers in SVX and SVX' have the same radius except layer 0. The radii of the layer 0 is 3.005 cm for SVX or 2.861 cm for SVX'. Radii of layer 1 to 3 are 4.256, 5.687 and 7.866 cm respectively. Layer 0 is positioned as close as possible to the beampipe for the best possible measurement of the impact parameter of tracks. The design modification of a smaller radius and an additional 1° rotation between the adjacent ladders at layer 0 in the SVX' improves the ϕ coverage by eliminating a 1.26° gap present in the SVX. The middle two layers, layer 1 and layer 2, provide redundancy near the beamline in the high track density and high radiation environment. The outmost layer, layer 3, provides good matching between the vertex detector and the outer tracking system.

22
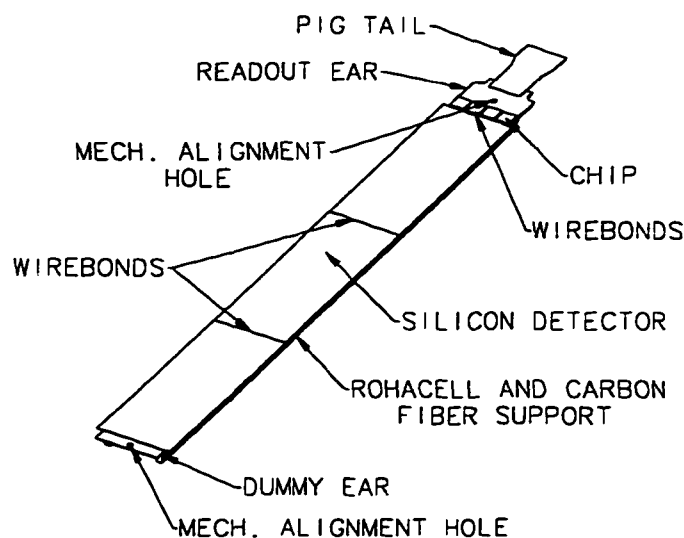
Figure 2.7: An SVX ladder.

2.4.2 Front End Electronics

Each SVX or SVX' barrel is divided into 12 wedges of 30° in ϕ and the wedges are individually readout. A total of 46,480 channels are operated in a spare scan mode so that only channels whose integrated charge is above a threshold are digitized. Two sparsification thresholds can be set per wedge. The DC-coupled SVX necessitates that the device be operated in a quadruple sample and hold mode. The leakage current per channel is typically less than 2 nA but varies strip to strip. Sensitivity to these variations can be minimized by processing a signal that results from the difference between two charge integrations at "on beam" and "off beam" times. The SVX' design reduces the noise level by $1/\sqrt{2}$ compared to that of SVX by using AC-coupling with only one integration being done at "on beam" time since the leakage current does not appear at the preamplifier input. The signal to noise ratio (S/N) was 9.5 for SVX and 16.0 for SVX' at the time of installation. The characteristics of each channel was monitored by taking calibration runs between the Tevatron stores when there was no beam activity. Pedestal, gain and the threshold of each channel were examined.

The sequence of read-out operations is governed by clock-signals synchronized with

23

the Tevatron. It begins with the integration of the signal from the hit channels. The multi-level CDF trigger system described in Section 2.3 determines whether a given event is to be passed to the data acquisition system (DAQ). For the SVX operation, after a Level 1 trigger is received, a second, "off beam", integration is then performed, followed by a latch being set if the latter integration produces a value over the threshold. The process is simplified in the operation of SVX' which requires only one integration, a benefit of the AC-coupled design. The mixed analog and digital signal processing circuits, SVXD or SVXH3 chips, read out the analog pulse height and digital address of the latched channels.

The four ears in each wedge, which consists of 4 ladders from each of the layers, are daisychained to an interface card called "port card". The port card connects serially to a digitizer where analog data generated by the chips is converted to differential voltages before transmission to the external DAQ system. A group of six digitizers from half of a barrel are connected to a sequencer, a FASTBUS unit [39]. A total of four programmable sequencers provide the clocking signals necessary to operate the SVXD or SVXH3 chips. These units provide synchronization to the 53 MHz CDF Master clock which drives the DAQ system and contains storage for one event as it is pipelined to a set of SLAC Scanner Processor (SSP). The processors store and reformate the data according to CDF protocols.

2.4.3   Offline Performance

Data collected using SVX or SVX' is processed in a two-step offline analysis. Reconstruction of the tracks begins with the raw charge levels on individual strips and ends with segments associated with external tracking chambers that together form the final tracks.

The conversion from charge levels on individual strips to clusters is performed with an offline pedestal subtraction on a strip-by-strip basis with the full 46080 channel pedestals available. After the pedestal subtraction the strips are clustered using an algorithm that requires data from contiguous strips of a group, called a cluster. The threshold for a cluster is based on the measured strip noise and the number of non-dead strips in the group. Table 2.3 shows the multiplicative factors of SVX and SVX' signal-to-noise thresholds which are

24

Number of Strips	Multiplicative Factor	
	SVX	SVX'
1	4.0	4.0
2	2.5	2.5
3 - 8	2.0	2.0
≥ 9	1.5	2.0

Table 2.3: The multiplicative factor for SVX and SVX' hit clustering, by number of strips in the cluster candidate.

Number of Strips	Computed Resolution	
	SVX	SVX'
1	15 μm	13 μm
2	13 μm	11 μm
3	25 μm	19 μm

Table 2.4: Assigned cluster errors derived for SVX and SVX' cluster with fewer than four associated strips.

applied on each strip in the cluster candidates for various cluster widths. The factors were optimized for "good" hit efficiency and noise rejection in cosmic rays and collision data where "good" hits refers to clusters containing 4 or less strips without any dead strips. The grouping is broken into two or more cluster candidates if any strip fails the threshold requirement, followed by the clustering process being performed again.

The cluster position is calculated as a charge weighted centroid using individual strip charges and strip center positions. The spatial resolution of the cluster is also assigned based on the total charge and the number of strips. For clusters with charge ≥ 11.7 fc, or those with more than 3 strips, the position error is computed using (strip pitch $\times$ number of strips)/$\sqrt{12}$. For clusters with 3 or fewer strips, the resolution, shown in table 2.4, is obtained from a study of the residual distributions from the final track fits in the data.

The cluster-finding efficiency along the paths of particles can thus be studied by counting tracks, found by the external tracking chambers, which extrapolate into the SVX

25

Layer	Hit efficiency	
	SVX	SVX'
0	93%	95%
1	93%	96%
2	93%	96%
3	93%	95%

Table 2.5: Cluster-finding efficiency for SVX and SVX' ladders.

or SVX' tracking volume and have missing hits on some of the layers. The efficiency can be affected by signal to noise ratio, sparse readout, pedestals, clustering, pattern recognition, bad regions and geometrical acceptance. Table 2.5 shows the efficiencies for SVX and SVX'.

Despite the accurate measurement of the $(r - \phi)$ position of charged tracks as they pass through the silicon vertex detector, the optimal track reconstruction is done using information from all the tracking detectors at CDF. Starting with a 2-dimensional fit in the transverse plane using hits from the CTC axial superlayers, a five-parameter 3-dimensional track fit was performed with additional information from the VTX detector and the CTC stereo superlayers. The five track parameters chosen by CDF for all analysis are:

- c : the 2-dimensional curvature which is inversely proportional to the transverse momentum of the track

- $\cot \theta$: the cotangent of the polar angle θ

- d_0 : the distance of closest approach of the track to the primary vertex in the transverse plane

- z_0 : the z coordinate of the distance of closest approach as defined for impact parameter

- ϕ_0 : the ϕ direction of the track at the distance of closest approach as defined for impact parameter

26

Clusters	Fraction	
	SVX	SVX'
4	70.5%	81.3%
3	23.0%	15.3%
2	4.5%	2.1%
total	98.0%	98.7%

Table 2.6: Fraction of tracks associated with 2, 3, and 4 SVX or SVX' clusters found in the track-finding studies.

Extrapolation of the CTC tracks into the SVX fiducial volume is then performed. A road, the search region for associated SVX clusters, is defined based on the track parameters and their uncertainties. The track parameters and the error matrix as well as the road are recalculated once a cluster is found. Multiple scattering and ionization energy loss in the material are taken into account during the extrapolation. The cluster assignment to a track candidate is determined according to the goodness-of-fit, χ^2, from the track fit and number of associated clusters used. The χ^2 of the track fit is updated at each step and used as a cut to retain possible candidates. The procedure is iterated for each layer inward toward the beamline until all four layers are examined. The one with the lowest total χ^2 is chosen among the possible track candidates associated with an external track. The tracking algorithm also prefers tracks with more clusters. If there is no track can be reconstructed using clusters from each of the four layers, the extrapolation seeks tracks associated with three clusters. The fit χ^2 is still used to pick the best candidate. The search continues for two-hit tracks if needed. Reconstructing one-hit tracks is not permitted. The tracking finding efficiency can be calculated using well reconstructed CTC tracks which extrapolate within the SVX fiducial volume. Studies show efficiencies of 98.0% [22] in SVX and 98.7% [40] in SVX' were reached. The fraction of tracks with 2, 3, and 4 clusters is shown in table 2.6.

During 1992-96 Tevatron data-taking, SVX and SVX' recorded about 110 pb^{-1} of data and were functioning within their specifications. The $p\bar{p}$ interaction point and displaced

27

tracks from the b-hadron decay were both identified with the information provided. These are used as input to the tagging algorithm which identifies b quark from $t\bar{t}$ decay described in the following chapters.

28

Chapter 3

Event Selection

The experimental signature of the "lepton plus jets" final state from $t\bar{t}$ decay is a subset of events containing W bosons in association with jets. In this chapter, all cuts made for the W + jets event selection are described. These include lepton identification, missing transverse energy ($\not{E}_T$) measurement and modeling of the jets as well as associated energy corrections. Selection criteria used to remove events containing Z bosons from the sample are also listed. Thresholds of the cuts applied on the data taken during 1992-93 (run 1A) may be different from those applied on the data taken during 1994-96 (run 1B) due to upgrade of the detector components or higher instantaneous luminosity environment.

A search for the $t\bar{t}$ candidates begins with the selection of the inclusive W + jets events. A high transverse-momentum electron or muon from the W leptonic decay involves an emission of a neutrino, which must be inferred from the imbalance in the observed calorimeter energy. The presence of the W signals can be further indicated by a mass peak around W mass value. However, the ability to reconstruct the dilepton invariant mass of the $e\nu$ or $\mu\nu$ system is limited by the unknown component of the neutrino momentum in z direction. Instead a two dimensional analog of the dilepton invariance mass, transverse mass (M_T), is used.

Calorimeter responses as totaled within a cone of fixed radius in ($\eta - \phi$) plane are designated as hadronic jets. Since $t\bar{t}$ decays are expected to contain large numbers of hadronic jets relative to events from single W production, the number of jets will be used

29

to enhance the $t\bar{t}$ signal. The $t\bar{t}$ candidates are then observable only at the high end of the leptonic W decay candidates when plotted as a function of the number of jets observed in the event. In the next chapter, the presence of a b-flavored hadron among the jets is required to further isolate the $t\bar{t}$ candidates.

3.1 Electron Identification

Electrons passing through the central rapidity ($|\eta| \leq 1.0$) region of the detector are used in the analysis. The well-instrumented tracking and calorimeter components in the region provide the trigger decision and offline selection to reconstruct electron candidates.

3.1.1 Triggers

The Level 1 electron trigger required at least one CEM or CHA trigger tower with E_T ($= E * \sin\theta$) greater than certain thresholds. The CEM and CHA thresholds were set to be 6 and 8 GeV respectively during run 1A, and were raised to 8 and 12 GeV for run 1B data-taking. The change in thresholds reduced the corresponding growth in trigger rate due to the increase of instantaneous luminosity of the $p\bar{p}$ collisions.

The central electron trigger at Level 2 made use of more sophisticated calorimeter clustering and CFT tracking information. Calorimeter clusters were constructed as sets of contiguous CEM trigger towers. The inclusive electron trigger required an energy cluster with $E_T > 9\ GeV$ to be associated with a CFT track with $P_T > 9.2\ GeV/c$ during run 1A or a cluster with $E_T > 8\ GeV$ associated with a CFT track with $P_T > 7.5\ GeV/c$ during run 1B. The upgrade [41] of electron trigger hardware used during run 1B allowed information about the position and size of electromagnetic showers to be used in the trigger decision. Thresholds were thus lowered to collect more data.

The level 3 trigger made more cuts on the electron selection using programmable software to perform a 3-dimensional CTC track reconstruction. The central electron trigger

30

at Level 3 required a track with $P_T > 13$ (10) GeV/c pointing to a electromagnetic cluster with $E_T > 20$ (18) GeV during run 1A (1B).

3.1.2 Offline Selection

The offline selection of events is applied to events that have passed the triggers. The raw data is passed through the CDF offline "Production" program to perform event reconstruction. The CEM clustering algorithm starts with a seed tower with $E_T > 3$ GeV and two neighboring towers with $E_T > 1$ GeV in pseudorapidity. The size of the cluster is 3 towers in pseudorapidity ($\Delta\eta = 0.3$) by 1 tower in azimuth ($\Delta\phi = 15°$). Towers adjacent in ϕ are not considered because electromagnetic showers do not extend over the ϕ boundary of the wedges by construction. The central electron is defined as a CTC track extrapolating to a CEM cluster.

The signature can also occur when an event has multiple photons with charged particles nearby. The electromagnetic energy deposit would be created by the photons and the charged particles leave signals in the tracking chamber. Overlaps of photons and charged particles occur frequently in the $p\bar{p}$ collisions since jets produce mainly charged and neutral pions. In order to suppress these overlaps, signal patterns in the calorimeters and tracking chambers are compared to those expected for a single electron. The patterns to be examined are:

1. Longitudinal shower shape

    - HAD/EM, a ratio of hadronic energy to electromagnetic energy of the cluster: Cluster in the central pseudorapidity region are accepted as "electromagnetic" when the ratio is below 0.05.

2. Lateral shower shape

    - L_{shr}, a comparison of the lateral shower profile in the calorimeter cluster with that of test beam electrons: L_{shr} is zero when an observed shape matches the

31

expectation for a single electron. For hadronic showers extending over towers, extra energy is shown in the adjacent towers and the L_{shr} value becomes larger. An appropriate cut of 0.2 is used.

- χ^2_{strip}, a χ^2 comparison of the CES shower profiles with those of test beam electrons: A single shower hypothesis is applied to compare with the measured shower shape. Showers from π^o's or QCD jets show larger χ^2 value. An appropriate cut of 10 is used.

3. Geometrical matching of the calorimeter shower and the track positions

- $|\Delta x|$ and $|\Delta z|$, the distance between the position of the extrapolated CTC track and the CES shower position measured in $(r - \phi)$ and z view: An electron candidate with most of the energy coming from photons matched to a charged hadron track results in a mismatch of the energy deposition and track positions. Requiring a geometrical matching with $|\Delta x| < 1.5$ cm and $|\Delta z| < 3.0$ cm rejects such events.

4. Energy and momentum comparison

- E/P, the ratio of cluster energy to track momentum: With an electron shower isolated in three CEM towers, the E/P distribution is peaked around unity. A 1.5 cut is applied on the data taken during run 1A. The cut was relaxed to 1.8 for run 1B data in order to be consistent with the one used in top dilepton analysis.

Photon conversion in the material preceeding the CTC can produce an electron-positron pair that must be removed on an event-by-event basis. Tracks from conversions can be rejected if few associated hits can be found in the VTX or if they pair with tracks of opposite sign to form a small invariant mass that originates inside the CTC. An track will be consider a conversion if

- VTX occupancy < 0.2

32

Variable	Cut
HAD/EM	< 0.05
L_{shr}	< 0.2
χ^2_{strip}	< 10
Δx	$< 1.5\ cm$
Δz	$< 3.0\ cm$
E/P	1A: < 1.5, 1B: < 1.8
conversion removal	-
z-vertex match	$< 5.0\ cm$
isolation	$I_{cal} < 0.1$

Table 3.1: Central electron offline selection requirements.

- $|\Delta R| < 0.3$: ΔR is the separation of two tracks in $(r - \phi)$ plane at the point where they are tangent (the conversion point).

- $|\Delta \cot \theta| < 0.06$: At the conversion point where $\Delta \phi_{ij} = 0$, the invariant mass formed by the track pair is $M_{min} \simeq \sqrt{P_i P_j} * |\Delta \cot \theta|$. The requirement on $|\Delta \cot \theta|$ implies the same cut on the invariant mass and excludes the uncertainties from the momentum measurement.

- $-20\ cm < R_c < 50\ cm$: R_c is defined as the distance from center of the detector to the conversion point. Some of the conversion points can be observed at the opposite hemisphere to the tracks.

In addition, two more variables are used to select electrons coming from W decay. Electron candidates are required to be located within 5 cm in z direction of the $p\bar{p}$ interaction point to ensure that the track originated at the primary vertex. An isolation requirement is also applied to distinguish W decay electrons from those resulting from heavy flavor decays. A calorimeter isolation, I_{cal}, defined as the ratio of transverse energy in the towers within a cone of radius $R = \sqrt{(\Delta\phi)^2 + (\Delta\eta)^2} = 0.4$ centered on the electron but excluding the electron E_T to the electron E_T, is required to be less than 0.1. Table 3.1 summaries the selection requirements for the central electrons.

33

3.2 Muon Identification

The "μ + jets" events use muons in the central rapidity ($|\eta| \leq 1.0$) of the detector. CTC and muon chambers (CMU, CMP, and CMX) provide the trigger decision and offline reconstruction to select muon candidates. The central muon identification also makes use of the energy deposition in the different calorimeter components.

3.2.1 Triggers

The Level 1 central muon trigger relies on a fast analog estimation for the arrival times of the drift electrons at the sense wires of different layers in the muon chambers. The difference in times results from the deflection of the muon under the magnetic field relative to the alignment of the projective wires. The trigger cuts on certain maximum difference in times, which corresponds to a minimum cut on $P_T > 6$ GeV/c for CMU/CMP and $P_T > 10$ GeV/c for CMX. A CMU trigger also requires CMP trigger confirmation in those CMU towers covered by CMP chambers.

The Level 2 muon trigger requires a match between a CFT track in ($r - \phi$) plane with $P_T > 9.2$ GeV/c during run 1A or $P_T > 12$ GeV/c during run 1B, and a Level 1 muon trigger segment. The match was declared if projection of the CFT track was within a certain $\Delta\phi$ window of the muon chamber segment. More precise match is required by the Level 3 trigger that cuts at 10 cm in Δx ($= r * \Delta\phi$) between a reconstructed track with P_T greater than 18 GeV/c and the muon segment. Energy deposition in the associated CHA tower was also used in the Level 3. It was required to be less than 6 GeV.

3.2.2 Offline Selection

The offline "Production" process makes loose identification of muon candidates. The process performs several basic functions:

1. CTC tracking pattern recognition

2. Muon chamber track stub reconstruction

34

3. Calorimeter clustering

The lists of CTC tracks and CMU/CMP stubs are matched to yield possible muon candidates, with a number of Δx quantities describing the geometrical matching distance. From the matching to the calorimeter towers, the minimum ionizing energy deposition is available in order to reduce backgrounds. The following variables are used to separate muons from hadrons or cosmic rays that interact in the calorimeters.

- EM energy: An energy deposition in the electromagnetic calorimeters should be less than 2 *GeV*.

- HAD energy: An energy deposition in the hadronic calorimeters should be less than 6 *GeV*. The cut is looser than that for EM energy because of the extra absorption lengths in the hadronic compartment.

- Δx: The distance between the extrapolated position of the CTC track and the actual position of the muon chamber stub is required to be less than 2 *cm* for CMU, 5 *cm* for CMP and CMX.

- Impact parameter: The closest approach of the reconstructed track to the beam line is required to be less than 3 *mm* in order to reject cosmic rays.

As used in identifying electrons, the same two additional cuts are used in the muon selection to enhance muons coming from W decay. Muon tracks are required to be located within 5 cm in z direction of the interaction vertex. An isolation requirement is also applied on the muon candidates in order to distinguish W decays from those from heavy flavor decays. The calorimeter isolation, I_{cal} is required to be less than 0.1. Table 3.2 lists the selection requirements for the central muons.

35

Variable	Cut
EM energy	$< 2\ GeV$
HAD energy	$< 6\ GeV$
Δx	CMU: $< 2.0\ cm$, CMP and CMX: $< 5.0\ cm$
impact parameter	$< 3\ mm$
z-vertex match	$< 5.0\ cm$
isolation	$I_{cal} < 0.1$

Table 3.2: Central muon offline selection requirements.

3.3 Missing Transverse Energy Measurement

The missing transverse energy ($\not{E}_T$) is defined to be the negative of the vector sum of all energy projected in the transverse plane of the entire detector with $|\eta| < 3.6$:

$$\not{E}_T = -\sum_i E_{Ti}\,\hat{n}_i$$

where the sum is over calorimeter towers, E_{Ti} is the transverse energy on tower cell i, and $\hat{n}_i$ is a unit vector in transverse plane pointing to the cell i.

A correction is needed if there exist muons or minimum ionizing particles in the event. $\not{E}_T$ is corrected for the P_T of muons (P^μ) and minimum ionizing energy $(E^{min.ion.})$:

$$\not{E}_{Tx} = -(E_x^{calorimeter} + P_x^\mu - E_x^{min.ion.})$$

$$\not{E}_{Ty} = -(E_y^{calorimeter} + P_y^\mu - E_y^{min.ion.})$$

$$\not{E}_T = \sqrt{\not{E}_{Tx}^2 + \not{E}_{Ty}^2}$$

Detector effects may introduce a finite and relatively poor resolution in the measurement of the missing transverse energy. The resolution is determined by the calorimeter resolutions, nonlinear responses of the calorimeter to hadrons, and inactive regions of the detector. The $\not{E}_T$ resolution is given approximately by $0.7\sqrt{\sum E_T}$, where $\sqrt{\sum E_T}$ is the scalar sum of the transverse energy measured in units of GeV.

36

3.4 Jet Identification and Energy Corrections

The CDF jet clustering algorithm uses a cone of a fixed radius in order to produce cleanly separated jets. It begins by creating a list of towers above an E_T threshold 1.0 GeV which are used as seeds. Preclusters are formed from an unbroken chain of contiguous seed towers and are used as the starting point for the jet finding algorithm. A cone in $(\eta - \phi)$ plane of radius R is formed around the E_T weighed centroid of the precluster. A choice of radius $R = 0.4$ is used from the Monte Carlo studies. All towers with $E_T > 0.1$ GeV are incorporated into the cluster if their centroids are inside the cone. The cluster center is re-calculated using all included towers and a new cone is drawn to iterate the process for finding new or deleting old towers until the tower list remains unchanged.

The associated quantities with the cluster can be computed. The direction of the cluster is defined by a unit vector pointing from the event origin to the center of the face of the calorimeter towers. Once the primary vertex is found, a correction is made to apply on the pseudorapidity of all clusters from detector pseudorapidity ($\eta_{detector}$) to event pseudorapidity (η_{event}) due to the Gaussian distribution of the primary vertex spreading out along the beamline. The cluster energy is calculated as the scalar sum of the tower energies. This uncorrected energy may differ from the true partonic values. The difference results from either the fundamental elements of the physics process or limitations of the detector performance. These include effects due to:

- Energy not associated with the hard scattering process, i.e. contribution from the underlying event collected within the clustering cone

- Out-of-cone energy loses resulting from the transverse spreading of the jet fragmentation

- Undetected energy carried by muons or neutrinos

- Non-linearity of the calorimeter response to low energy particles with $P_T < 10$ GeV/c

37

- Energy loses due to low P_T charged particles which either do not reach the calorimeter or are bent outside the clustering cone in the magnetic field

- Reduced calorimeter response at the boundaries between detector components and calorimeter subsystems

A correction which depends on the jet E_T and detector pseudorapidity ($\eta_{detector}$) is generated and applied to the data sample in order to reproduce the average jet E_T correctly. Uncertainties on the energy scale of jets result from a theoretical uncertainty in the jet fragmentation, detector responses to the low energy pions, modeling ability for the variation of the single pion response in the detector simulation, and energy scale calibration.

3.5 Z Identification

Z leptonic decays can produce two opposite charged electrons or muons. A set of cuts is applied on the sample to exclude events containing Z bosons. The removal is to reduce backgrounds from misidentified Z bosons that mimic W decays where one leg of a Z decay is identified as the primary lepton which is reconstructed and selected by the cuts listed in previous sections. For the purpose of Z rejection, the second candidate lepton is identified with rather loose cuts described below.

- The second candidate leg of a $Z \rightarrow ee$ event can be in the central, plug, or forward calorimeters. The electron should satisfy:

  - $E_T > 10 \ GeV$

  - $E/P < 2.0$ for a central electron

  - Had/EM < 0.12

  - Calorimeter isolation $(I_{cal}) < 0.2$

- The second leg of a $Z \rightarrow \mu\mu$ event can be in the CMU, CMU/CMP, CMP, or CMX. Muons in regions of the detector not covered by muon chambers, but the energy in

38

the calorimeter tower in the path of the extrapolated track which is consistent with that for a minimum ionizing particle (CMIO muons) are also included. The muon should satisfy:

- $P_T > 10 \ GeV/c$

- HAD energy $< 10 \ GeV$ for CMU, CMU/CMP, CMP and CMX muon; HAD energy $< 6 \ GeV$ for CMIO muon

- EM energy $< 5 \ GeV$ for CMU, CMU/CMP, CMP and CMX muon; EM energy $< 2 \ GeV$ for CMIO muon

- Calorimeter isolation $(I_{cal}) < 0.2$

- Track stub matching: $\Delta x < 5 \ cm$ for CMU, CMU/CMP, CMP and CMX muon

- $|\eta| < 1.2$ for CMIO muon

The event is flagged as a Z event if the transverse mass of the lepton pair is between 75 GeV/c^2 and 105 GeV/c^2.

3.6   Inclusive W + Jets Selection

The W + jets event selection begins with data taken in those runs when the detector was fully functioning. A "fiducial run" requirement removes events affected by detector high voltage malfunctions, data acquisition errors or trigger problems. Events with z-coordinate of the $p\bar{p}$ collision outside 60 cm of the center of the CDF detector are also rejected because of possibly incomplete collection of the decay fragments. Events containing Z bosons are removed from the sample.

Selection of $W \rightarrow e\nu$ or $W \rightarrow \mu\nu$ candidate requires an electron with $E_T \geq 20$ GeV or muon with $P_T \geq 20 \ GeV/c$ and pass the trigger and offline identification outlined in previous sections. The neutrino identification is made with $\not{E}_T \geq 20 \ GeV$. Figure 3.1 shows the electron E_T and muon P_T distribution before and after the $\not{E}_T$ cut. The $\not{E}_T$ requirement

39

Jet Multiplicity	Electron Events	Muon Events	Total Events
0 Jet	62267	40072	102339
1 Jet	6233	4483	10716
2 Jet	938	725	1663
3 Jet	144	110	254
$\geq$ 4 Jet	31	39	70

Table 3.3: Summary of W candidate event yields as a function of jet multiplicity.

reduces backgrounds from misidentified leptons in QCD-jet events or semileptonic decays in $b\bar{b}$ events. The transverse mass thus can be calculated using

$$M_T{}^2 = (E_T{}^{e,\mu} + E_T{}^\nu)^2 - (\vec{E}_T{}^{e,\mu} + \vec{E}_T{}^\nu)^2$$

The spectra of the transverse mass in the $e\nu$ and $\mu\nu$ systems are shown in figure 3.2. The M_T spectrum peaks below the W mass value is due to the unknown neutrino momentum in z-coordinate and a high mass tail is representative of the experimental uncertainty in the missing transverse energy. To study the number of jets associated with W production, clusters with $E_T \geq 15\ GeV$ and $|\eta| \leq 2.0$ are counted as jets. Number of events in the W sample classified according to the jet multiplicity, N_{jet}, are shown in table 3.3.

$t\bar{t}$ events in the inclusive W sample are rather distinctive in their global event topology. Decay of $t\bar{t}$ into the "lepton plus jets" channel involve significant jet activity. In principle one might expect to observe a four-jet final state along with $W \rightarrow e\nu$ or $\mu\nu$. However in practice jets might coalesce, be lost down to the beamline, or fail the jet selection criteria. Figure 3.3 shows the expected jet multiplicity distribution for Monte Carlo $t\bar{t}$ events passing the detector simulations with top masses of 165, 175 and 185 GeV/c^2. It is found that $\sim$ 75% of the $t\bar{t}$ events have at least 3 jets with little dependence on the top mass while less than 0.4% of all W events in the data sample pass the same requirement. Therefore, the $t\bar{t}$ search sample requires $N_{jet} \geq 3$ to improve the signal-to-background ratio. Table 3.4 summaries the $t\bar{t}$ signal sample selection requirements.

In order to further differentiate $t\bar{t}$ events from QCD W + multijet events, the pres-

40

ence of a b-flavored hadron among the jets is required. In the next chapter, a tagging algorithm is introduced to exploit displaced vertex from b decay and applied on the inclusive W + jets sample to isolate possible $t\bar{t}$ signals.

Selection Criteria	Cut
Good Quality Run	
Trigger Requirement	
Good Lepton	Electron $E_T \geq 20$ Gev or
	Muon $P_T \geq 20$ GeV/c
Lepton Isolation	$I_{cal} < 0.1$
Z Removal	
Missing Transverse Energy	$\not{E}_T > 20$ GeV
Jet Multiplicity	$N_{jet} \geq 3$

Table 3.4: Summary of the $t\bar{t}$ signal sample selection requirement.
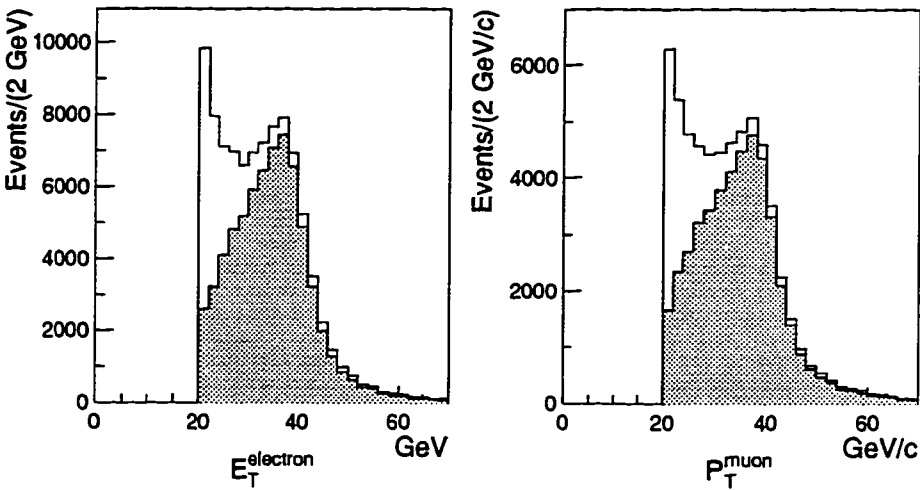
Figure 3.1: The electron E_T and muon P_T spectra before (histogram) and after (hatched) missing transverse energy requirement.

41
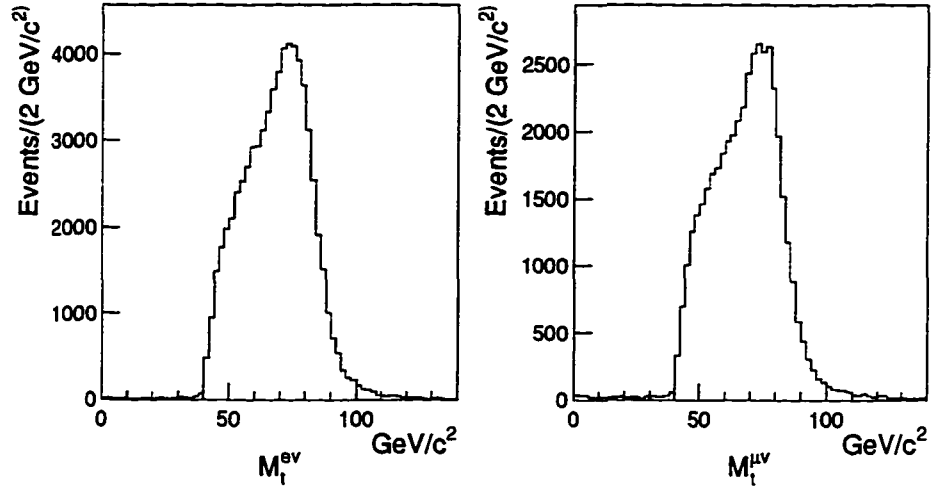
Figure 3.2: The transverse mass distributions for the $W \to e\nu$ and $W \to \mu\nu$ samples.
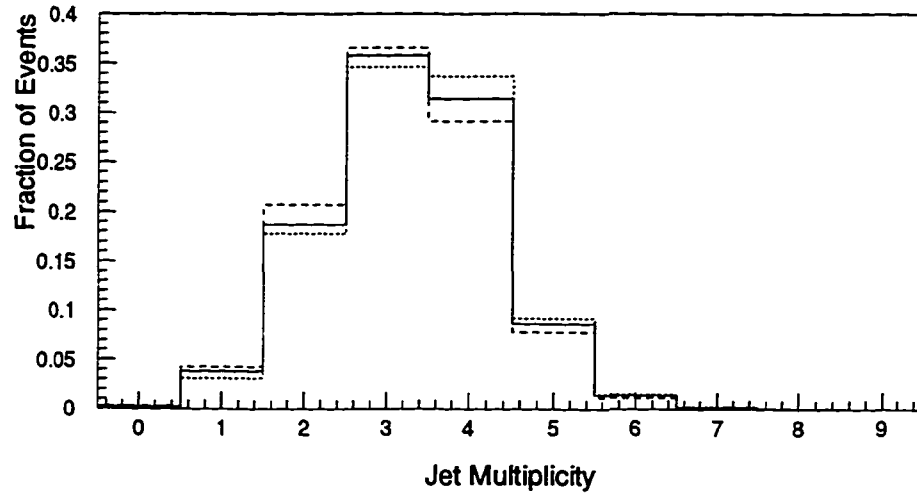
Figure 3.3: The expected jet multiplicity distribution for events passing the W selection criteria in $t\bar{t}$ events with top mass set to be 165 (dot), 175 (solid), and 185 GeV/c^2 (dash).

42

Chapter 4

The Tagging Algorithm

The presence of jets originating from b quarks is one of the distinctive features of the $t\bar{t}$ signals. The number of b jets expected in each of the jet multiplicity bins for events passing the W selection criteria in $t\bar{t}$ Monte Carlo samples is shown in figure 4.1. Further suppression of the W + multijet background can be achieved if at least one b or $\bar{b}$ quark can be identified. Described in this chapter is the task accomplished using a tagging algorithm. The procedure exploits the ability of the SVX detector for precisely measuring the impact parameters of the decay products in order to reconstruct the displaced vertices of b hadrons.

Section 4.1 describes the determination of the primary vertex position on an event-by-event basis. The concept of the impact parameter and its relation to both the primary and displaced vertices is also discussed. Section 4.2 briefly shows the kinematics of the b quarks, especially those occurring in the $t\bar{t}$ events. The tagging algorithm is described in section 4.3. The efficiency of the algorithm to identify b jets in a $t\bar{t}$ event is measured by using Monte Carlo simulations. The different tagging performance seen between run 1A and run 1B data is discussed along with the acceptance calculations in the next chapter. The rest of the chapter is devoted to the tests of the reliability of the Monte Carlo tagging simulations. Section 4.4 describes the method by which the tagging performance in a large inclusive electron sample is evaluated. Results determine the ratio of tagging efficiencies between the sample of semileptonic b decays and Monte Carlo simulations. Section 4.5 reports on the first measurement of the tagging efficiency in the inclusive b decays directly from CDF

43
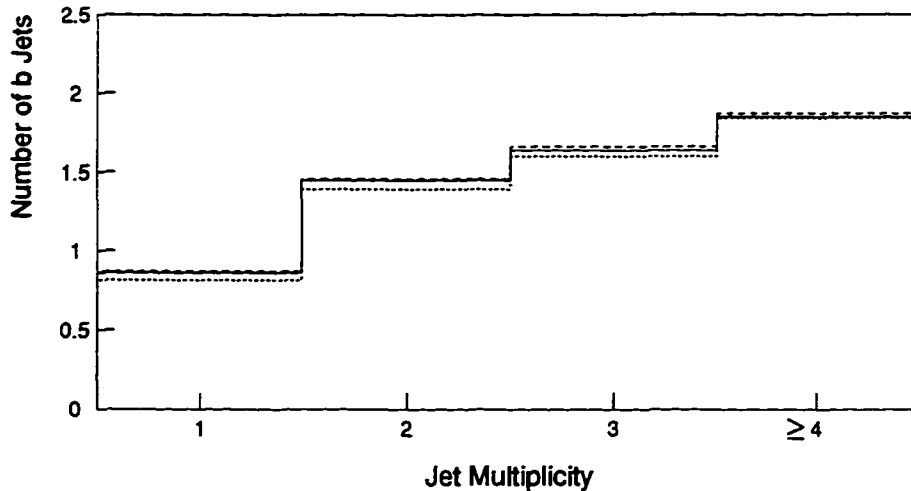
Figure 4.1: The expected number of b jets in each of the jet multiplicity bin for events passing the W selection criteria in $t\bar{t}$ events with top mass set to 165 GeV/c^2 (dot), 175 GeV/c^2 (solid), and 185 GeV/c^2 (dash).

data. The ratio of tagging efficiencies between the sample of inclusive b decays and Monte Carlo simulations is obtained. Both measurements show that the Monte Carlo simulations overestimate the tagging efficiencies in b hadron decays and therefore corrections must be made and applied to the simulation programs. Section 4.6 describes an improved detector simulation developed by correctly modeling the track-finding efficiency. The simulation is used to determine the tagging efficiency in Monte Carlo $t\bar{t}$ events in the next chapter. Observed tags in the W + multijet sample are summarized in section 4.7.

4.1 Vertices and Impact Parameters

4.1.1 Primary Vertex Finding

Precision measurement of the $p\bar{p}$ interaction point, called the primary vertex, results in a correct frame of reference for the event topology. In CDF detector the primary vertex position is measured by a weighted 3-dimensional fit of the SVX tracks with a starting point at z position obtained from the VTX detector measurements. The iterative process minimizes the residuals of the P_T-weighted tracks with respect to the fit point assuming

44

that most of the tracks in the event come from the primary vertex. Therefore the accuracy of the finding algorithm can be affected by the number of tracks used in the fit and the global event topology. A 20 μm uncertainty on the determination of primary vertex position in the transverse plane is estimated. The resolution of the primary vertex finding can be propagated into the measurement of the impact parameters which are used in the displaced vertex finding.

Approximately 72% of events in the inclusive W sample are accompanied by multiple primary interactions separated along the beamline. The event vertex is thus assigned to be the one with the largest P_T summed over the associated tracks. In the subsequent analysis only tracks extrapolating within 5 cm of the event vertex in the z-coordinate are used in order to exclude contributions from the multiple scattering.

4.1.2 Impact Parameter

Displacement of the tracks is described by the distance of closest approach of the track to the primary vertex in the $(r - \phi)$ plane, the impact parameter d. The uncertainty of the measurement can be parametrized as $\sigma_d = \sqrt{10^2 + 13^2 + (60/P_T)^2}$ μm, where these terms correspond to the uncertainties in the position of the $p\bar{p}$ interaction point, intrinsic SVX resolution and multiple scattering contributions.

The sign of the impact parameter, a convention preferentially chosen to indicate whether tracks are from displaced vertices, is determined according to the following prescription as shown in figure 4.2:

$$\text{sign of impact parameter} = \begin{cases} \text{positive,} & \text{if } \alpha < 90^\circ; \\ \text{negative,} & \text{if } \alpha > 90^\circ; \\ \text{zero,} & \text{otherwise.} \end{cases}$$

The positive sign is assigned to tracks that appear to come from the displaced vertices.

Negative signed impact parameters result from the resolution effects and mismeasurement of the direction of the jet. Tracks from zero-lifetime sources can have non-zero impact parameters which are randomly distributed in both positive and negative region due

45
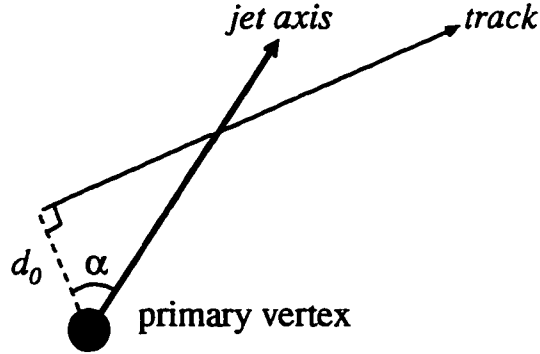
Figure 4.2: The sign of the impact parameter is determined according to the intersection of a track with a jet axis in the plane transverse to the beamline.

to resolution effects. Figure 4.3 shows the impact parameter significance, d/σ_d, distribution for jets in the 50 GeV jet-trigger sample. It is estimated that 90% [42] of the events in this sample are from zero-lifetime sources. Displaced tracks can also be mis-signed to have negative impact parameters if they are sufficiently mismeasured to be no longer consistent with having come from displaced vertices.

4.2 Bottom Quarks from Top Quarks Decay

Quarks produced with high momenta go through the fragmentation and decay processes. The hadronization of b quarks is described by an analytical form of the fragmentation functions introduced by Peterson $et\ al.$ [43], and final state radiation of "hard" gluons which can be incorporated into Monte Carlo generators. Decay spectrum of b hadrons including various charmed hadrons produced in the decays are also modeled by a Monte Carlo program which employs results from CLEO [44] experiments. A $t\bar{t}$ Monte Carlo generator level study reveals a significant component of distance projects into the plane transverse to the beamline for the b hadrons. This large distance is attributed to the energetic b quarks in

46
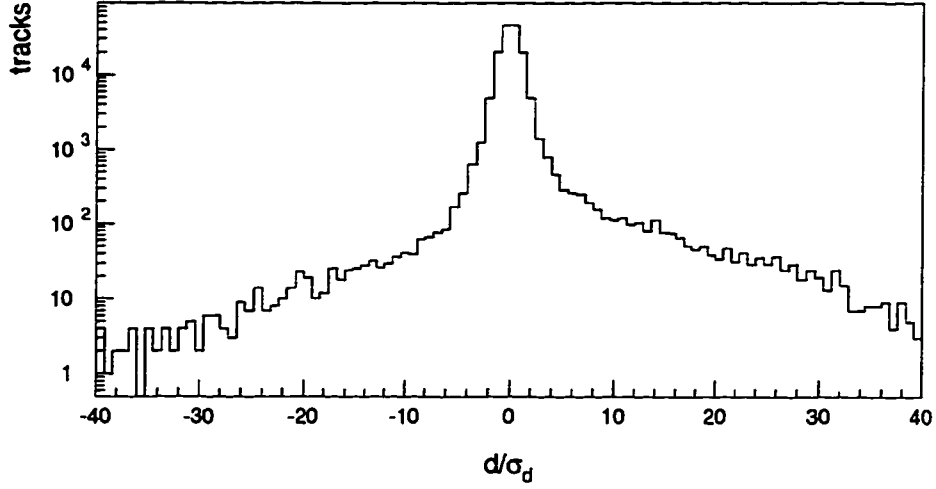
Figure 4.3: The d/σ_d distribution for tracks in the generic-jet sample.

the central pseudorapidity region from heavy top quark decay, along with the long b quark lifetime ($c\tau_b \sim 450\mu m$). Figure 4.4 shows the expected P_T and η distributions of the b quarks before detector resolution effects. The resulting transverse decay length distribution is show in figure 4.5. Therefore, tracks from b hadron decays are expected to be displaced from the interaction point and may be used to locate the secondary vertex.

4.3 Description of the Tagging Algorithm

A tagging algorithm has been developed to identify displaced tracks and vertices. Tracks inside of cone of radius 0.4 with respect to the jet axis are used in the algorithm and are classified into two categories by different selection criteria:

- Loose selection criteria for displaced tracks

  - track $P_T > 0.5$ GeV/c

  - $d/\sigma_d > 2.5$

  - at least one "good" hit (defined in section 2.4.3) for track with 3 or 4 SVX hits

47
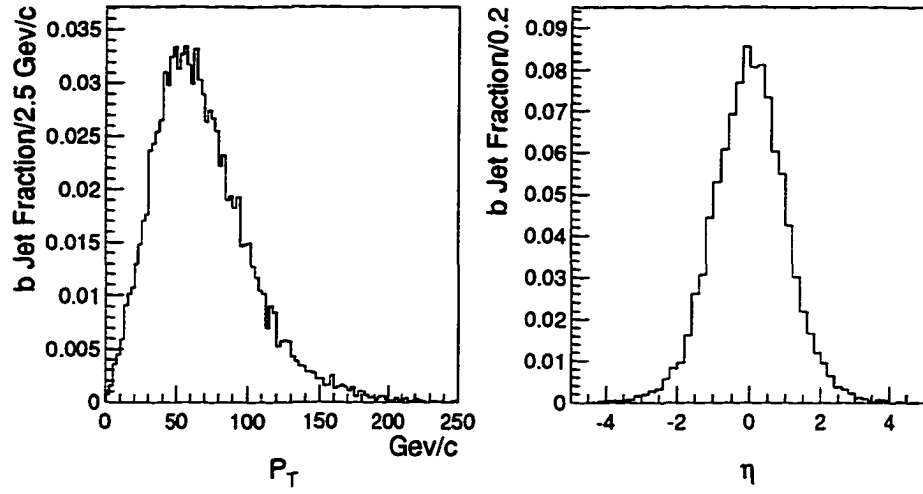
Figure 4.4: The P_T and pseudorapidity distributions for the b quarks in $t\bar{t}$ events with top mass set to 175 GeV/c^2.
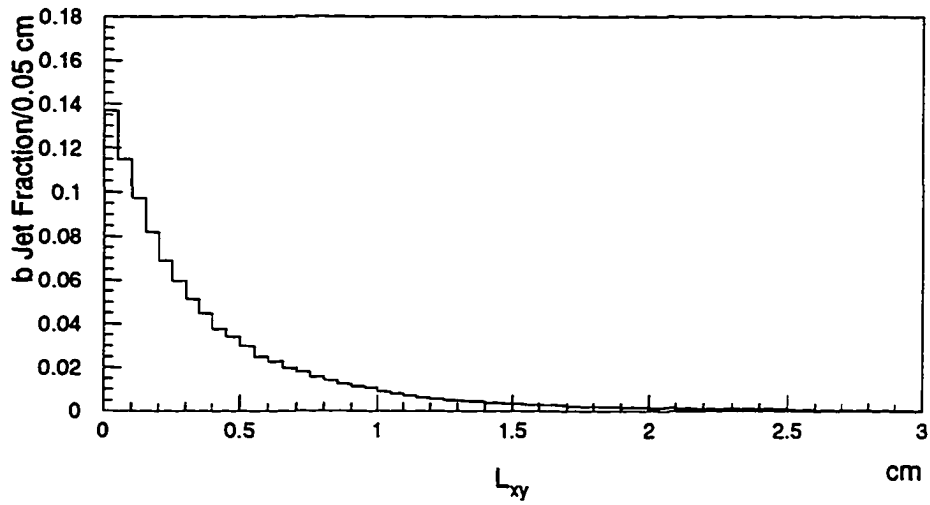
Figure 4.5: The transverse decay length distribution for the b hadrons in $t\bar{t}$ events with top mass set to 175 GeV/c^2.

48

- including tracks with 2 SVX hits only if $P_T > 1.5$ *GeV/c*, both have to be "good" hits found in either layer 0 and layer 1, or in layer 2 and layer 3 of the SVX detector

- excluding tracks from long-lived neutral particles such as K_s^0's and Λ's decays

- **Tight selection criteria for displaced tracks**

  - track $P_T > 1.5$ *GeV/c*

  - $d/\sigma_d > 3.0$

  - at least one "good" hit for track with 4 SVX hits

  - at least two "good" hits for track with 3 SVX hits

  - excluding track with only 2 SVX hits

  - excluding tracks from long-lived neutral particles such as K_s^0's and Λ's decays

The algorithm then employs a two-step sequence to search for the displaced vertices. The first step which is referred as "Pass 1" process applies relatively restrictive constrains to form the vertex using tracks passing the loose selection criteria described above. The second, referred as "Pass 2", uses tracks passing the tight selection criteria to form the vertex less restrictively. The Pass 2 process is performed only if there is no secondary vertex candidate found by Pass 1. The following specification describes the two passes.

- **Pass 1:** Tracks are selected using loose criteria. They are then ranked according to their P_T, d/σ_d and number of "good" SVX hits associated with the tracks. A vertex formed from the two best tracks where at least one of the tracks has $P_T > 2.0$ *GeV/c* is used as a seed to test the association of other tracks. The search ends with a secondary vertex candidate declared if at least one of the remaining tracks have $d/\sigma_d < 3.0$ with respect to the seed. Otherwise a new search is begun with the seed formed from a next ranking pair of tracks. If there is no secondary vertex candidate found after seeds from all track pairs have been used, the program begins to perform the Pass 2.

49

- **Pass 2:** At least 2 tracks passing tight track quality cuts are required in order to perform the process. The process begins with vertexing from all tracks, followed by excluding tracks that contribute $\chi^2 > 50$ in the fit. A new fit is performed and the procedure is repeated until no more tracks can be removed. In the end if there remain two or more tracks and at least one of those has $P_T > 2$ GeV/c, the corresponding vertex is declared to be the secondary vertex candidate.

A tag is found if the decay length of the secondary vertex candidate in the transverse plane, L_{xy}, is less than 2.5 cm and the significance $(L_{xy}/\sigma_{L_{xy}})$ is greater than 3.0. The decay length cut is applied in order to require the vertex inside the region of the radius of the SVX innermost layer.

4.4 Tagging Efficiency for Semileptonic b Decays

The tagging performance for the semileptonic b decays is evaluated in a large data sample containing electron events. The inclusive electron event has at least one electron passing the selection criteria described in section 3.1 except for the E_T threshold lowered to 8 GeV and no isolation requirement applied. The sample is enriched in $b\bar{b}$ events where an electron from the semileptonic b decay $(b \rightarrow eX)$ recoils against a jet from the other b. Events containing Z bosons, or possible W candidates ($\not{E}_T > 20$ GeV or electron isolation $I_{cal} < 0.1$) are removed from the sample in order to minimize the non-$b\bar{b}$ fraction.

Electron-jets are selected as jets containing the electron tracks, with $E_T > 10$ GeV, $|\eta| < 2.0$ and there existing at least one "away jet" in the events. The away-jets are those jets with $E_T > 15$ GeV and separated from the electron tracks in $(\eta - \phi)$ plane by $\Delta R \geq 2.5$. The requirement for the presence of the back-to-back away-jet is to meet the $b\bar{b}$ event topology. In the tagging studies, the electron-jets are further required to have at least 2 tracks passing the Pass 1 track selections except for the d/σ_d cut. Jets that pass this requirement are called taggable jets. The tagging efficiency is then calculated by counting the tagged jets among the taggable-jet subset.

50

There are 118,707 taggable electron-jets found in the sample. Among jets passing the tagging algorithm, 16,767 have positive decay lengths, and 765 have negative decay lengths. The tagging efficiency is then computed using a so-called "single-tag" method:

$$\epsilon_{b \to eX} = \frac{N^+_{tagged-e} - N^-_{tagged-e}}{N_e \times F_b}$$

where $N^+_{tagged-e}$, $N^-_{tagged-e}$ are the number of tagged electron-jets with positive and negative decay length; N_e is the total number of events in the sample; F_b is the fraction of electron-jets which come from semileptonic b-hadron decay. Number of tagged jets with negative decay length is used to estimate the mistag rate for the tagging algorithm in the electron sample. F_b is estimated to be $(39 \pm 5)\%$ [45] by measuring the yield of muons near the electrons in the cascade decay process $b \to e\bar{\nu}c \to e\mu X$. The tagging efficiency for jets from semileptonic b decays is measured to be 0.35 ± 0.04.

Another method to measure tagging efficiency for the semileptonic b decay is to use a subsample of 4,054 events in which the away-jets are required to be tagged. This increases the b purity in the subsample. Among this group 1,209 events also have electron-jets tagged. The tagging efficiency can be calculated from this "double-tag" method by:

$$\epsilon_{b \to eX} = \frac{N_{double}}{N^{tagged}_{away}}$$

where N^{tagged}_{away} is the number of events with away-jets tagged after corrected for mistags of non-b jets. The background subtraction is of order 20%. N_{double} is the number of events in which the electron-jets are also tagged. $\epsilon_{b \to eX}$ is measured to be 0.37 ± 0.03. Two complementary methods for measuring the tagging efficiency in semileptonic b decays provide consistent results as shown in figure 4.6(a). The errors shown with the single-tag point are dominated by the uncertainty of F_b, and the errors shown with the double-tag points are dominated by the limited number of double-tagged events and the uncertainty in the background subtraction.

The measurement is simulated using the HERWIG [46] generator. Events from the reaction $p\bar{p} \to b\bar{b}X$ are generated and processed through the CDF detector simulation. The decay spectrum of the b hadrons is modeled by the CLEO decay tables. The same electron

51
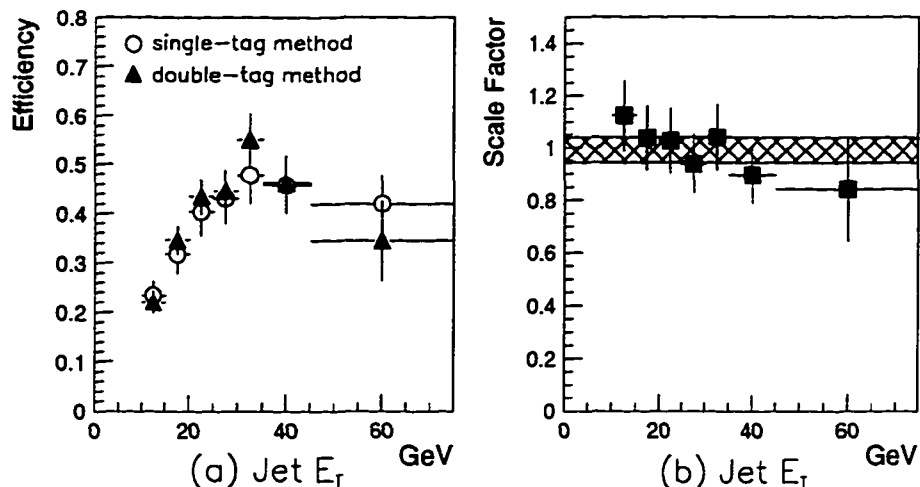
Figure 4.6: (a) The tagging efficiency for semileptonic b decays is plotted versus the E_T of the jet associated with the electron. (b) Ratios of tagging efficiencies between data and Monte Carlo. The shaded region is the $\pm 1\sigma$ bounds of a fit assuming no dependence on E_T.

event selection was used and the "single-tag" method was applied. The ratios of tagging efficiencies between data and Monte Carlo as a function of the E_T of the jet are shown in figure 4.6(b). The data points were the weighed average of results from two methods. A scale factor of 0.99 ± 0.05 obtained by fitting the distribution to a flat line is obtained. This value can be used to scale the Monte Carlo simulations to agree with that found in the data. This scaling method was first used in reference [3] for adjusting the b-tagging efficiency in the $t\bar{t}$ Monte Carlo.

However, scaling the tagging efficiency for b jets observed in the Monte Carlo $t\bar{t}$ events by the ratio may result larger errors. The systematic uncertainties come from the different E_T spectrum of b jets between the electron sample and $t\bar{t}$ events. The discrepancy is estimated to be ±0.20 by fitting the distribution to a sloped line and taking half of the difference between the results at the average E_T of the b jet in the Monte Carlo $t\bar{t}$ sample. In addition, the scale factor determined in semileptonic b decays can be different from those in $t\bar{t}$ events where b decays are totally inclusive. The application to $t\bar{t}$ events of a scale factor determined from events so dissimilar is clearly fraught with uncertainty. In the next

52

section an approach that attempts to directly measure the scale factor from the inclusive b decays will be presented.

4.5 Tagging Efficiency for Inclusive b Decays

An inclusive-jet sample enhanced in b quark decays can be obtained in the electron dataset by selecting jets separated from the electron tracks in $(\eta - \phi)$ plane by $\Delta R > 1.0$. The inclusive jet sample contains b, c, and jets from non-heavy sources (referred as primary jets) in which the b decays inclusively. The number of inclusive-jets tagged, $N_{inclusive}^{tagged}$, observed in the sample can be calculated as

$$N_{inclusive}^{tagged} = N_{inclusive} \cdot \{f_b \cdot \epsilon_b + f_c \cdot \epsilon_c + f_p \cdot \epsilon_p\}$$
$$= N_{inclusive} \cdot \{f_b + f_c \cdot (\frac{\epsilon_c}{\epsilon_b}) + f_p \cdot (\frac{\epsilon_p}{\epsilon_b})\} \cdot \epsilon_b$$

where $N_{inclusive}$ is the total number of inclusive jets; $f_{b,c,p}$ are the fractions of the b, c, primary jets in the sample; $\epsilon_{b,c,p}$ are the tagging efficiencies for the inclusive b, c decays and primary jets. Therefore ϵ_b can be measured if fractions of heavy flavor contents and relative tagging performances are known.

Fractions of each flavor components, $f_{b,c,p}$, are estimated using a jet probability algorithm [47]. The algorithm assigns a track-probability to each track associated with the jet based on its signed impact parameter. The probability predicts that the track is consistent with originating from the primary vertex. The track probabilities are then combined into an overall "jet probability" which shows the jet is consistent with the zero lifetime hypothesis. By fitting the jet probability distribution to that expected from b, c, and primary jets, the fractions of each flavor component in the sample can be obtained [48]. The success of the technique depends on the reliability of the Monte Carlo models for the jet probability distributions. The details of the jet probability algorithm and a test for the fitting method are described in the appendix B. Table 4.1 summarizes the b, c, and primary jet contents as measured in the inclusive-jet sample. The errors shown include uncertainties from the fitting method and statistical errors.

53

E_T(GeV)	10-15	15-20	20-25	25-30	30-35	35-45	45-
b (%)	8.4±0.4	13.4±0.5	14.5±0.6	15.5±0.9	13.4±1.1	13.3±1.1	9.1±1.3
c (%)	13.8±0.7	6.0±0.9	5.7±1.2	$1.3^{+1.6}_{-1.3}$	4.3±2.1	2.9±2.2	12.4±3.4
p (%)	77.8±15.6	80.6±16.2	79.9±16.0	83.2±16.7	82.3±16.6	$83.8^{+16.2}_{-16.9}$	78.5±16.0

Table 4.1: b, c, and primary jet contents measured in the inclusive-jet sample.

E_T(GeV)	10-15	15-20	20-25	25-30	30-35	35-45	45-
ϵ_c/ϵ_b (%)	30.2±1.3	29.7±1.4	27.1±2.0	25.2±2.9	24.9±4.2	26.6±5.1	29.5±13.8
ϵ_p/ϵ_b (%)	0.5±0.2	0.7±0.2	0.7±0.2	0.9±0.1	1.0±0.2	1.0±0.1	1.5±0.3

Table 4.2: Tagging ratios studied in the Monte Carlo samples. Errors reflect Monte Carlo statistics only.

Ratios of tagging efficiencies between inclusive c to b decays (ϵ_c/ϵ_b), and between primary jets to inclusive b decays (ϵ_p/ϵ_b) are measured in Monte Carlo samples. The ratios for each jet E_T bin is shown in table 4.2. These ratios are directly obtained from the simulations without any correction applied. The tagging efficiency for c and primary jets rely on the Monte Carlo modeling throughout the analysis.

There are 239,457 inclusive-jets found in the sample, among those 10,943 jets are tagged. Tagging efficiencies measured for inclusive b decays in data using the method described above and the ratios between data and the corresponding Monte Carlo as a function of the jet E_T are shown in figure 4.7. A scale factor for inclusive b decays is measured to be 0.83±0.03 by fitting the distribution to a flat line. It is estimated an uncertainty ±0.14 occurs in scaling the tagging efficiency for b jets in the Monte Carlo $t\bar{t}$ events due to the different E_T spectrums.

The scale factors used to extrapolate the tagging efficiency for b jets are found to be different in the semileptonic and inclusive b decays. Two effects can account for the discrepancy. The electron-jets used in the studies of semileptonic b decays must contain one well-identified track, the electron track. This can result better vertexing performance

54
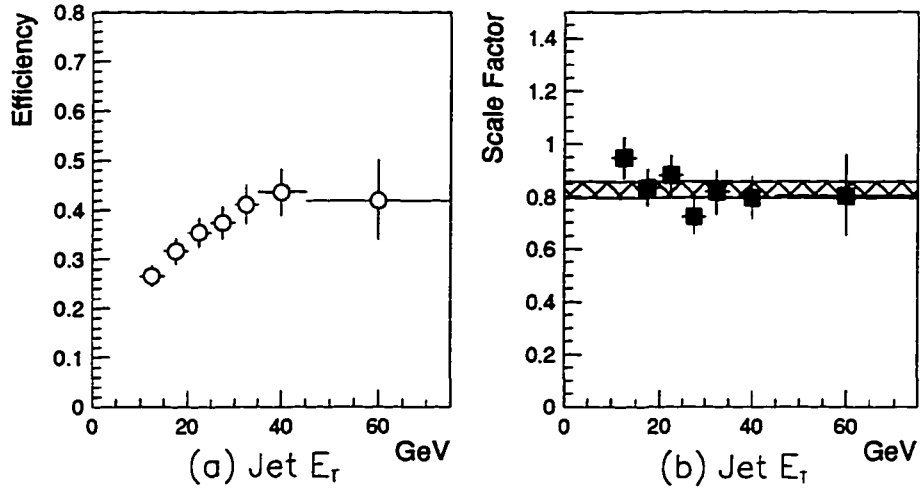
Figure 4.7: (a) The tagging efficiency for inclusive b decays, is plotted versus the E_T of the inclusive-jet. (b) Ratios of tagging efficiencies between data and Monte Carlo. The shaded region is the $\pm 1\sigma$ bounds of a fit assuming no dependence on E_T.

though the bias has been minimized by the requirement that the jets used in both studies have to be "taggable". On the other hand, the neutrinos from the semileptonic b decay are undetectable and the electron-jet may have one less track to be used in the vertexing. The relative sizes of the two effects are not well known.

Furthermore, limited by the statistics for high E_T jets in the inclusive electron data, two methods are unable to provide a full crosscheck for the tagging performance in higher E_T region. It is seen from figure 4.6 and 4.7 that there exist larger statistical errors in the high E_T bins where an increasing fraction of b jets result from $t\bar{t}$ events. Again, use of the scale factor in the region where it is poorly determined is dubious. A complementary method which attempts to improve the detector simulations program to ameliorate these effects is then developed.

4.6 Monte Carlo Tagging Efficiency Measurement

The scale factor studies indicate that there exists discrepancies in the simulation program. Several effects from physics and detector simulations are investigated. Among

those are the b lifetime, fragmentation in b hadron decay, SVX resolution and detector tracking efficiency effects. Examination of the sensitivity of the tagging efficiency with changes in the details of the analysis has revealed that only tracking efficiency strongly effects the outcome. This is consistent with a conclusion that the tagging efficiency is related to the tracking efficiency. Thus any difference found in the tracking efficiency between data and Monte Carlo results in a difference in the overall tagging efficiency.

In order to represent the tagging performance in the Monte Carlo programs, a precise modeling for the tracking efficiency must be used in the detector simulations. The task is achieved by applying an overall scale factor to the track-finding efficiency. For this work the track-finding efficiency in data is measured using Monte Carlo tracks embedded into the data sample. A random track passing certain selection cuts is merged into jet data, followed by the reconstruction of the events. The track-finding efficiencies measured in CTC and SVX are calculated by counting the embedded Monte Carlo tracks. In measuring the Monte Carlo track-finding efficiency, only tracks coming from the primary vertex are used. The degradation is then obtained by comparing the CTC and SVX track-finding efficiencies between data and Monte Carlo simulations. The scaling is parametrized as a function of the density of hits around the object track, and incorporated into the tagging algorithm. The advantage of this method is its avoidance of the statistical limitation on the high E_T jets. The degradation can be used without the uncertainty that results from the E_T spectrum of b jets. A check of the degradation method is presented in appendix C where the systematic uncertainty is estimated to be relative 7%.

Figure 4.8 and 4.9 show the tagging efficiencies for the semileptonic and inclusive b decays in electron events which are obtained with the track-finding degradation. The scale factor is measured to be 0.93 $\pm$ 0.02 and 0.89 $\pm$ 0.04 for the semileptonic and inclusive b decays respectively. Results are consistent with those measured using methods described in the previous two sections. In the measurement of the $t\bar{t}$ production cross section described in this dissertation, the efficiency for tagging at least one jet in a $t\bar{t}$ event will be measured using the Monte Carlo simulations where the track-finding efficiency has been degraded.
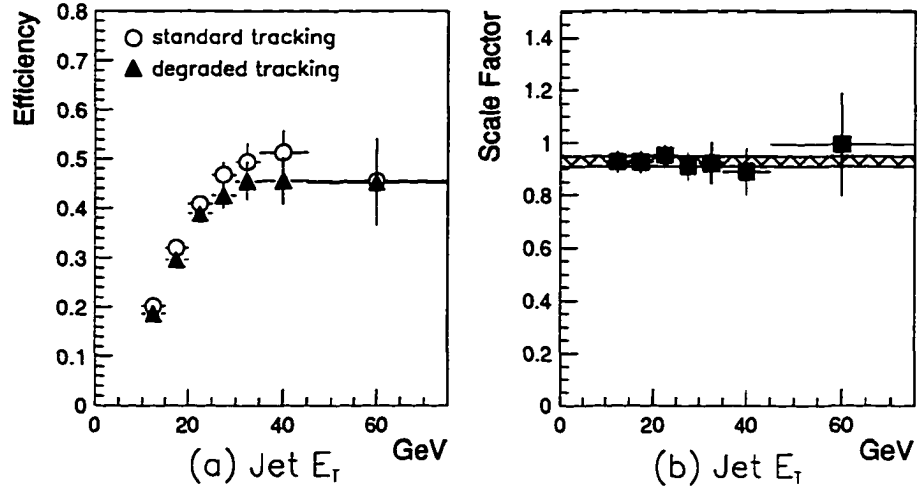
Figure 4.8: (a) Tagging efficiencies for semileptonic b decays determined using Monte Carlo simulations. (b) Ratios of tagging efficiencies are plotted versus the jet E_T. The shaded region is the $\pm 1\sigma$ bounds of a fit assuming no dependence on E_T.
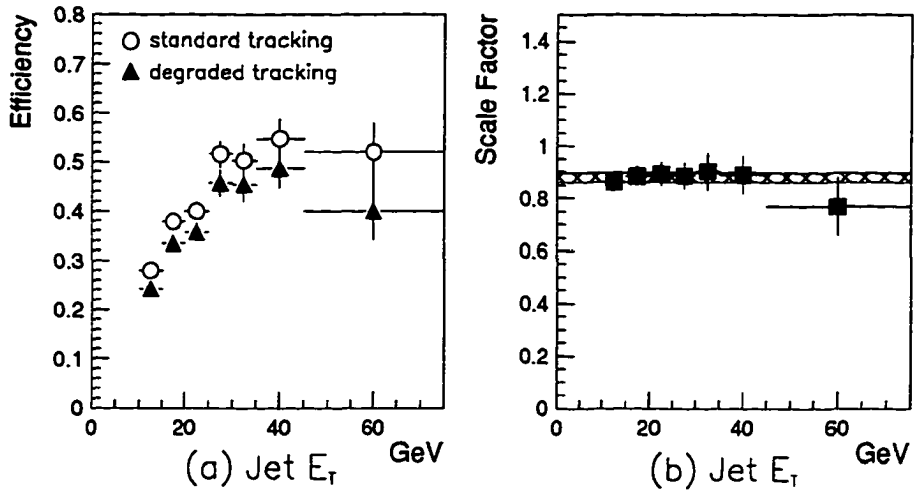
Figure 4.9: (a) The tagging efficiency for inclusive b decays determined using Monte Carlo simulations. (b) Ratios of tagging efficiencies are plotted versus the jet E_T. The shaded region is the $\pm 1\sigma$ bounds of a fit assuming no dependence on E_T.

57

	W + 1 Jet	W + 2 Jets	W + 3 Jets	W + ≥4 Jets
Tagged Events				
Positive-tagged	70	46	18	16
Negative-tagged	19	9	2	0
Tagged Jets				
Positive-tagged	70	52	24	18
Negative-tagged	19	9	2	0

Table 4.3: Summary of observed tagged events and jets in the W + jets samples.

4.7 Observed Tags in the W + Multijet Sample

It has been shown that the tagging algorithm is able to identify the b jets with good efficiency and that Monte Carlo program can reproduce the performance. Applying the tagging algorithm on the W + $\geq$ 3 jets sample, 34 events are found to have at least 1 jet tagged with positive decay length and 2 events have jets tagged with negative decay length. Tags observed in the inclusive W + jets sample are summarized in table 4.3. The $c\tau$ distribution for the vertexed jets shown in figure 4.10 is consistent with jets primarily from b jets. Distribution for the 36 events with at least 1 jet tagged in the W + $\geq$ 3 jets $t\bar{t}$ search sample is also highlighted. Expected tags from a variety of sources besides $t\bar{t}$ events as well as kinematics of these tagged jets are discussed in the next chapter.
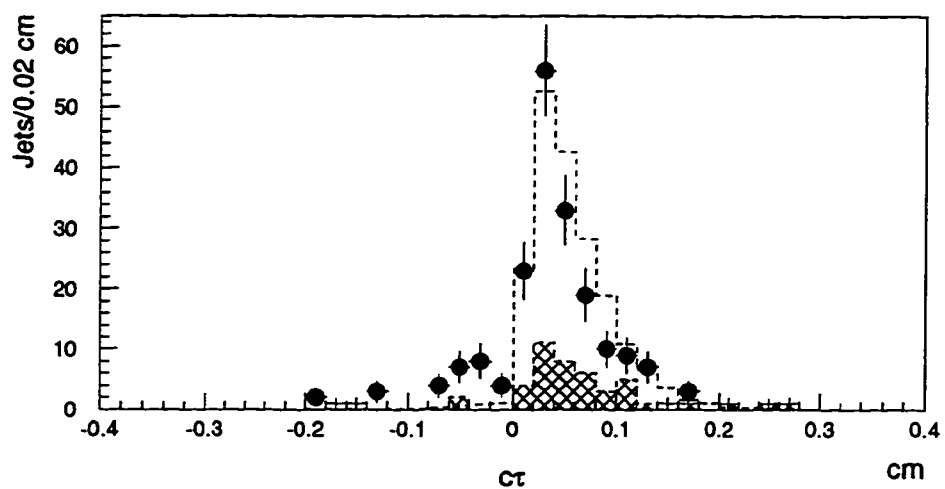
Figure 4.10: The $c\tau$ distributions for jets with a secondary vertex in the W + jets data (points with errors) compared to b jets in Monte Carlo $t\bar{t}$ events (histogram normalized to data). The shaded histogram is the W + $\geq$ 3 jets tags in the data.

59

Chapter 5

The Acceptance Calculations

5.1 Luminosity

Integrating the instantaneous luminosity over the course of the data run is needed in the measuring the $t\bar{t}$ production cross section. The instantaneous luminosity is defined as the production rate of a given final state divided by the cross section for producing that final state. Since this rate is the same for all final states, a known process can be used to determine the luminosity. At CDF, the instantaneous luminosity is obtained by counting the rate of a specific process, the Beam-Beam Counters (BBC) coincidences, for which cross section is known. The BBC consists of two sets of planes near the beampipe covering the far forward and backward regions as described in chapter 2.2.5. The rates of coincident hits in both counters divided by the effective cross section for BBC events gives the luminosity values.

To measure the cross section for BBC events, σ_{BBC}, one has to perform a normalization of the raw counter rates. The BBC events are considered a sample of elastic, inelastic and diffractive $p\bar{p}$ interactions with backgrounds from secondary scattering of particles back into the counters or other accidental processes. The background events result from the amount and type of the material between the $p\bar{p}$ collision point and the counters. To obtain the normalization of the BBC rate to σ_{BBC}, data collected from a special run in 1989 for measuring the $p\bar{p}$ total cross section was used. The normalization can be expressed

60

as:

$$\sigma_{BBC} = \sigma_{p\bar{p}} \cdot \frac{N_{BBC}^{vis}}{N_{p\bar{p}}}$$

where $\sigma_{p\bar{p}}$ is the $p\bar{p}$ total cross section; $N_{p\bar{p}}$ is the number of total events from the $\sigma_{p\bar{p}}$ measurement; N_{BBC}^{vis} is the number of events in the same run counted by the BBC.

The $p\bar{p}$ total cross section is measured independently and documented in references [58, 59, 60]. The cross sections for $p\bar{p}$ elastic, inelastic and single diffractive processes are measured separately. Therefore breaking the total event count $(N_{p\bar{p}})$ into elastic scattering events (N_e), single diffractive scattering events (N_d), and double inelastic events (N_i):

$$N_{p\bar{p}} = N_e + N_d + N_i$$

the cross section σ_{BBC} is re-written according to reference [59] as:

$$\sigma_{BBC} = \frac{16\pi(\hbar c)^2}{1 + \rho^2} \cdot \frac{dN_e/dt|_{t=0}}{N_i + N_d + N_e} \cdot \frac{N_{BBC}^{vis}}{N_i + N_d + N_e}$$

where t is the momentum exchange squared in the interaction and ρ is the inelasticity of the interaction. The $p\bar{p}$ total cross section measurement provides the necessary components used in the calculations and yields the final result $\sigma_{BBC} = 51.2 \pm 1.7$ mb [61].

The instantaneous luminosity is then calculated as

$$\mathcal{L} = \frac{-f_0}{\sigma_{BBC}} \cdot ln(1 - \frac{R}{f_0})$$

where R is the BBC count rate; $f_0^{-1} \sim 3.5$ μsec is the beam crossing period and the log term represents a poisson correction for the possible multiple interactions. Uncertainties of the measurement are therefore dominated by the errors in the $p\bar{p}$ total cross section and the BBC detector resolutions. Figure 5.1 (a) displays the distribution of instantaneous luminosities obtained from the run 1B W + jets and electron samples.

By integrating the luminosity over the course of the data run, the run 1A and run 1B integrated luminosity are measured to be 19.3 ± 0.7 and 90.1 ± 7.2 pb^{-1} respectively. The uncertainties include additional errors from beam interactions with the residual gas in the beam pipe and variations between stores. These numbers are used as inputs in the calculations of $t\bar{t}$ production cross section.

61
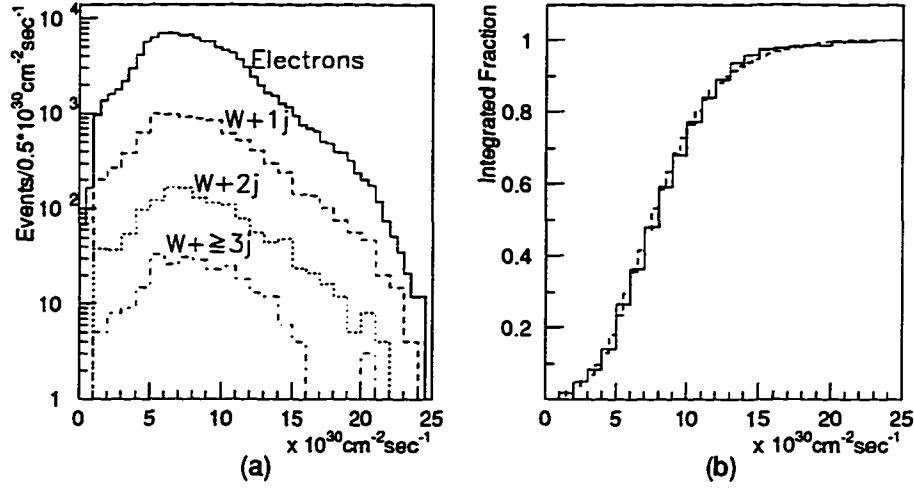
Figure 5.1: (a) The instantaneous luminosity fractions for the run 1B W + jets and the electron events. (b) The integrated fraction for the instantaneous luminosity in the $W + \geq$ 3 jets sample (solid line) and in the electron data (dash line).

5.2 The $t\bar{t}$ Event Detection Efficiency

This section describes the computation for the fraction of $t\bar{t}$ events can be detected using the selection criteria described in the previous chapters. The calculation is factorized into independent terms which are determined by either data control samples or Monte Carlo simulations. The total $t\bar{t}$ events detection efficiency, $\epsilon_{t\bar{t}}$, can be expressed as:

$$\epsilon_{t\bar{t}} = A_{t\bar{t}} \cdot \epsilon_{trigger} \cdot \epsilon_{tag}$$

where

- $A_{t\bar{t}} \equiv$ the fraction of $t\bar{t}$ events within the geometric acceptance of the CDF detector and passing the event selection except for the trigger requirement

- $\epsilon_{trigger} \equiv$ the trigger efficiency for identifying $t\bar{t}$ events in the "lepton plus jets" channel

- $\epsilon_{tag} \equiv$ the efficiency for tagging at least one jet in the event

In the following sections, each term is measured separately with top mass assumed to be 165, 175, and 185 GeV/c^2. Uncertainties are also discussed.

62

Jet Multiplicity	W + 1 jet	W + 2 Jets	W + ≥ 3 Jets
$M_{top} = 165\ GeV/c^2$	0.007±0.001	0.029±0.001	0.115±0.002
$M_{top} = 175\ GeV/c^2$	0.005±0.001	0.030±0.001	0.120±0.002
$M_{top} = 185\ GeV/c^2$	0.004±0.001	0.026±0.001	0.125±0.002

Table 5.1: The fraction of $t\bar{t}$ events passing all event selection criteria except for the trigger requirement as predicted in Monte Carlo samples with top mass set to 165, 175, and 185 GeV/c^2. Errors shown are statistical only.

5.2.1 Determination of $A_{t\bar{t}}$

The geometric acceptance and event selection efficiency, $A_{t\bar{t}}$, is simulated in Monte Carlo samples with corrections applied for differences seen between data and simulations. The Monte Carlo events are generated using Herwig with top mass set to 165, 175, and 185 GeV/c^2 and passed the same selection criteria as used for data after the detector simulations. Table 5.1 shows the fractions of $t\bar{t}$ events that should be observed in each jet multiplicity bin according to the simulation study. Some correction factors obtained from the comparison between data control samples and Monte Carlo events are needed to scale the fractions. These include the different efficiencies for the event vertex cut $|Z_{vertex}| < 60\ cm$ and the lepton identification cut.

The distributions of the z position of the primary vertex in the run 1B $W \to \mu\nu$ data before the fiducial cut is shown in figure 5.2. It is found that the Monte Carlo always generates events within 60 cm from the detector center along the z axis while data shows there exist events outside the region. Performing an integration on the data points, the area method, from the distribution yields an efficiency of 0.946 ± 0.001 (statistical error only) for the fiducial cut. A relative 2% systematic uncertainty is assigned assuming the distribution is flat as functions of the jet multiplicity and the luminosity. When normalized with the run 1A number of 0.956 ± 0.011 [36], the combined efficiency for all the runs is estimated to be 0.948 ± 0.018.

To calculate the correction factor for the lepton identification, efficiencies measured
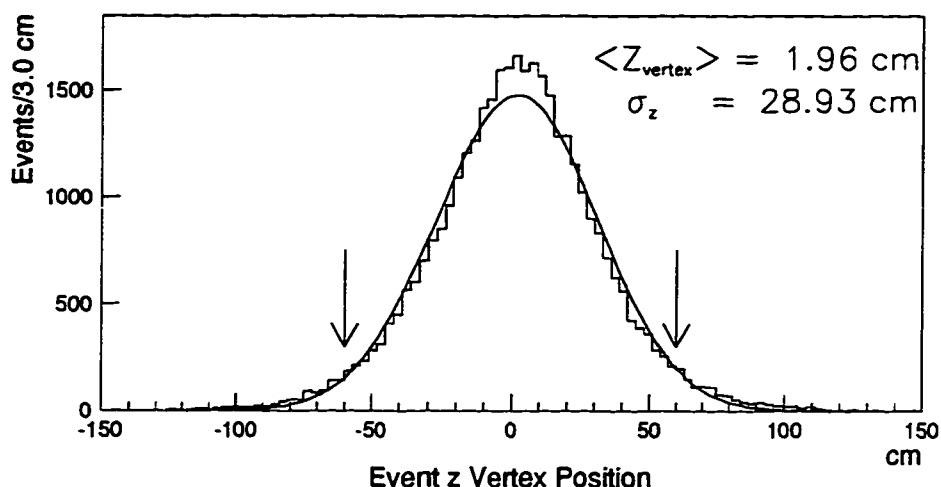
Figure 5.2: The distribution for z-coordinate of the run 1B inclusive W event vertex before the fiducial cut. The results of a fit to a Gaussian are also displayed. The arrows indicate the cut values of ± 60 cm.

from Monte Carlo $W \to e\nu$, $\mu\nu$ samples are compared to those from data $Z \to ee$, $\mu\mu$ events [62]. The Z samples are used because leptons come from W and Z events are both isolated, and one can examine the second leg of Z decays to obtain the identification efficiencies. Scale factors of 0.866 ± 0.011 for electrons and 0.924 ± 0.016 for muons are obtained. Weighed by the ratio of electron and muon events in the $W + \geq 1$ jet data sample, a combined correction factor of $R_{lepton} = 0.890 \pm 0.013$ is found.

Uncertainties resulting from the jet multiplicity modeling as well as the jet energy scale are also considered. Monte Carlo samples with the initial and final state radiation simulations are used to measure the uncertainty of the jet multiplicity modeling. Errors are estimated by taking half of the difference in of $A_{t\bar{t}}$ between default Monte Carlo and that with radiation simulation turned off. A relative uncertainty of 7.0% is found. Uncertainty due to the jet energy scale is estimated to be 7% in the reference [63]. Combining all available information, table 5.2 shows $A_{t\bar{t}}$ in the $W + \geq 3$ jets bin for several top quark masses for the combined run 1A and run 1B data samples.

64

	$M_{top} = 165\ GeV/c^2$	$M_{top} = 175\ GeV/c^2$	$M_{top} = 185\ GeV/c^2$
raw $A_{t\bar{t}}$	0.115 ± 0.011	0.120 ± 0.012	0.125 ± 0.012
$\epsilon_{|Z_{vtx}|}$	0.948 ± 0.018	0.948 ± 0.018	0.948 ± 0.018
R_{lepton}	0.890 ± 0.013	0.890 ± 0.013	0.890 ± 0.013
$A_{t\bar{t}}$	0.097 ± 0.010	0.101 ± 0.010	0.105 ± 0.011

Table 5.2: The fractions of $t\bar{t}$ events passing all event selection criteria (except for the trigger requirement) after corrections for the event vertex cut and lepton identification efficiencies.

5.2.2 Determination of $\epsilon_{trigger}$

The acceptance study described above does not include the trigger requirement. The (Level 1 × Level 2) and Level 3 trigger efficiencies are measured separately for electron and muon events in unbiased data samples described in reference [64]. The trigger studies assume that the electron data and muon data are not correlated. One can study the electron trigger performance in muon data and vice versa.

The (Level 1 × Level 2) electron trigger is estimated to be $\sim$ 100% efficient from an .OR. of electron triggers and $\not{E}_T$ trigger. To study the Level 3 electron trigger, an unbiased data sample is needed. The sample is selected by requiring events pass the Level 3 muon triggers contain electrons passing all the electron identification cuts including the Level 2 electron trigger requirement with the exception of the isolation cut. By counting events among this group that also exhibit a Level 3 electron trigger, the Level 3 electron efficiency is measured to be 0.987 ± 0.003 (stat).

The (Level 1 × Level 2) muon trigger efficiency is obtained by simulating the trigger algorithms. The efficiency is estimated to be 0.899 ± 0.009 (stat). Using the method employed to measure the electron trigger, the Level 3 muon trigger is examined in an inclusive electron sample containing muons. The efficiency is found to be 0.970 ± 0.007 (stat). Combining the Level 1, Level 2 and Level 3 results leads to a muon trigger efficiency of 0.872 ± 0.009 (stat).

When the electron and muon trigger efficiencies are weighted by the number of

65

Jet Multiplicity	W + 1 jet	W + 2 Jets	W + $\geq$3 Jets
b jets per event	0.860	1.449	1.753
c jets per event	0.023	0.109	0.368
p jets pre event	0.117	0.442	1.568
b tags per event	0.238	0.405	0.501
c tags per event	0.001	0.006	0.023
p tags pre event	0.001	0.002	0.003

Table 5.3: Number of b, c and non-heavy flavor jets and tags expected in $(t\bar{t} \to W + \text{jets})$ events.

events in each category of the W + $\geq$ 1 jet sample, a composite trigger efficiency of 0.935 $\pm$ 0.09 with relative 10% uncertainty is assigned (See reference [64] for more details).

5.2.3 Determination of ϵ_{tag}

As shown in previous chapter, the tagging efficiency in electron data samples has been measured using different techniques. Good agreement is found between simulations and measured data. The semileptonic b decays as well as the inclusive b decays are well modeled by the Monte Carlo programs where improved track-finding simulations are needed. This method is selected for determination of the $t\bar{t}$ event tagging efficiency in the analysis.

Note the tagged jets are not required to be b jets in the simulations. The charm and non-heavy flavor jets in the $t\bar{t}$ events can also be tagged. Table 5.3 shows number of b, c and non-heavy flavor jets as well as tags expected in a $(t\bar{t} \to W + \text{jets})$ sample. The efficiency for tagging at least one jet in a $t\bar{t}$ event in the W + $\geq$ 3 jets sample as a function of top mass is plotted in figure 5.3. It is found that the central values of the tagging efficiencies varies within 3% between 160 GeV/c^2 and 190 GeV/c^2 and shows little dependence on the top mass. Table 5.4 summaries the efficiency numbers predicted in each of the jet multiplicity bin.

Beside the relative 7% uncertainty resulting from using the the Monte Carlo programs to measure the tagging efficiency as described in appendix C, variations due to the

66

Jet Multiplicity	W + 1 jet	W + 2 Jets	W + ≥ 3 Jets
$M_{top} = 165\ GeV/c^2$	0.198±0.018	0.324±0.009	0.396±0.005
$M_{top} = 175\ GeV/c^2$	0.240±0.016	0.356±0.008	0.420±0.004
$M_{top} = 185\ GeV/c^2$	0.232±0.022	0.361±0.010	0.414±0.005

Table 5.4: The run 1B event tagging efficiencies predicted in the Monte Carlo samples. Errors shown are statistical only.

luminosity dependence are also examined. It has been shown in the figure 5.1 (b) that the integrated fraction of the instantaneous luminosity in the top signal sample, the W + $\geq$ 3 jets sample, agrees well with that in the electron data. Therefore one can examine the dependences on luminosity for the tagging efficiency in the W samples by checking the tagging rate in the electron data. Figure 5.4(a) shows the tag rates in the jets associated with electrons as functions of instantaneous luminosity. Note that less than 2.5% of the data was collected with instantaneous luminosity greater than $15 \times 10^{30}\ cm^{-2}sec^{-1}$ and the distribution is consistent with a flat tagging efficiency with relative uncertainties measured to be less than 1.0%. The dependence on the integrated luminosity is also shown in 5.4(b). Variations due to the increased track multiplicity of events with high instantaneous luminosity or radiation damage to the SVX detector during the data-taking are small compared to the total uncertainty. A total of 10% relative uncertainty is assigned to the event tagging efficiency.

The run 1A event tagging efficiency is different from that of run 1B. With several upgrades to the silicon vertex detector and less radiation damage, the tagging algorithm is more efficient when applied on run 1B data. Studies [65] show the average b tagging efficiency in run 1A data is (86 ± 4)% of that in run 1B data. This leads to a 0.320 ± 0.096 run 1A event tagging efficiency in $t\bar{t}$ events. The different event tagging efficiencies are used separately in the calculations of the $t\bar{t}$ production cross section. Weighed by the integrated luminosity, the event tagging efficiency for whole run is measured to be 0.402 ± 0.052 with top mass assumed to be 175 GeV/c^2.

67
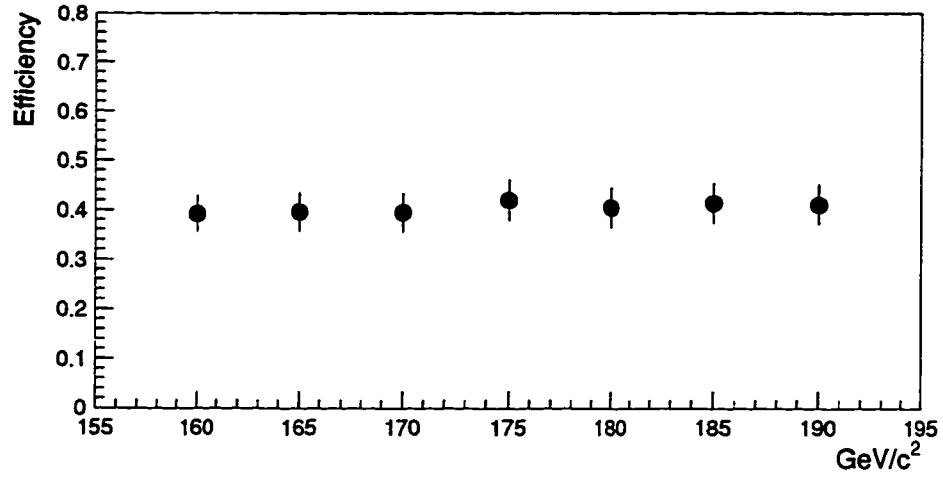
Figure 5.3: The event tagging efficiency in the run 1B $t\bar{t}$ Monte Carlo samples as a function of top mass are plotted. All tags from b, c and non-heavy flavor sources are counted.
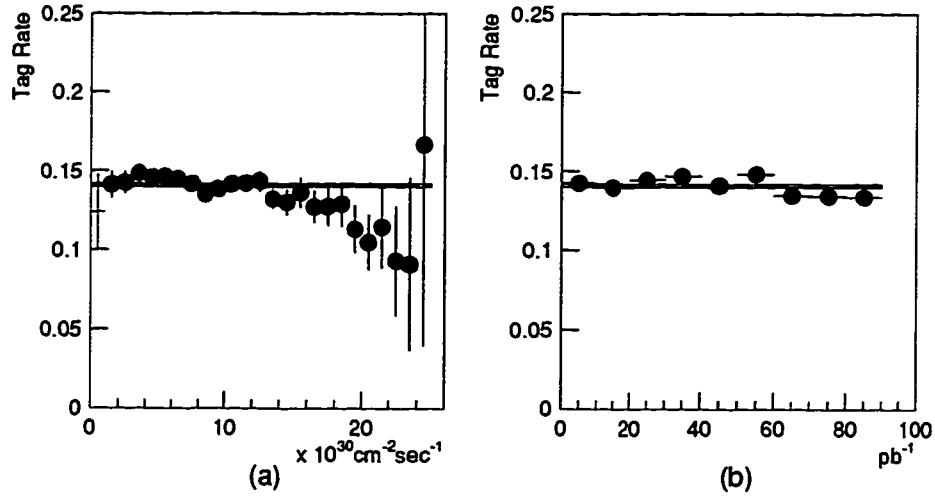
Figure 5.4: The tag rates in the run 1B inclusive electron data are plotted versus the (a) instantaneous and (b) integrated luminosity. The shaded regions are the $\pm 1\sigma$ bounds of a fit assuming no dependence on the instantaneous and integrated luminosity.

68

	$M_{top} = 165\ GeV/c^2$	$M_{top} = 175\ GeV/c^2$	$M_{top} = 185\ GeV/c^2$
$A_{t\bar{t}}$	0.097 ± 0.010	0.101 ± 0.010	0.105 ± 0.011
$\epsilon_{trigger}$	0.935 ± 0.094	0.935 ± 0.094	0.935 ± 0.094
ϵ_{tag}	0.383 ± 0.048	0.402 ± 0.052	0.397 ± 0.051
$\epsilon_{t\bar{t}}$	0.035 ± 0.007	0.038 ± 0.007	0.039 ± 0.008

Table 5.5: The total $t\bar{t}$ event detection efficiency. All uncertainties include statistical and systematic errors.

5.2.4 Summary

The total $t\bar{t}$ event detection efficiency for different top masses are summarized in table 5.5. The acceptances rise with the top mass as one would expect. This is mostly due to the increase of the fraction of events passing the kinematic requirement of ≥ 3 jets cut in the selection criteria. Less than 4% of the $t\bar{t}$ events with top mass between 165 and 185 GeV/c^2 can be identified using the method described in this dissertation.

69

Chapter 6

Background to $t\bar{t}$ Production

Jets identified by the tagging algorithm in the W + jets sample are either heavy flavor tags or the fake tags. Events containing heavy flavor content produced in association with the W, or from non-W sources passing the W + jets sample selection provide tags from b and c hadrons besides $t\bar{t}$ decays. These processes include W production with gluons splitting into heavy quark pairs ($Wb\bar{b}$ and $Wc\bar{c}$), $p\bar{p} \rightarrow W$ + charm , WW and WZ production, or non-W mechanism such as Z + heavy flavor, $Z \rightarrow \tau\tau$, and $b\bar{b}$ production. Background to $t\bar{t}$ production resulting from single top production is also considered. Fake tags originating from track mismeasurement are dominated by the non-heavy flavor tags with fewer mistags from b and c hadrons observed. In this chapter, the contribution from each individual process is computed separately for run 1B data and combined with those for run 1A, documented in reference [49], into final numbers. The calculations are based on the assumption that there are no $t\bar{t}$ events in the W + jets sample. Errors resulting from this assumption can be removed in the final calculation of the $t\bar{t}$ cross section. A comparison of kinematics features between data and predictions are presented in the end of the chapter.

6.1   The Mistags Background

The mistags background in the W + jets sample resulting from the track mismeasurement is determined using parameterization of the $x - y$ projected decay length, L_{xy},

70
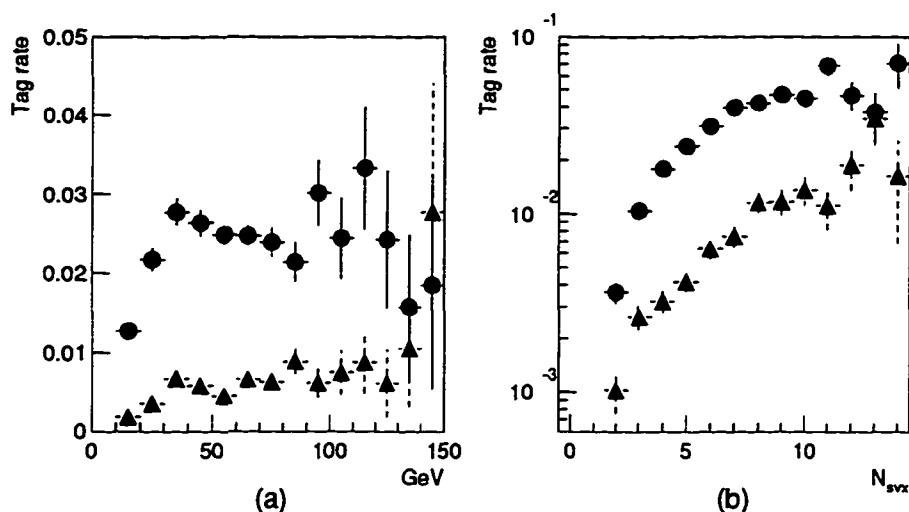
Figure 6.1: The positive tag rate (circle) and negative tag rate (triangle) as functions of (a) Jet E_T and (b) Number of good SVX tracks.

derived from the generic jet sample. The $+L_{xy}$ and $-L_{xy}$ tag rates can be parametrized based on the E_T of the tagged jet and associated number of good SVX tracks. The positive and negative L_{xy} tag rates as functions of jet E_T and number of good SVX tracks in the run 1B 50 GeV jet-trigger sample are shown in figure 6.1. The excess of positive tags is consistent with the presence of heavy flavor b and c in the generic jet sample.

Assuming that all the fake tags have a decay-length distribution symmetric around zero, one can predict the fake tags by examining the $-L_{xy}$ tag rate in the W + jets samples. The calculations then use parameterization functions derived separately from run 1A and 1B data. The reliability of the parameterization has been checked using different jet-trigger samples described in reference [51]. However, to exclude contributions in the negative tags from heavy flavor content in the generic jet sample which will be computed in the following sections, studies [50] show correction factors of 0.88, 0.87 and 0.83 are needed for the parameterization in the W + 1, 2, and $\geq$ 3 jets bins. Table 6.1 shows the predictions for the mistag backgrounds in the W + jets sample. Adding all uncertainties leads to a total error of $\pm 40\%$ on the fake background prediction in the W + jets sample [50].

71

Jet Multiplicity	$W + 1$ jet	$W + 2$ Jets	$W + \geq 3$ Jets
1A Parameterization	4.8	1.8	0.59
1B Parameterization	16.8	5.8	2.12
Correction Factor	0.88	0.87	0.83
Mistag Background	19.0 ± 7.6	6.6 ± 2.6	2.25 ± 0.89

Table 6.1: Mistag background estimated in the W + jets sample.

6.2 Non-W, Z Backgrounds

Tags from non-W, Z sources can mimic the semi-leptonic W boson decays. These include QCD light quark or gluon multi-jet events and heavy flavor pair production ($b\bar{b}$ or $c\bar{c}$). The event selection is satisfied by either a faked lepton from fragments of a jet, or a real lepton from b or c decays while other jets in the event are mis-measured and result a large missing energy. It is expected there are more tracks close to such fake or real leptons due to their proximity to the parent jet in both cases. By studying the lepton isolation (I_{cal}) and the missing transverse energy ($\not{E}_T$) in the events, tags from the non-W, Z sources can be directly determined from the data with the assumption that these two quantities are not correlated for the non-W, Z background events.

The I_{cal} vs. $\not{E}_T$ distributions for the run 1B W + jets samples are shown in figure 6.2. A cluster of events at large I_{cal} and small $\not{E}_T$ are dominated by leptons from b decays, while another cluster of events at small I_{cal} and large $\not{E}_T$ constitutes the W samples. Each plot is divided into four regions:

- Region A: $\not{E}_T < 15\ GeV$ and $I_{cal} < 0.1$

- Region B: $\not{E}_T < 15\ GeV$ and $I_{cal} > 0.2$

- Region C: $\not{E}_T > 20\ GeV$ and $I_{cal} > 0.2$

- Region D: $\not{E}_T > 20\ GeV$ and $I_{cal} < 0.1$ (W signal region)
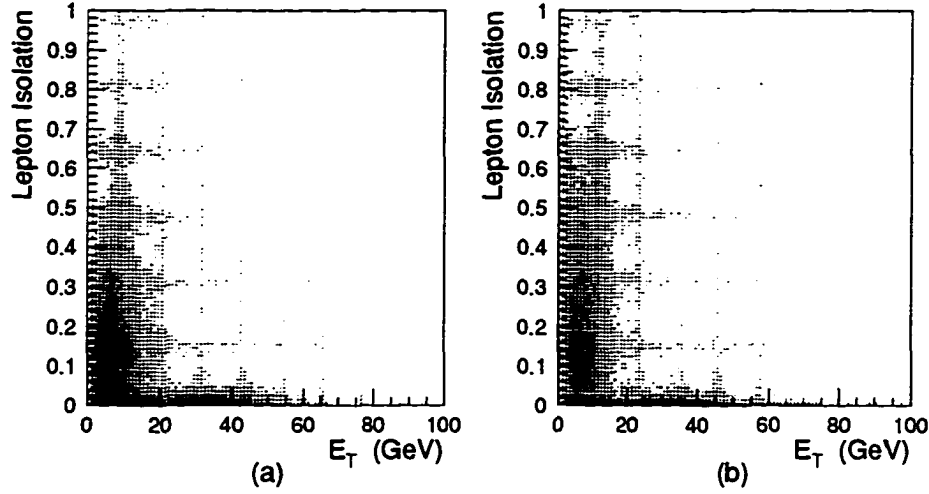
Figure 6.2: Lepton isolation *vs.* event $\not{E}_T$ in the (a) e + jets and (b) μ + jets sample.

The I_{cal} *vs.* $\not{E}_T$ method factorizes the computation in two steps: (1) the total number of non-W, Z events before tagging and (2) the tag rate in these events. The number of background events before tagging in the W signal region D can be estimated by $(A*C)/B$, and the fraction of such events in the W + jets sample is $F_{non-W,Z} = \frac{(A*C)/B}{D}$. Table 6.2 summaries the yields of events before tagging in run 1B data. The derived fractions $F_{non-W,Z}$ are also given for each jet multiplicity bin. Note that in order to improve the sample statistics, the trigger requirement is dropped since triggers do not introduce any bias. To estimate the tag rate for the background events in region D, the assumption that the tag rate of these events is independent of $\not{E}_T$ is verified in a $b\bar{b}$ Monte Carlo sample. Therefore, the tag rate in region D is assumed to be the same as that in region A where events are selected using the same isolation cut. Table 6.3 shows the tag rate per taggable jet found in each region. Number of expected tags from non-W, Z sources are listed in table 6.4. A systematic error of ±50% is assigned to include various uncertainties in the estimation.

73

Region	W + 1 jet		W + 2 Jets		W + $\geq$3 Jets	
	(e)	(μ)	(e)	(μ)	(e)	(μ)
A	7311	4129	610	362	63	52
B	10796	7842	1315	4796	195	950
C	627	548	145	567	38	212
D	5166	3974	745	664	139	138
$F_{non-W,Z}$(%)	8.2±0.4	7.3±0.4	9.0±1.0	6.4±1.0	8.8±2.4	8.4±2.4
Weighed(%)	7.8±0.3		7.8±0.7		8.6±1.7	

Table 6.2: Summary of events before tagging in regions A-D and the background fraction $F_{non-W,Z}$ in the run 1B inclusive W + jets sample.

Region	W + 1 jet		W + 2 Jets		W + $\geq$3 Jets	
	Tag Rate(%)		Tag Rate(%)		Tag Rate(%)	
	(e)	(μ)	(e)	(μ)	(e)	(μ)
A	2.9±0.3	2.6±0.4	1.7±0.6	1.7±0.7	6.0±2.6	1.4±1.4
B	5.7±0.3	9.1±0.5	5.4±0.7	13.8±0.5	6.1±1.4	11.5±0.8
C	5.1±1.3	12.2±2.0	7.8±2.4	11.8±1.3	10.7±4.1	8.7±1.5

Table 6.3: Summary of tag rate in regions A-C in the run 1B inclusive W + jets sample.

	W + 1 jet		W + 2 Jets		W + $\geq$3 Jets	
	(e)	(μ)	(e)	(μ)	(e)	(μ)
1B $N_{taggable}$	2203	1857	665	622	200	238
1B Non-W, Z	8.8±4.4		2.1±1.1		0.74±0.37	
1A+1B Non-W, Z	10.1±5.1		3.1±1.6		1.07±0.54	

Table 6.4: Summary of taggable jets in run 1B W + jets samples and estimated background from non-W, Z sources for run 1A + 1B data.

74

6.3 The Background from WW, WZ and $Z \to \tau\tau$

Contribution from the WW, WZ and $Z \to \tau\tau$ processes are estimated in the Monte Carlo samples. The calculations use the theoretical production cross section and their branching ratios in "lepton plus jets" modes. By combining the acceptances including tag rates predicted by the simulations, the final results are obtained after multiplication by the integrated luminosity for the run. Relative 30% errors are applied to the Monte Carlo predictions to include various uncertainties in the estimation.

WW events can be identified as W + jets events with one W decay leptonically. The theoretical production cross section of the process is $9.5 \pm 0.5 \pm 0.5$ pb [52] where the first error is due to the uncertainty in structure functions and the second is from Q^2 uncertainties. Table 6.5 gives the acceptance and tag rate studied using 157,366 events generated with PYTHIA and detector simulations. Tags from the WW process are estimated by

$$N_{WW} = \sigma(WW) \cdot \epsilon_{accpt} \cdot \epsilon_{tag} \cdot \int \mathcal{L}\, dt$$

Jet Multiplicity	W + 1 Jet	W + 2 Jets	W + $\geq$3 Jets
Acceptance	$(5.00\pm0.05)\%$	$(4.71\pm0.05)\%$	$(0.85\pm0.02)\%$
Tag Rate	$(1.19\pm0.12)\%$	$(2.35\pm0.18)\%$	$(2.91\pm0.46)\%$
1B Background	0.51 ± 0.17	0.95 ± 0.29	0.21 ± 0.07
1A + 1B Background	0.58 ± 0.20	1.05 ± 0.32	0.24 ± 0.09

Table 6.5: WW background estimated in the W + jets sample.

WZ diboson production is expected to give a small contribution to the tags in the W + jets sample with events containing $W \to e\nu$ or $\mu\nu$ and $Z \to b\bar{b}$ decays. The process is simulated with 27,124 Monte Carlo events. The following calculation is done to examine the WZ background:

$$N_{WZ} = \sigma(WZ) \cdot Br \cdot \epsilon_{accpt} \cdot \epsilon_{tag} \cdot \int \mathcal{L}\, dt$$

75

By counting events passing the W + jets selection and requiring events with at least one jet tagged, the contributions from the WZ process can be estimated from the production cross section $\sigma(WZ)$ of 2.6 $\pm$ 0.3 $\pm$ 0.3 pb and the branching ratio for $WZ \to e\nu b\bar{b}$ or $\mu\nu b\bar{b}$ predicted to be 0.02 [53]. Table 6.6 summaries the calculations.

Jet Multiplicity	W + 1 Jet	W + 2 Jets	W + ≥ 3 Jets
Acceptance	(11.9$\pm$0.2)%	(12.8$\pm$0.2)%	(2.4$\pm$0.1)%
Tag Rate	(18.4$\pm$0.7)%	(33.0$\pm$0.8)%	(33.4$\pm$1.9)%
1B Background	0.21$\pm$0.07	0.40$\pm$0.13	0.08$\pm$ 0.03
1A + 1B Background	0.23$\pm$0.08	0.45$\pm$0.15	0.09$\pm$0.03

Table 6.6: WZ background estimated in the W + jets sample.

The production cross section for the $\sigma(Z \to \tau\tau)$ process is 0.2 $\pm$ 0.02 nb. The subsequent τ decays can provide high P_T electrons or muons along with hadrons. Simulations with 317,202 events, table 6.7 gives a background estimate of

$$N_{Z \to \tau\tau} = \sigma(Z \to \tau\tau) \cdot \epsilon_{accpt} \cdot \epsilon_{tag} \cdot \int \mathcal{L} \, dt$$

Jet Multiplicity	W + 1 Jet	W + 2 Jets	W + ≥ 3 Jets
Acceptance	(0.176$\pm$0.007)%	(0.034$\pm$0.003)%	(0.003$\pm$0.001)%
Tag Rate	(1.32$\pm$0.44)%	(1.32$\pm$0.44)%	(1.32$\pm$0.44)%
1B Background	0.42$\pm$0.13	0.08$\pm$0.03	0.007$\pm$0.002
1A + 1B Background	0.49$\pm$0.16	0.10$\pm$0.04	0.009$\pm$0.003

Table 6.7: $Z \to \tau\tau$ background estimated in the W + jets sample.

6.4 The $Wb\bar{b}$ and $Wc\bar{c}$ Backgrounds

The leading order and some higher order Feynman diagrams for $Wb\bar{b}$ and $Wc\bar{c}$ production are shown in figure 6.3. These processes are simulated using several Monte

76
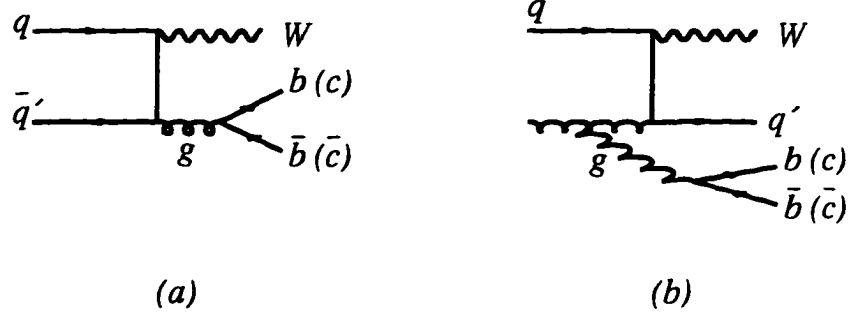
Figure 6.3: Feynman diagrams for (a) $Wb\bar{b}$ ($Wc\bar{c}$) production and (b) an example of higher order production.

Carlo programs to obtain an accurate production rate of event with only one "real" W with gluons splitting into jets. These programs consider effects of higher order contributions, finite b (c) mass as well as the angular correlations of the two bottom (charm) quarks in space. The computation thus combines the fraction of W events that are expected to have a heavy flavor pair and the corresponding tagging efficiencies, to estimate the expected tags per event in each jet multiplicity bin. The final contributions can be obtained by multiplying the number of "real" W candidates in the sample.

6.4.1 Composition of the W + Jets Sample

To estimate the number of the "real" W + jets events, one can subtract the Non-W, Z fraction, WW, WZ, $Z \to \tau\tau$ (described in previous sections) and Z + jets events from the inclusive W + jets sample. Note that there still remain Z + jets events in the W + jets sample after the Z removal described in chapter 3. The ratios between Z and W events (N_Z/N_W) estimated from Monte Carlo are $(4.9 \pm 2.5)\%$ in the electron sample and $(10.5 \pm 1.9)\%$ in the muon sample [54]. Therefore the number of "real" W + jets events (N_W) can be estimated by

$$N_W = \frac{N_{data} \cdot (1 - F_{non-W,Z}) - N_{WW} - N_{WZ} - N_{Z \to \tau\tau}}{1 + \frac{N_Z}{N_W}}$$

77

	$W + 1$ jet	$W + 2$ Jets	$W + \geq 3$
N_{data}	9003	1382	273
Z/W ratio (weighed)	$(7.3\pm2.2)\%$	$(7.5\pm2.2)\%$	$(7.7\pm2.5)\%$
$F_{non-W,Z}$	$(7.8\pm0.3)\%$	$(7.8\pm0.7)\%$	$(8.6\pm1.7)\%$
WW event	43 ± 13	40 ± 12	7.3 ± 2.2
WZ event	1 ± 0	1 ± 0	0.2 ± 0.1
$Z \to \tau\tau$ event	32 ± 10	6 ± 2	0.5 ± 0.16
"real" W event	7665 ± 235	1142 ± 52	224 ± 14
"real" Z event	560 ± 168	86 ± 25	17 ± 6

Table 6.8: Composition of the run 1B inclusive W + jets sample.

Table 6.8 list each component in the calculations and the final results. These numbers are used to estimate the $W b\bar{b}$, $W c\bar{c}$ and $W c$ backgrounds as well as the Z + heavy flavor contributions in the following sections.

6.4.2 $W b\bar{b}$ background

The Monte Carlo generators used to model the $W b\bar{b}$ production include a parton shower program and the VECBOS [55] program which are both interfaced to the Herwig generator. The parton shower program runs the W + 1 jet matrix element calculations, followed by parton shower evolution that produces $b\bar{b}$ pairs. The program is used to predict the fraction of W events with exactly one b jet in the final state. It has been shown that the parton shower approach underestimates the rate of events in the region where the angular separation of the two b jets becomes larger. Therefore, the fraction of events with exactly two b jets in the final state is calculated using the VECBOS program with a $b\bar{b}$ option. VECBOS is a parton-level Monte Carlo based on tree-level matrix element computation. It generates two hard b quarks, giving rise to two separate b jets in each event. Therefore the $W b\bar{b}$ background in the W + jets sample can be calculated in each of the jet multiplicity bins by

$$N_{W b\bar{b}} = N_W \cdot (F1_{W b\bar{b}} \cdot \epsilon1_{W b\bar{b}} + F2_{W b\bar{b}} \cdot \epsilon2_{W b\bar{b}})$$

78

Jet Multiplicity	$W + 1$ Jet	$W + 2$ Jets	$W + \geq 3$ Jets
N_W	7665±235	1142±52	224±14
$F1_{W b \bar{b}}$	(0.55±0.14)%	(0.87±0.23)%	(1.53±0.48)%
$F2_{W b \bar{b}}$		(0.85±0.25)%	(1.50±0.40)%
$\epsilon 1_{W b \bar{b}}$	(20.6±0.6)%	(20.0±1.2)%	(15.3±2.6)%
$\epsilon 2_{W b \bar{b}}$		(39.5±2.8)%	(38.1±4.9)%
1B Background	8.7±2.2	5.8±1.7	1.80±0.58
1A + 1B Background	10.7±3.8	6.8±2.5	2.10±0.84

Table 6.9: $W b \bar{b}$ background estimated in the $W +$ jets sample.

where N_W is the number of "real" W candidates; $F1_{W b \bar{b}}$ and $F2_{W b \bar{b}}$ are the fractions of events which have exactly one and two b jets in the final state [56]; the $\epsilon_{W b \bar{b}}$'s are the corresponding tagging efficiencies. Table 6.9 summarizes the results.

6.4.3 $W c \bar{c}$ background

The $W c \bar{c}$ background is calculated using the same method as used in the $W b \bar{b}$ computation. All events containing $W c \bar{s}$ vertex are exclude and are considered as part of the $W c$ background described in the next section. Therefore the difference between the contributions from $W b \bar{b}$ and that of $W c \bar{c}$ are due to the quark mass and fragmentation differences. Tables 6.10 summarizes the results.

6.5   The $W c$ Background

An example of associated production of charm with a W boson at lowest order is shown in figure 6.4. The fusion of a strange quark from the sea with a gluon, $gs \rightarrow W c$ is the dominated source with a smaller contribution from the $gd \rightarrow W c$ process. Higher order processes such as $gg \rightarrow W c \bar{s}$ which have no quark in the initial state are also possible. The background shown in table 6.11 is calculated in each jet multiplicity by

$$N_{Wc} = N_W \cdot F_{Wc} \cdot \epsilon_{Wc}$$

79

Jet Multiplicity	W + 1 Jet	W + 2 Jets	W + $\geq$3 Jets
N_W	7665±235	1142±52	224±14
$F1_{Wc\bar{c}}$	(1.28±0.49)%	(2.37±0.91)%	(3.49±1.45)%
$F2_{Wc\bar{c}}$		(1.04±0.27)%	(1.80±0.50)%
$\epsilon1_{Wc\bar{c}}$	(4.8±0.2)%	(4.0±0.4)%	(4.8±1.0)%
$\epsilon2_{Wc\bar{c}}$		(7.0±1.4)%	(12.2±3.0)%
1B Background	4.7±1.8	1.9±0.7	0.87±0.36
1A + 1B Background	5.7±2.6	2.5±1.2	1.01±0.48

Table 6.10: $Wc\bar{c}$ background estimated in the W + jets sample.
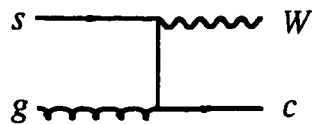
Figure 6.4: An example of the Feynman diagram for Wc production.

80

Jet Multiplicity	W + 1 Jet	W + 2 Jets	W + $\geq$3 Jets
N_W	7665±235	1142±52	224±14
F_{Wc}	(5.3±1.3)%	(7.5±1.5)%	(8.0±1.5)%
ϵ_{Wc}	(3.5±0.3)%	(5.3±0.7)%	(9.6±1.9)%
1B Background	14.2±3.7	4.5±1.1	1.72±0.48
1A + 1B Background	17.4±4.7	5.4±1.4	1.96±0.59

Table 6.11: Wc background estimated in the W + jets sample.

where N_W is the number of "real" W candidates; F_{Wc} is the fraction of Wc events found in W + jets events studied in the Monte Carlo sample [49]; ϵ_{Wc} is the event tag rate.

6.6 Z + Heavy Flavor

Events containing Z + heavy flavor jets are accepted into the W + jets sample. The heavy flavor hadrons come from gluon splitting which are similar to $Wb\bar{b}$ and $Wc\bar{c}$, or from $Zb\bar{b}$ vertex ($gg \to Zb\bar{b}$) as well as $Zc\bar{c}$ vertex (similar to $Wc\bar{s}$). These contributions are estimated by multiplying the fraction of each process obtained from Monte Carlo simulations of the number of Z events remaining in the W sample as shown in table 6.8. Studies [50] show that the Z + heavy flavor events provide 2.7 ± 1.2 tags in the W + 1 jet sample, 1.4 ± 0.5 tags in the W + 2 jets sample, and 0.44 ± 0.18 tags in the W + $\geq$ 3 jets sample.

6.7 Single Top Production

Single top production in the $p\bar{p}$ collisions is an additional background to the $t\bar{t}$ signal in the W + jets sample. This includes the top quark produced from W-gluon fusion and from W^* decays. The theoretical production cross section [57] for these two channels are 1.44 ± 0.43 pb for W-gluon fusion and 0.74 ± 0.05 pb for W^* modes. The processes are simulated in Monte Carlo samples. 80,146 W-gluon events and 72,103 W^* events are used

81

Jet Multiplicity	$W + 1$ Jet	$W + 2$ Jets	$W + \geq 3$ Jets
Acceptance			
$W - g$	$(2.65\pm0.06)\%$	$(3.78\pm0.07)\%$	$(2.02\pm0.05)\%$
W^*	$(2.08\pm0.05)\%$	$(4.21\pm0.07)\%$	$(1.51\pm0.05)\%$
Tag Rate			
$W - g$	$(20.1\pm0.9)\%$	$(26.4\pm0.8)\%$	$(32.0\pm1.2)\%$
W^*	$(23.1\pm1.1)\%$	$(36.6\pm0.9)\%$	$(40.0\pm1.5)\%$
1B Background	1.01 ± 0.3	2.32 ± 0.70	1.24 ± 0.37
1A + 1B Background	1.20 ± 0.36	2.73 ± 0.82	1.51 ± 0.45

Table 6.12: Single top production estimated in the $W +$ jets sample.

to obtain the acceptance and tag rate. Table 6.12 summaries the final numbers with relative 30% uncertainties assigned.

6.8 Background Correction for $t\bar{t}$ Content

The sum of all the backgrounds assuming that there are no $t\bar{t}$ events in the $W +$ jets samples are shown in table 6.13. Figure 6.5 shows the number of W candidates, the number of events passing the tagging algorithm, and the backgrounds as a function of jet multiplicity in the event. A clear excess is shown in $W + \geq 3$ jets bin where most $t\bar{t}$ events are expected to lie.

However, corrections are needed for those backgrounds which are obtained by multiplying the number of $W +$ jets events. The contributions are overestimated because the number of $W +$ jets events should be smaller since some of them are real $t\bar{t}$ events. This is done using a iterative procedure which assumes a fixed fraction of backgrounds from non-$t\bar{t}$ $W +$ jets events. Other backgrounds such as WW, WZ, $Z \rightarrow \tau\tau$ and single top contributions are directly calculated from theoretical production cross section and thus remain the same during the iteration. With data tagged events being the sum of the tagged $t\bar{t}$ events and backgrounds (the $t\bar{t}$ event tagging efficiency was given in the previous chapter), the run 1A and 1B backgrounds after correction for the $t\bar{t}$ content are 1.66 ± 0.47 and $7.36 \pm$

82

Jet Multiplicity	$W + 1$ Jet	$W + 2$ Jets	$W + \geq 3$ Jets
Mistags	19.0±7.6	6.6±2.6	2.25±0.89
$Wb\bar{b}$, $Wc\bar{c}$	16.4±6.4	9.3±3.7	3.11±1.32
Wc	17.4±4.7	5.4±1.4	1.96±0.59
Z + heavy flavor	2.7±1.2	1.4±0.5	0.44±0.18
WW, WZ, $Z \to \tau\tau$	1.3±0.4	1.6±0.5	0.34±0.12
Non-W, Z	10.1±5.1	3.1±1.6	1.07±0.54
single top	1.20±0.36	2.73±0.82	1.51±0.45
Total	68.1±12.2	30.1±5.1	10.68±1.85

Table 6.13: Summary of backgrounds in the W + jets sample.

1.37 respectively. These numbers are separately used in the calculation of the $t\bar{t}$ production cross section in the next chapter.

6.9 Kinematic Distributions

Kinematic distributions of the tagged events in the $W + \geq 3$ jets sample are compared to those in $t\bar{t}$ Monte Carlo events ($M_{top} = 175$ GeV/c^2) and backgrounds. The backgrounds have been corrected for the $t\bar{t}$ content, and the shapes include relative contributions from $Wb\bar{b}$, $Wc\bar{c}$, Wc and single top contributions. Figures 6.6 and 6.7 compare the $c\tau$ and E_T distributions of the tagged jets. The $c\tau$ distributions show that the tagged jets are consistent with jets primarily from heavy flavor in both $t\bar{t}$ and background events. The E_T plot shows that the tagged jets in the $t\bar{t}$ events are more energetic than those in the backgrounds and data is consistent with the predictions. In figure 6.8, number of tracks attached to the displaced vertex in the tagged jets is compared. The fact that there are relative more charm tags and less bottom tags among the backgrounds results in fewer tracks associated with the background tags as shown. Reconstructed transverse mass of the W bosons is shown in figures 6.9. It is found that the selection of a high P_T lepton with E_T requirement in the events gives a clear W identification as expected. Figure 6.10 compares the total transverse energy distribution, H_T, of the tagged events. H_T is defined as the sum of the transverse

83

energy of the primary lepton and all jets in the event as well as the $\not{E}_T$. The plot shows that the $t\bar{t}$ events are more energetic and that events with at least one tagged jet have relatively more total transverse energy than untagged events. The H_T distributions also give indication that an additional H_T cut could have been used to reject the background in the W + jets sample as used in the analysis published by the D0 collaboration [66]. However, to avoid distorting the $t\bar{t}$ event topology, this dissertation does not use the kinematic H_T cut in the event selection. In all cases the kinematic distributions are consistent between data and predictions.

84
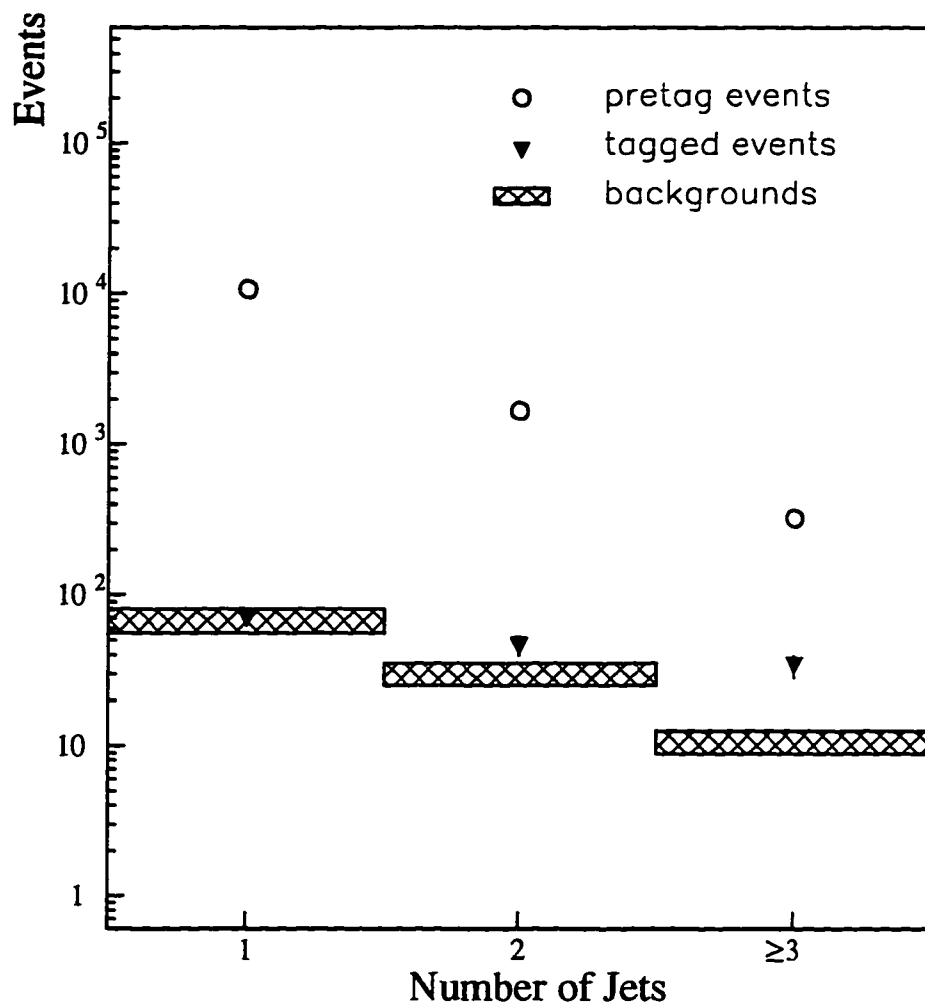
Figure 6.5: The W + jets distribution observed in the data. The open circles are events before tagging and the solid triangles are events after tagging. The cross-hatched boxes are backgrounds assumed there is no $t\bar{t}$ events in the samples.

85
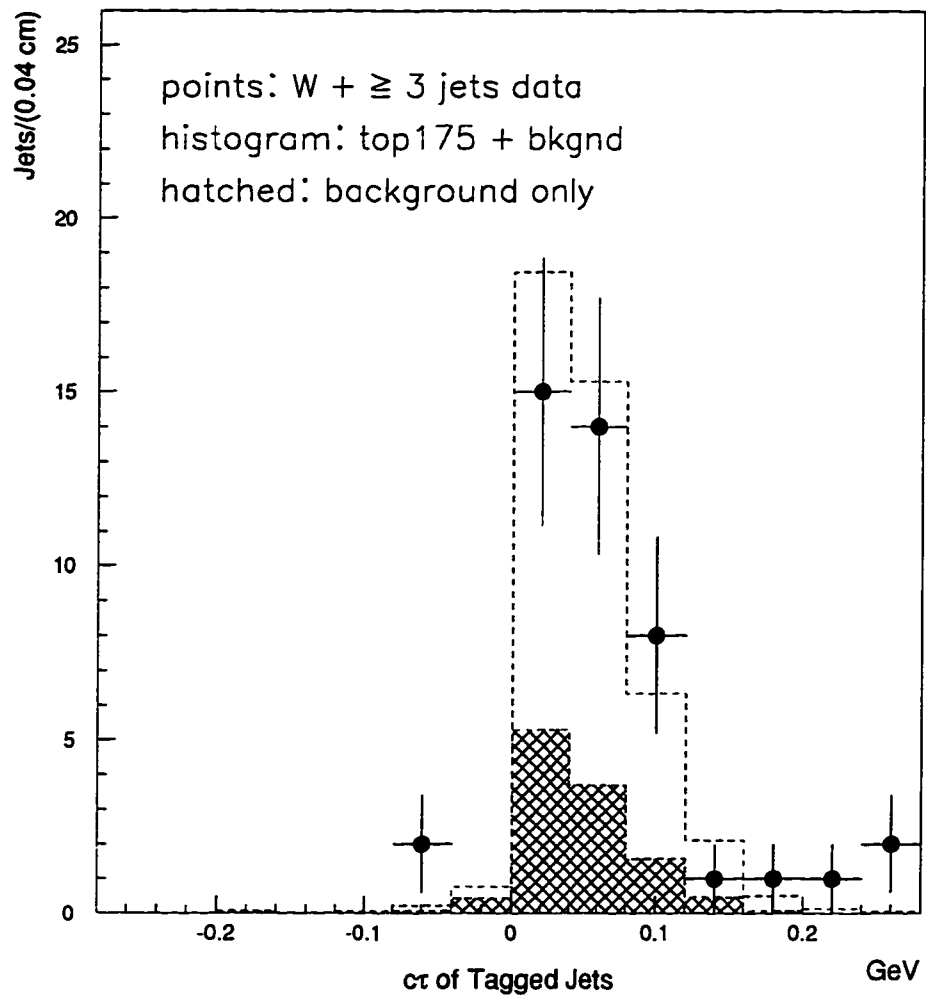
Figure 6.6: The dash histogram is the $c\tau$ of the tagged jets in the top signal region for a Herwig top175 + background Monte Carlo. The points are the data. The two distributions are normalized to the same area. The hatched histogram is the background shape normalized to its relative contribution.

86
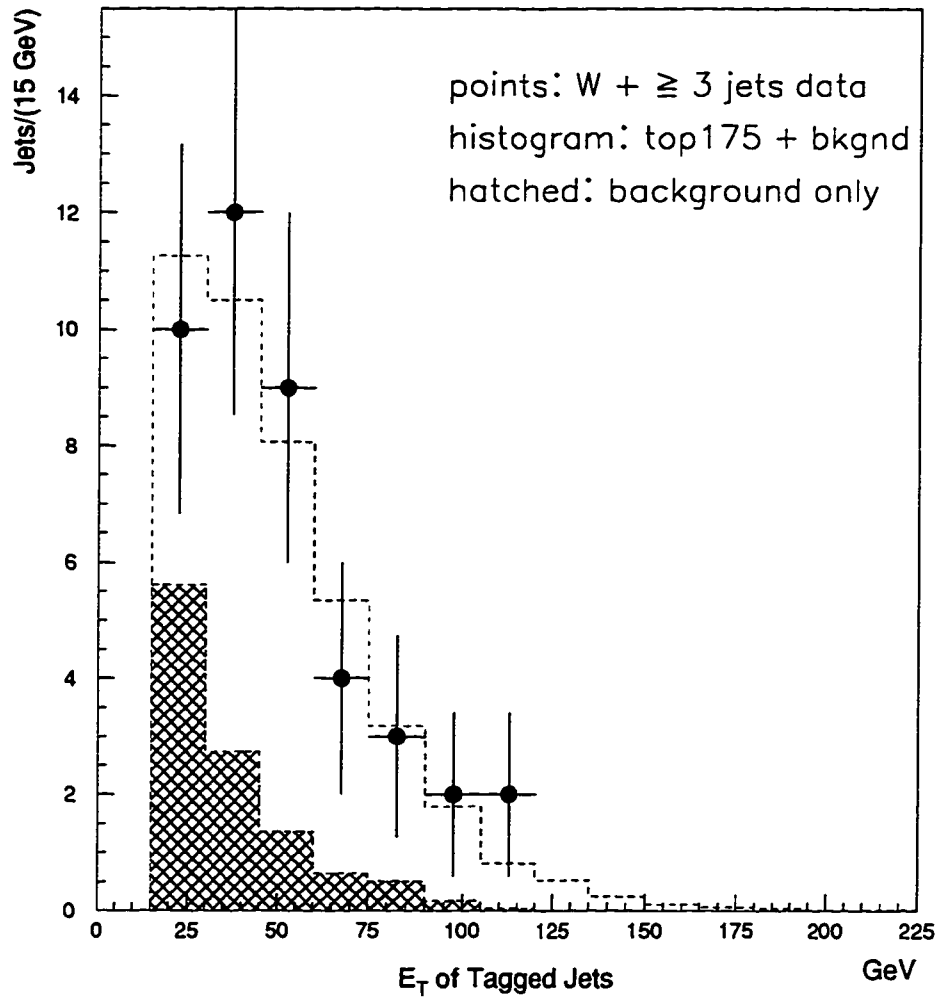
Figure 6.7: The dash histogram is the E_T of the tagged jets in the top signal region for a Herwig top175 + background Monte Carlo. The points are the data. The two distributions are normalized to the same area. The hatched histogram is the background shape normalized to its relative contribution.

87
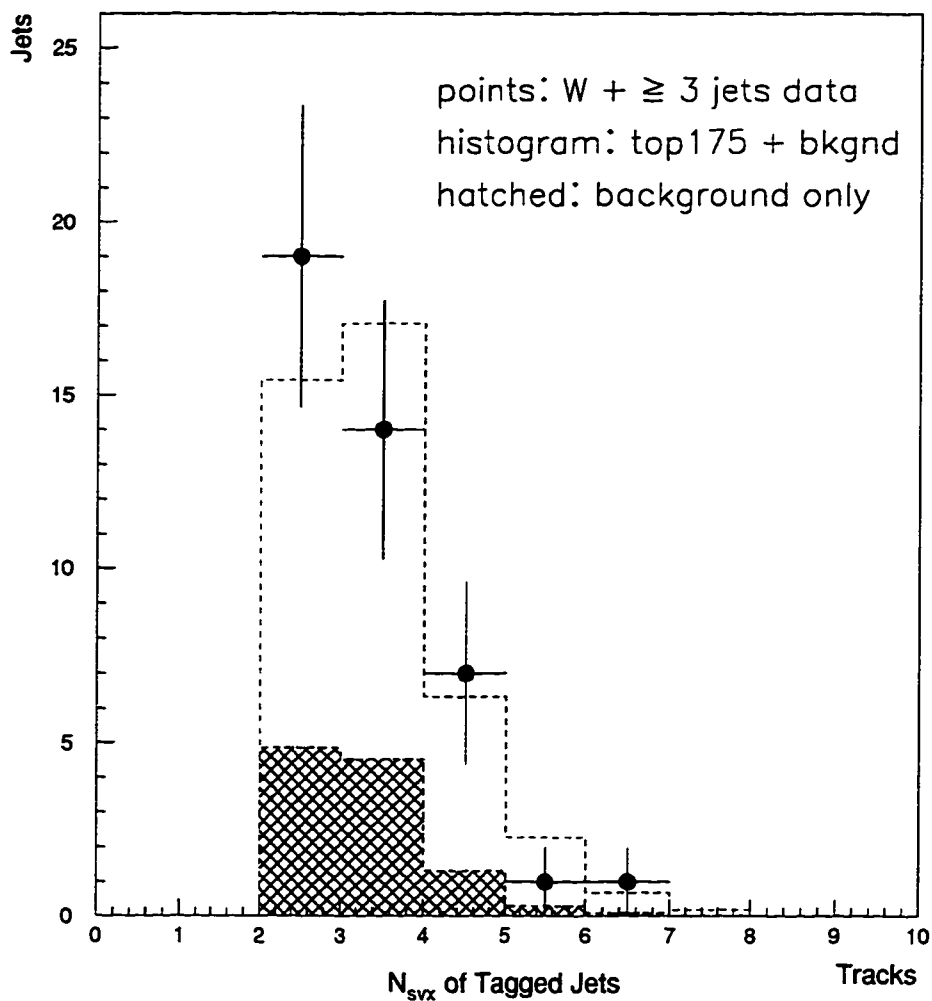
Figure 6.8: The dash histogram is the number of tracks attached to the vertex for the tagged jets in the top signal region for a Herwig top175 + background Monte Carlo. The points are the data. The two distributions are normalized to the same area. The hatched histogram is the background shape normalized to its relative contribution.

88
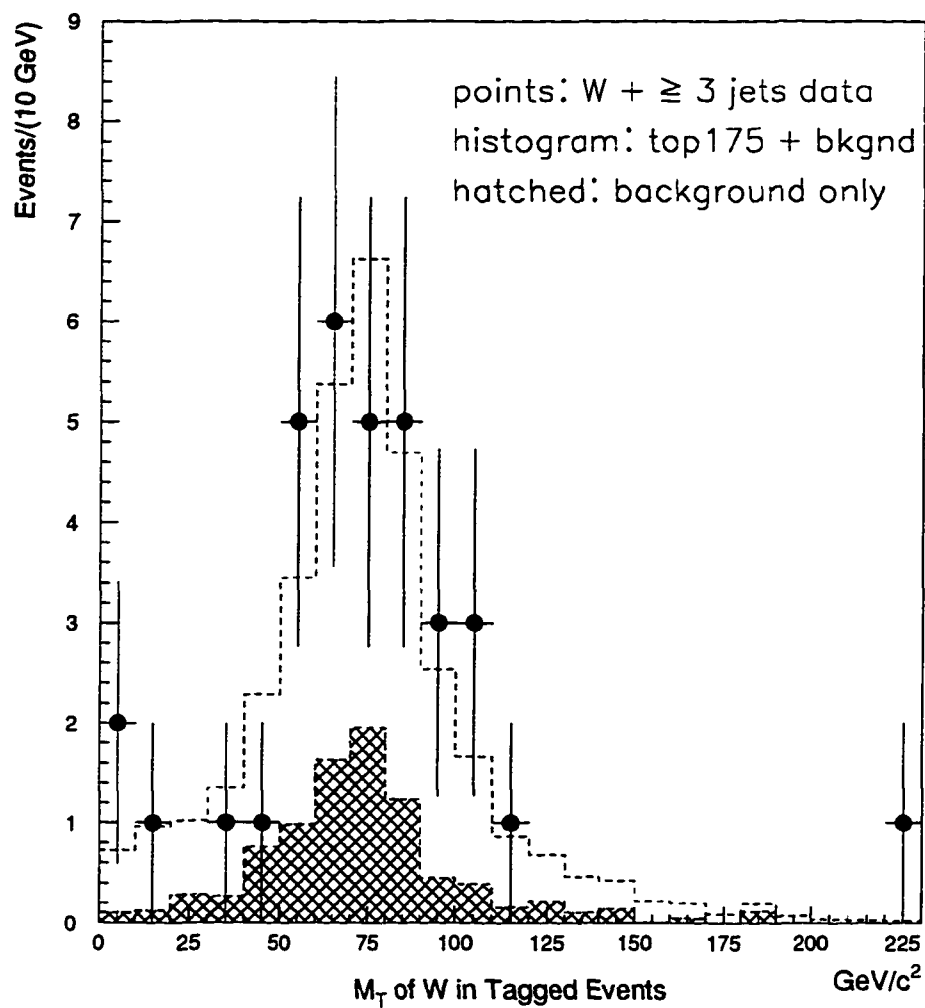
Figure 6.9: The dash histogram is the transverse mass distribution of the lepton and neutrino (whose momentum is estimated using the missing E_T vector) for a Herwig top175 + background Monte Carlo. The points are the data. The two distributions are normalized to the same number of events. The hatched histogram is the background shape normalized to its relative contribution.

89
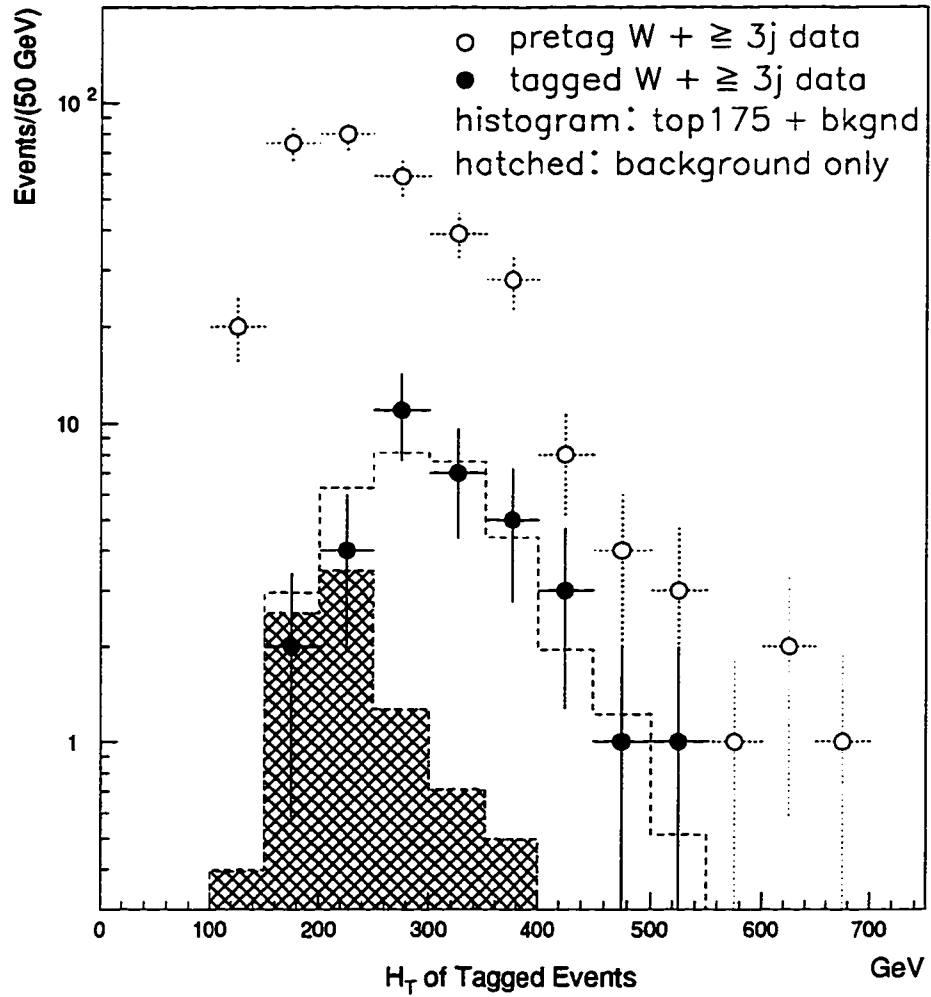
Figure 6.10: The dash histogram is the H_T distribution for a Herwig top175 + background Monte Carlo. The points are the data. The two distributions are normalized to the same number of events. The hatched histogram is the background shape normalized to its relative contribution.

90

Chapter 7

Results and Conclusions

The $t\bar{t}$ production cross section calculated using the tagged events in the "lepton plus jets" channel is presented. Given the event counts, backgrounds, acceptances, and integrated luminosity developed in the preceeding chapters, a maximum-likelihood method assembles all the numbers, and determines the cross section and its uncertainty. The central value of the cross section found from the maximum of the likelihood method is

$$\sigma = \frac{N - B}{\epsilon \cdot \int \mathcal{L} dt}$$

as shown in the chapter 1. A summary of all results is listed in table 7.1.

7.1 Measurement of the Cross Section

The cross section $(\sigma_{t\bar{t}})$ and its uncertainty are calculated using the likelihood function:

$$L = \frac{(\epsilon \cdot \sigma_{t\bar{t}} \cdot \int \mathcal{L} dt + B)^N}{N!} e^{(\epsilon \cdot \sigma_{t\bar{t}} \cdot \int \mathcal{L} dt + B)^N} \cdot e^{-\frac{(B-\bar{B})^2}{2\sigma_B^2}} \cdot e^{-\frac{(\epsilon-\bar{\epsilon})^2}{2\sigma_\epsilon^2}} \cdot e^{-\frac{(\int \mathcal{L} dt - \int \bar{\mathcal{L}} dt)^2}{2\sigma_{lum}^2}}$$

Note the likelihood expression is a combination of a Poisson for the number of tagged events and Gaussians for backgrounds, acceptances and integrated luminosity. In the maximization the parameters B, ϵ and $\int \mathcal{L} dt$ are initialized at their mean values, $\bar{B}$, $\bar{\epsilon}$ and $\int \bar{\mathcal{L}} dt$, and varied to obtain a maximum value for the likelihood. $\sigma_{t\bar{t}}$ is determined at the maximum of the $\ln L$, the minium value of $-\ln L$ in the calculations.

91

Item	Run 1A	Run 1B	Combined 1A + 1B
Tagged Events	4	30	34
Corrected Background	1.7 ± 0.5	7.4 ± 1.4	9.0 ± 1.9
Acceptance	0.030 ± 0.010	0.040 ± 0.007	0.038 ± 0.007
Luminosity (in pb^{-1})	19.3 ± 0.8	90.1 ± 7.2	109.4 ± 7.2
Cross Section (in pb) ($M_{top} = 175$ GeV/c^2)	$4.0^{+5.4}_{-3.4}$	$6.3^{+2.4}_{-1.9}$	$6.0^{+2.2}_{-1.8}$

Table 7.1: Summary of the $t\bar{t}$ production cross section measurement.

To determine the uncertainty, several adjustment need to be applied on the likelihood function. These include

- The run 1A and run 1B numbers for each parameter are separately used in the Gaussians.

- The acceptances are divided into $\epsilon = A_{t\bar{t}} * \epsilon_{trigger} * \epsilon_{tag}$ as described in chapter 5 where the first two items are common to run 1A and 1B.

- The backgrounds are separated into mistags and non-mistags. The non-mistags background can be scaled by the tagging efficiency to obtain the pre-tag background, i.e. $B = B^{mistag} + \epsilon_{tag} * B^{pretag}$. The purpose is to include the tagging efficiency uncertainty in the pretag backgrounds used in the likelihood calculations.

Using $G(p, \bar{p}, \sigma_p)$ as a Gaussian expression for parameter p with mean $\bar{p}$ and width σ_p, and $P(n, m)$ as a Poisson with mean m and number of observed events n, the likelihood expression changes to:

$$
\begin{aligned}
L = \ & G(B^{pretag}, \bar{B}^{pretag}, \sigma_{B^{pretag}}) \cdot G(B^{mistag}, \bar{B}^{mistag}, \sigma_{B^{mistag}}) \\
& \cdot G(A_{t\bar{t}}, \bar{A}_{t\bar{t}}, \sigma_{A_{t\bar{t}}}) \cdot G(\epsilon_{trigger}, \bar{\epsilon}_{trigger}, \sigma_{\epsilon_{trigger}}) \cdot G(\epsilon_{tag}, \bar{\epsilon}_{tag}, \sigma_{\epsilon_{tag}}) \\
& \cdot G(\int \mathcal{L}dt, \int \bar{\mathcal{L}}dt, \sigma_{lum}) \cdot P(N, \epsilon \cdot \int \mathcal{L}dt \cdot \sigma_{t\bar{t}} + B)
\end{aligned}
$$

92

The uncertainty is estimated by considering the $\sigma_{t\bar{t}}$ change necessary to decrease $\ln L$ by $\Delta(\ln L) = \frac{1}{2}$ which corresponds to an increase of the goodness-of-fit χ^2 by 1. With top mass measured to be 175.6 ± 5.7 (stat) ± 7.1 (syst) GeV/c^2 in CDF [67], the $t\bar{t}$ production cross section is measured to be

$$\sigma_{t\bar{t}} = 6.0^{+2.2}_{-1.8} \, pb \quad (M_{top} = 175 \, GeV/c^2)$$

while cross sections at top mass of 165 and 185 GeV/c^2 are measured to be $6.7^{+2.4}_{-1.9}$ and $5.9^{+2.1}_{-1.7}$ pb respectively.

7.2 Conclusions

We have presented a measurement of the $t\bar{t}$ cross section in the "lepton plus jets" channel in $\bar{p}p$ Collisions at $\sqrt{s} = 1.8 \, TeV$. Results are summarized in table 7.1. Breaking down the sources of error on the measurement, table 7.2 lists various uncertainties contributing to the final numbers. It is seen that a good measurement has been made in a small signal sample where the uncertainties are dominated by the statistical error.

In figure 7.1, the experimental results are compared to the theoretical predictions [17]. The cross section measured is in reasonable agreement with the theoretical value. At the top mass 175 GeV/c^2, cross section values measured from other $t\bar{t}$ decay channels in CDF are also compared and shown in figure 7.2. The data include the $t\bar{t}$ fully hadronic (HAD) final state ($t\bar{t} \rightarrow q\bar{q}'b \, q\bar{q}'\bar{b}$), di-lepton (DIL) final state ($t\bar{t} \rightarrow l\nu b \, l'\nu\bar{b}$, $l, l' = e$ or μ), and the "lepton plus jets" channel with different b-tagging technique (SLT) [3]. The spread in theoretical values predicted by references [15][16][17] is also shown. These numbers are consistent with each other within one standard deviation and show a good agreement within the framework of the Standard Model predictions. The measurement of the $t\bar{t}$ production cross section in the "lepton plus jets" channel described in this dissertation represents an important test of the Standard Model prediction for the $t\bar{t}$ production cross section in $\bar{p}p$ Collisions at $\sqrt{s} = 1.8 \, TeV$.

93
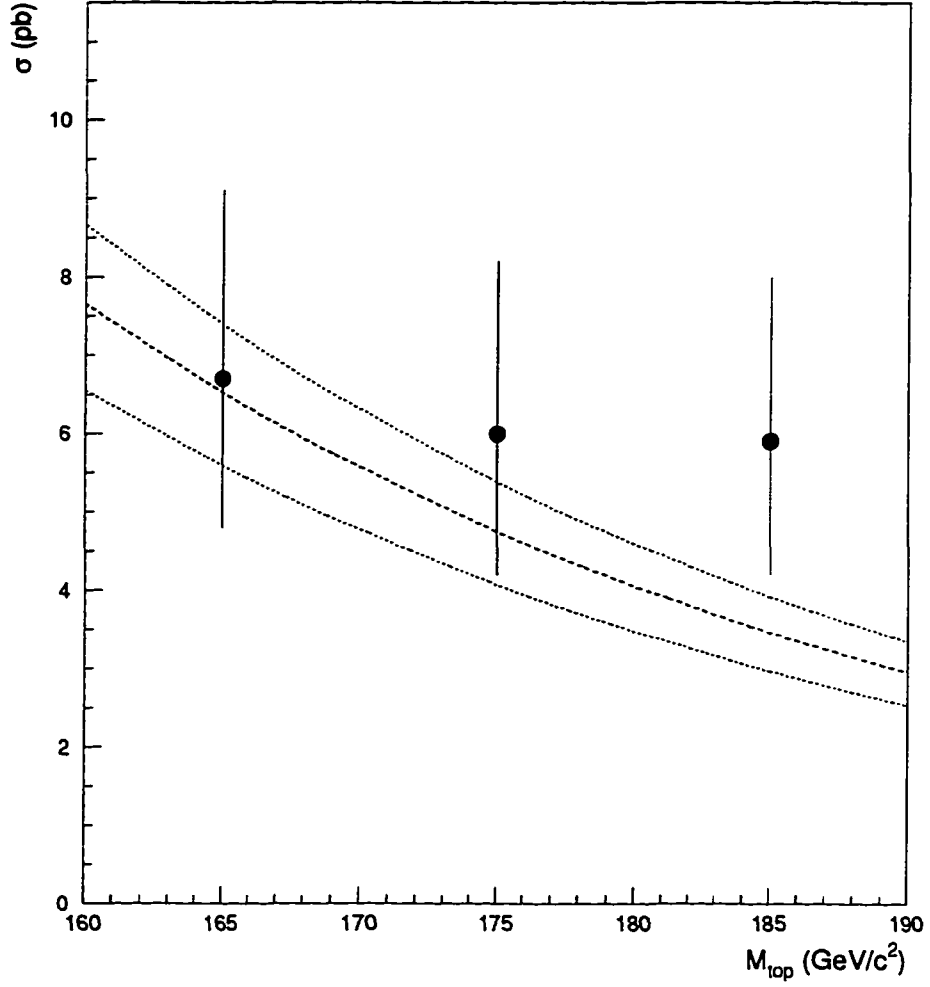
Figure 7.1: The $t\bar{t}$ production cross sections as a function of top mass. The dash line is the theoretical predictions with $\pm 1\sigma$ bounds shown in dot lines. The points are experimental values measured in this dissertation.

94
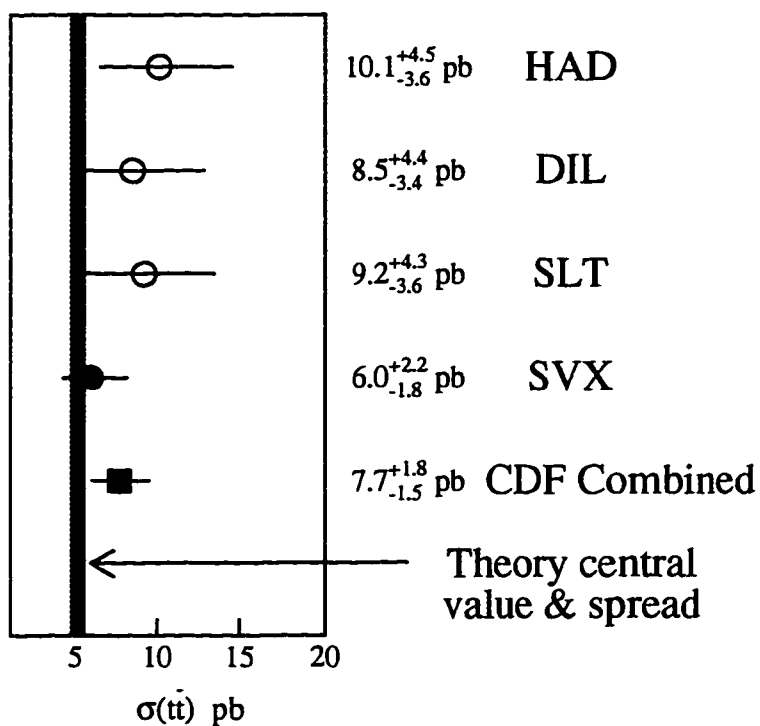
Figure 7.2: The $t\bar{t}$ production cross sections measured in different $t\bar{t}$ decay channels in CDF. The measurement described in the dissertation is referred as SVX channel. The shaded region is the spread theoretical central values assuming a top mass 175 GeV/c^2.

95

Source	Uncertainty
Statistics	23.3%
Background	13.0%
Integrated Luminosity	6.9%
Geometric Acceptance	8.5%
Trigger Efficiency	8.5%
Tagging Efficiency	12.2%
Total	32.4%

Table 7.2: Summary of uncertainties for the cross section measurement.

96

Appendices

97

Appendix A

Prospects for Future Work

The Fermilab Main Injector collider run is expected to begin in few years. It will provide a substantial luminosity upgrade of up to a few $\times$ 10^{32} $cm^{-2}sec^{-1}$ and 99 proton and antiproton bunches. The accompanying upgrades of CDF and D0 detectors will also lead to an extended high P_T physics which has been evaluated in reference [68].

The impact on the future measurement of the $t\bar{t}$ production cross section is multi-phasic. An increase of the acceptances results from the extension of the detector coverage for high P_T leptons as well as the improved tagging efficiency benefited from new silicon system for the identification of low P_T tracks and dense jets. The $W + \geq 3$ jets sample is expected to contain $\sim$ 1,300 events with $\sim$ 1,100 tags over the course of the $\sim$ 2 fb^{-1} data run. This could radically improve the statistical prospects. A potential to obtain the backgrounds directly from data would also reduce uncertainties resulting from the massive Monte Carlo simulations shown in this dissertation. Some techniques which exploit the kinematic features of the $t\bar{t}$ events may need to be developed to achieve the prospects.

However several systematic problems occurring at the large luminosities have to be addressed. The level of the isotropic energy flow, the so-called underlying events, not only jeopardize the accuracy of the event vertex finding but also affect the certainty of the isolation selection cut. Furthermore substantially increased instantaneous luminosity may be a challenge for the detector operations. More systematic uncertainties might occur and prohibit precision measurements.

98

In the far future, the LHC $p\bar{p}$ collider run will provide the $t\bar{t}$ production cross section measurement in a different kinematic and initial state regime. At the energies $\sqrt{s} \sim 13\ TeV$, most top quarks are expected to be produced from the gluon splitting process. Therefore a different $t\bar{t}$ production mechanism can be examined.

Appendix B

The Jet Probability Fit Algorithm and Applications

B.1 The Jet Probability Algorithm

The jet probability algorithm has been documented in reference [3]. Here is a brief description of the algorithm. As described in chapter 4, the signed impact parameters of decay fragments from hadrons with a lifetime preferentially populate in the positive side of the distribution. Without the lifetime effects, the impact parameters should have been only determined by the resolutions of the silicon vertex detector and equally distributed in both sides. Therefore hadrons with lifetimes can be identified by the positive-signed impact parameters after the resolutions effects being extracted.

The negative side of the signed impact parameter distribution can be used to measure the resolution functions. Tracks associated with jets are also categorized according to number of SVX hits and their resolutions. Each distribution is normalized and fit to a function $R(s)$, formed by two Gaussians plus exponential tails where s is the signed impact parameter. The track probability, $P_{track}(s)$, is then defined for tracks passing certainty quality cuts according to the integral probability that it have a signed impact parameter value of s or less.

$$P_{track}(s) = \int_{-\infty}^{-|s|} R(t)\,dt$$

Figure B.1 (a) shows a distribution of $P_{track}(s)$ for tracks with negative-signed im-

100

pact parameters in the generic jets data sample. The shape is essentially flat over most of the intervals as expected. There exist small peak near zero which indicates a slight excess of tracks with a larger $|s|$ compared to the expectation from the fit. Using the resolution functions for tracks passing the same quality cuts but with positive-signed impact parameters, the life time effects can be shown in figure B.1 (b). The excess of tracks with larger $|s|$ shown by a peak at smaller probabilities reveals the presence of long-lived particles in the events. In the following analysis, the resolution functions used for data and Monte Carlo jets are separately made using tracks in the generic jets events.

A jet probability is then obtained by combining the probabilities from tracks with *positive*-signed impact parameters in the jet using

$$P_{jet} = \Pi \sum_{k=0}^{N-1} \frac{(-ln\,\Pi)^k}{k!}$$

where $\Pi = P_1 P_2 \cdots P_N$ is the product of the probabilities. Figure B.2 shows the jet probability distribution for data events passing the jet 50 GeV trigger. There is excess in the first few bins in the plot and is attributed to real heavy flavor content in the data generic jets sample. A technique using the different jet probability shapes for b, c hadrons and non-heavy flavor jets due to the lifetime and fragmentation effects is used to measured the fraction of each flavor component.

B.2 The Fitting Method

Monte Carlo simulations are used to obtain the b and c jet probability shapes expected in data. Events are generated by PYTHIA 2 → 2 QCD pair production processes ($b\bar{b}$ and $c\bar{c}$) with full detector simulations. Figure B.3 shows the relative distributions expected for inclusive b, c decays and non-heavy flavor jets (referred as primary jets) in the Monte Carlo samples. These templates are used as inputs to a binned likelihood fitting for the data distribution, covering the range -10 to 0 in log_{10}(jet probability) with each content constrained to be positive in the fit. The fit results are then scaled by the acceptances to obtain the flavor content in the sample.

101
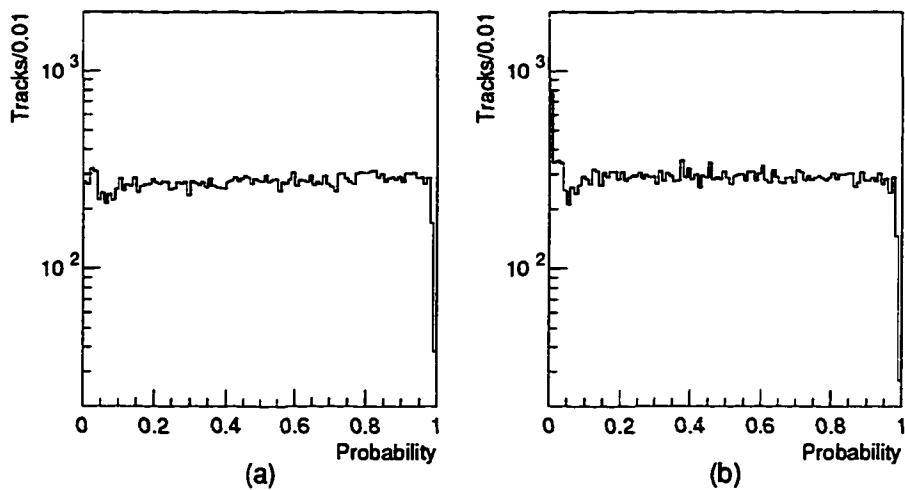
Figure B.1: The (a) negative and (b) positive sides of the track probability distributions in the data generic jet sample.
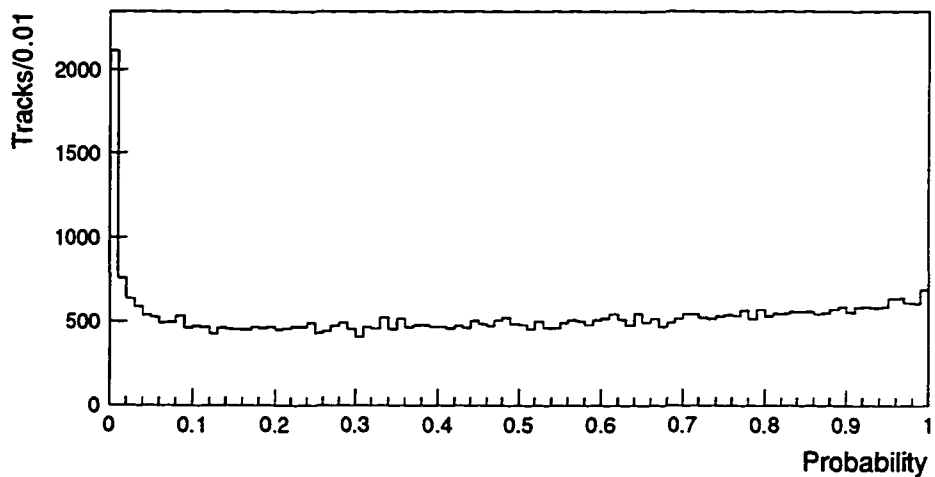
Figure B.2: The jet probability distribution for data events passing jet 50 GeV trigger.

102
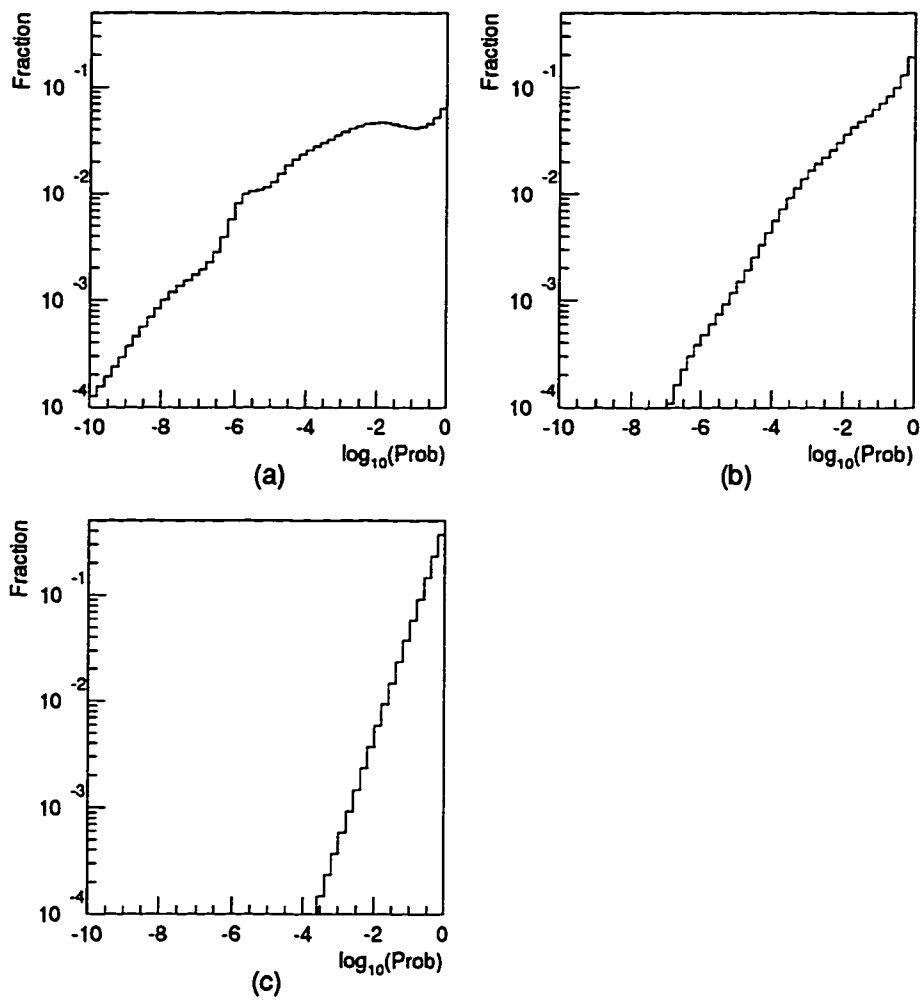
Figure B.3: The expected log_{10}(jet Probability) distributions for (a) bottom, (b) charm, and (c) primary jets. Distributions have been smoothed and normalized to the same area.

103

B.3 Systematics

The jet probability shapes obtained from the Monte Carlo simulations are expected to be able to represent those in the data. The assumption may not be correct due to the following uncertainties.

- Ability of detector simulations: Two systematics are considered.

    - Track multiplicity modeling: Number of tracks to form the jet probability is not only determined by the fragmentations but also by the detector simulation programs. The track multiplicity and jet probability correlate to each other. In general the more tracks exist in the jet, the lower jet probability is seen. This is shown in figure B.4 and B.5. The track multiplicity modeling ability of the Monte Carlo simulations can affect the shapes of the template.

    - Resolution modeling: The Monte Carlo jet probability is obtained from the resolution functions created by the impact parameter significance distribution of the Monte Carlo Jet50 events. The precision of the impact parameter model and the error estimation determine the models ability to simulate the jet probability shapes for the data. This can also affect the shapes of the template.

    In the next section, a comparison of the jet probability distributions between a $b\bar{b}$ data sample and Monte Carlo is made. The comparison also attempts to get correction factors which can be applied to the templates if there exists any discrepancy.

- Vertex finding ability: It has been found that the topology of jets recoiling against a single high P_T track can cause a bias in the shape of the jet probability in the W + 1 jet or γ + 1 jet events because few tracks can be used to determine the interaction vertex. This effects on the less energetic primary jets is more significant since these jets have fewer tracks than b or c jets on the average. Therefore the jet probability shape for the primary jets should be obtained from Monte Carlo simulations in each specific track multiplicity to obtain the best estimation.

104

- Monte Carlo generators: Different generators use different matrix element calculations for sub-processes, incoherent gluon emission and fragmentations. This affects the track multiplicity and the P_T spectrum of the tracks in the jets as well as the jet probability. It is shown in reference [48] that using template from different generators results in 5% uncertainty for the b fraction from the fit algorithm.

- b and c life time: There is a 5.8% uncertainty in the b lifetime measurement at CDF [69]. The uncertainty affect the impact parameter distribution of the Monte Carlo events. It is also shown in reference [48] that the effect results about 3% uncertainty on the fit results.

B.3.1 Check of the b and c Shapes

To examine whether the jet probability shapes are the same in data and Monte Carlo samples, the double-tagged events in the run 1b inclusive electron data from which most of the $b - \bar{b}$ events are selected are used for comparison. An event in the sample is required to have an electron track within cone size 0.4 of tagged-jet axis, a so-called electron jet, with $E_T \geq 15$ GeV and another away tagged jet. The electron jet sample is mostly semileptonic b decays while the away jet is mostly inclusive b decays. A PYTHIA ($b\bar{b} \rightarrow eX$) sample with detector simulations is used to compare with the data. Figures B.4 and B.5 show the jet probability distributions of Monte Carlo events. The distributions are found to be populated in lower regions than in the data in each of the track multiplicity bin.

A comparison of the number of tracks with positive impact parameter between data and Monte Carlo is shown in table B.1. Agreement is found in electron jet sample. The table shows that the lower jet probabilities found in the MC may not result from the track multiplicity modeling in the simulations. In additional to the track multiplicity dependences, there must be some subtlety in decay modeling and resolutions which result the differences shown between data and Monte Carlo. This should be understood in detail.

105

Track multiplicity		= 2	= 3	$\geq$ 4
Electron Jet:	Data	(45.4±1.6)%	(34.5±1.5)%	(20.1±1.3)%
	MC	(44.1±1.4)%	(35.9±1.4)%	(20.0±1.1)%
Away Jet:	Data	(27.8±1.4)%	(32.3±1.4)%	(39.9±1.5)%
	MC	(23.0±1.2)%	(32.3±1.4)%	(44.7±1.4)%

Table B.1: Comparison between fractions of good SVX tracks with positive-impact parameter in the ($b\bar{b} \rightarrow eX$) events between data and MC samples.

Inclusive b decays			
Track multiplicity	= 2	= 3	$\geq$ 4
$\frac{jetprob(DATA)}{jetprob(MC)}$	2.74	6.12	8.95

Table B.2: Correction factors for the jet probability in each of the track multiplicity bin.

For now, a simple scale correction is applied on the Monte Carlo distribution to include all other effects.

The correction is a single scale factor which is the ratio of the mean values of the away jet distributions in each of the track multiplicity bin. The mean values in the away jet sample are used because there is no requirement for the electron track present in these jets. Table B.2 list the correction factors in each of the track multiplicity bin. The correction factors could be even larger if the data sample, presumed all b jets, has a significant contamination from c or primary jets. Figure B.6 shows the Monte Carlo jet probability shapes of the away jets in the ($b\bar{b} \rightarrow eX$) events before and after the corrections overlayed with the data distribution. The corrected Monte Carlo shape agrees well with the data distribution. Discrepancy in the last 3 bins ($-0.6 \leq log(jetprob) < 0$) is ignored because these 3 bins only containing $\sim$ 1% of the events and the disagreement may be due to the statistical fluctuation. The same correction factor in each of the track multiplicity bin is applied on the b and c jet probability shapes without tagging requirement.

106
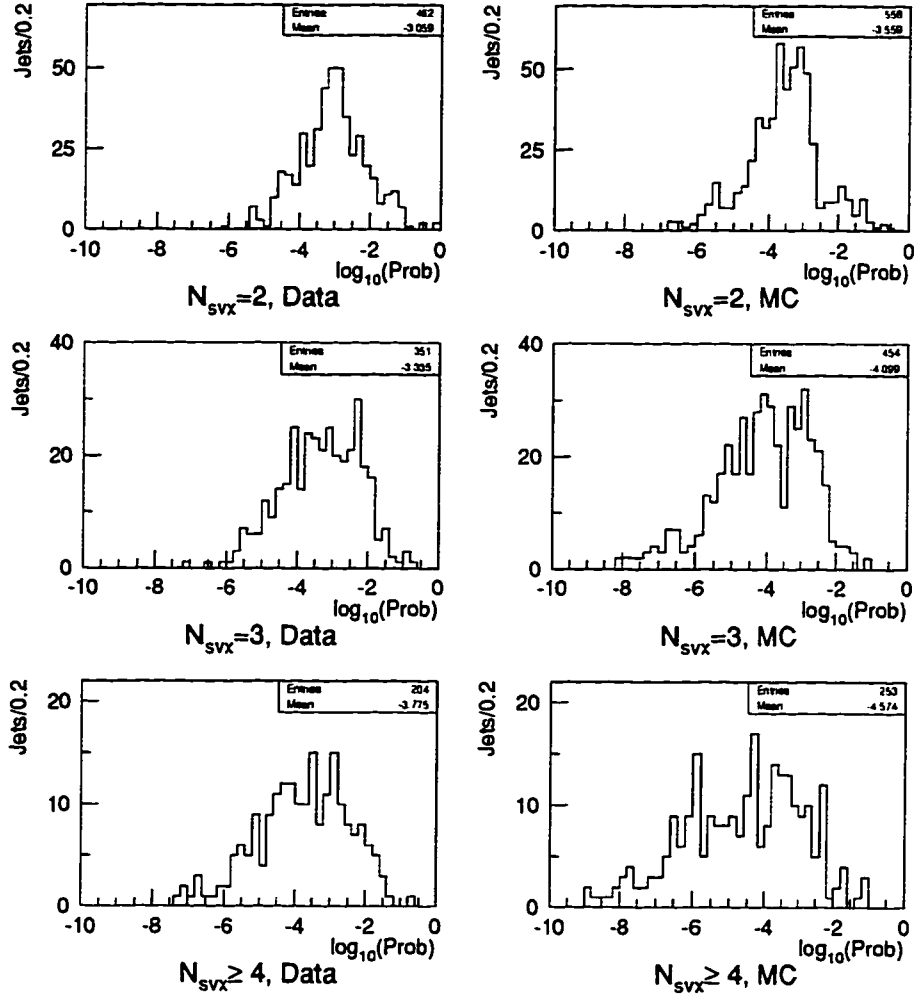
Figure B.4: The log_{10}(jet probability) distributions of the semileptonic b decays in each of the track multiplicity bin.

107
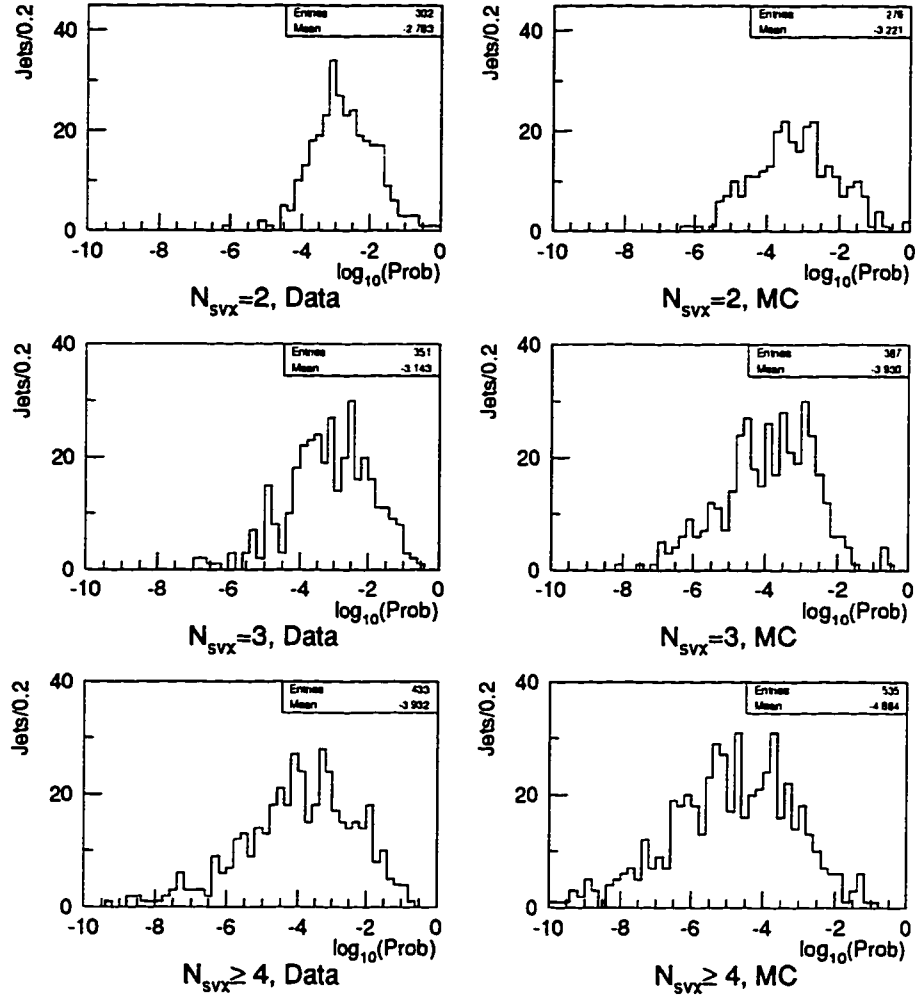
Figure B.5: The log_{10}(jet probability) distributions of the inclusive b decays in each of the track multiplicity bin.

108
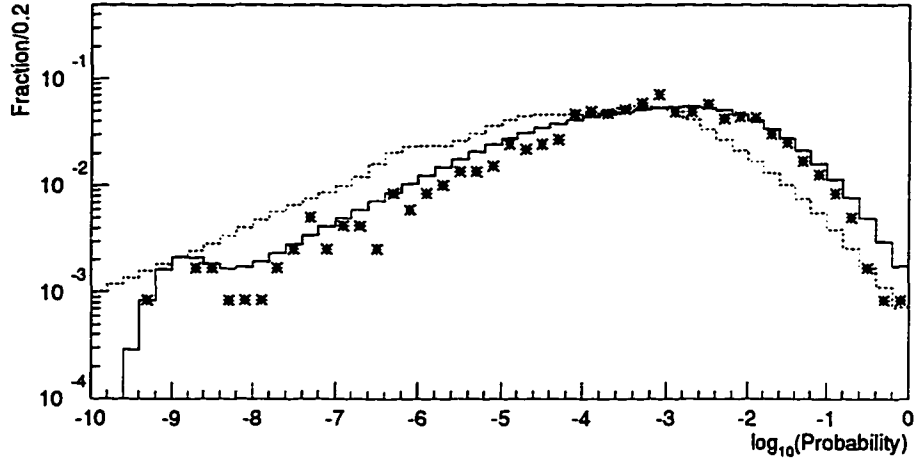
Figure B.6: The log_{10}(jet probability) distributions of the inclusive b decays in data (star) with comparison to those of Monte Carlo samples before (dot line) and after (solid line) the corrections.

B.3.2 Test of the Fit Algorithm

The self-consistence of the fit algorithm is tested using two samples containing a total of 1,000 and 10,000 jets respectively which are made of different fractions of b, c, and primary jet. A hundred test fits are made for four different flavor combinations in each sample. The test data shapes are made by summing the b, c and primary jet probabilities which are obtained from a random selection based on the shapes of the template. The mean and error of the fit output are shown in table B.3. Results show that the fit technique is able to predict the flavor content, but the statistical power for measuring the amount of the b, c and primary jets depends on the parent distribution. As listed in the table, group 1 and 4 show cases where each flavor content can be measured separately, while group 2 and 3 show less sensitivity on the charm fraction. This is expected since the charm template lies between shapes of the bottom and primary jets, and the fit power may have been washed out in some cases.

109

Group	(1)	(2)	(3)	(4)
Given fractions	40% b	30% b	5% b	0% b
	40% c	10% c	5% c	50% c
	20% p	60% p	90% p	50% p
1,000 jets sample	395±5 b	294±4 b	47±2 b	9±5 b
	406±8 c	107±11 c	58±7 c	480±4 c
	199±4 p	599±5 p	896±4 p	511±2 p
10,000 jets sample	3978±16 b	2982±14 b	500±7 b	20±10 b
	4038±27 c	1030±24 c	495±15 c	4954±15 c
	1984±14 p	5988±15 p	9005±14 p	5026±13 p

Table B.3: Test fit results from samples with different fractions of b, c and primary jets.

B.4 Flavor Fit in the Electron Data

The inclusive b content in the electron data can be measured to study the tagging efficiency by fitting the jet probability distribution of the taggable jets. Table B.4 gives the fit results in the run 1B electron data. The errors shown in the table are from the likelihood fit only. The superposition of the fit on the jet probability distributions is shown in figure B.7. A common uncertainty of 6.5% resulting from the lifetime and resolution effects is not included. Using the Monte Carlo simulations to obtain the acceptances for the fraction of taggable jets with the jet probability, which is listed in table B.5, the final results of the b content in the inclusive jets sample has been shown in table 4.1.

B.5 Flavor Fit in the W + Jets Samples

Tags in the W + jets samples come from various sources including $t\bar{t}$ events and backgrounds. It has been found that most of the tags from $t\bar{t}$ events are b hadrons while backgrounds give b, c and non-heavy flavor tags. A crosscheck can be made by comparing the flavor contents calculated from the $t\bar{t}$ production cross section measurement to the results obtained from the jet probability fit.

110

E_T(GeV)	10-15	15-20	20-25	25-30	30-35	35-45	45-
Taggable jets	110994	60085	32034	16630	8764	7204	3746
Used in fit	40828	26251	15412	8430	4723	3988	2183
Fit Results:							
b	4764 ±199	5038 ±175	3214 ±136	1934 ±104	906 ±69	781 ±65	286 ±40
c	6680 ±347	1887 ±287	1048 ±221	136 ±166	232 ±115	144 ±108	300 ±73
p	29382 ±255	19325 ±207	11148 ±159	6359 ±119	3585 ±88	3062 ±82	1596 ±60

Table B.4: Results of jet probability fit in the low E_T inclusive electron dataset. Errors shown are statistic only.

E_T(GeV)	10-15	15-20	20-25	25-30	30-35	35-45	45-
b (%)	50.8±0.8	62.8±0.9	69.4±1.0	75.1±1.3	77.3±1.7	81.7±1.8	84.1±3.4
c (%)	43.7±0.4	52.3±0.6	57.6±1.0	62.8±1.6	61.5±2.5	68.3±3.0	64.7±8.2
p (%)	36.0±0.4	45.5±0.4	50.7±0.5	55.6±0.5	58.5±0.5	62.4±0.4	65.5±0.5

Table B.5: Fractions of b, c, and primary jets have jet probabilities observed in the taggable jets sample. Errors shown reflect statistics only.

111
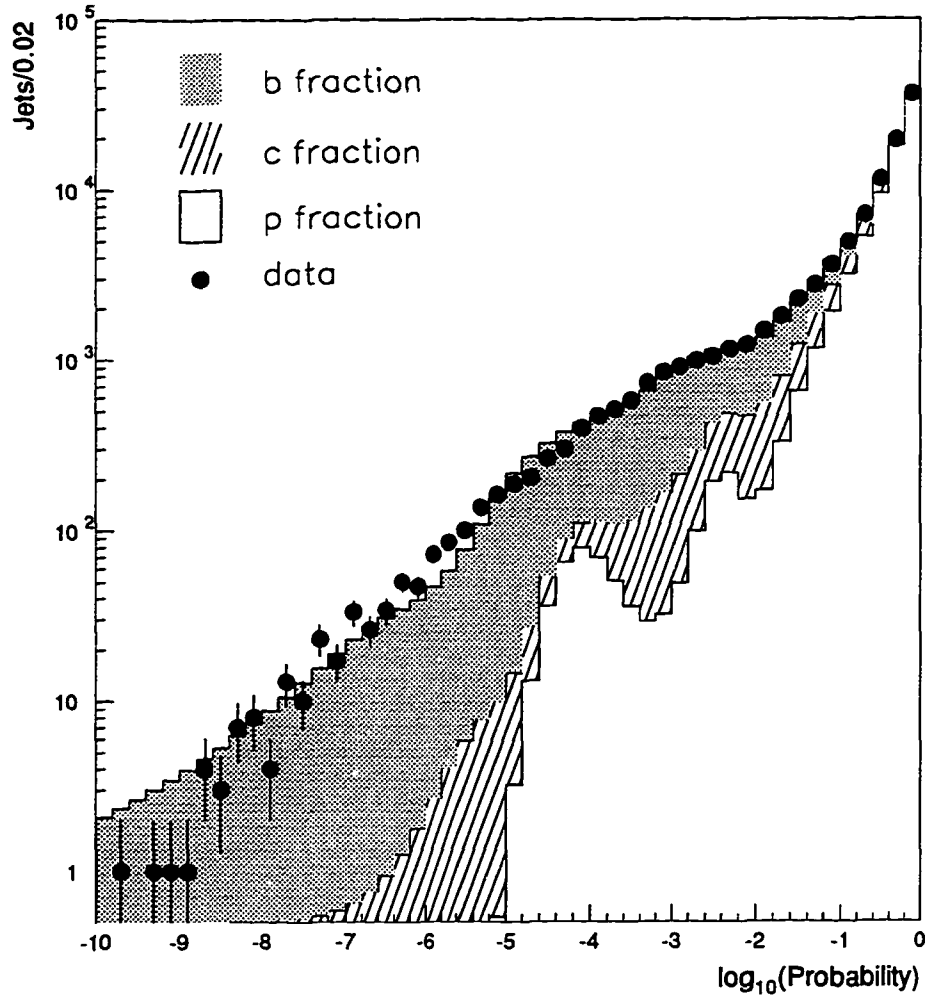
Figure B.7: The log_{10}(jet probability) distribution of inclusive jets in the run 1B electron data, overlayed with the fit results. Statistical errors on the data are included.

112

Corrected b and c templates used in the fit are described in the previous sections. The template for the primary jets is obtained from a VECBOS $W + n$ jets Monte Carlo sample to simulate the possible vertexing bias. The fit results are shown in table B.6 and the errors shown are from the fit only. The superposition of the fit on the jet probability distributions is shown in figure B.8, B.9 and B.10. Plots clearly show the existence of the bottom and charm hadrons in the sample. The flavor content can be obtained after scaling the fit output by the acceptances. The acceptances are studied in the Monte Carlo sample to measure the fraction of jets may have jet probability in each flavor content. The numbers are normalized to the E_T spectrum of the data with uncertainties estimated to be within 5%. As shown in the table, a 20% discrepancy is found between total number of jets in the data and the sum of the three components. This may due be to variations in the acceptance of the primary jet which is not well understood. A 25% change on the acceptance of the primary jets would have resulted the same discrepancy in the total number of jets shown here. In any case, the b and c content is not affected.

The measurement not only finds the b and c components but also serves as a cross-check to the results of the $t\bar{t}$ cross section measurement. A $t\bar{t}$ production cross section, 6.0 pb, and the background numbers shown in chapter 6 are used to estimate the content of the tags. Estimation is shown in table B.7. Also listed is a comparison to the results of the jet probability fit which has been scaled by the corresponding tag rates. A good agreement is found among the numbers as well as the actual tags observed in the $W +$ jets samples.

Studies of the bottom, charm and mistag components in the W + jets samples using jet probability algorithm have been presented. The technique directly determines each flavor component from data instead of using massive Monte Carlo simulation. Number of tagged jets predicted from the measurement is not only consistent with the Monte Carlo predictions but also agrees with data within the large statistical error of the present data size.

113

	W + 1 jet	W + 2 Jets	W + ≥3 Jets
Jets in data	8853	2738	886
Jets used in fit	1906	612	224
Fit results:			
b	73±23	62±20	50±18
c	151±50	98±37	37±30
p	1682±52	452±30	138±20
After scaled by acceptances:			
b	177±56	146±47	114±41
c	409±136	256±97	94±77
p	6520±203	1668±112	492±71

Table B.6: Summary of the flavor contents in the run 1B W + jets samples. Error shown are from the fit only.

	W + 1 jet		W + 2 Jets		W + ≥3 Jets	
	(a)	(b)	(a)	(b)	(a)	(b)
b	40.8±13.0	23.0±8.0	35.7±11.5	20.3±7.1	28.4±10.2	35.0±12.3
c	20.8± 7.0	26.2± 9.2	14.1± 5.4	8.2±2.9	5.3± 4.4	3.3± 1.2
p	10.1± 0.3	10.7± 3.7	2.6± 0.2	3.6±1.3	0.8± 0.1	1.2±0.4
Sum	71.7±20.3	59.9±20.9	52.4±17.1	32.1±11.3	34.5±14.7	39.6±13.9
Data	63		43		37	

Table B.7: Listed in (a) are number of tags predicted by the fit algorithm (fit error shown only) and (b) are number of tags from each flavor in the $t\bar{t}$ production cross section measurement. Tags observed in the run 1B W + jets data are also shown.

114
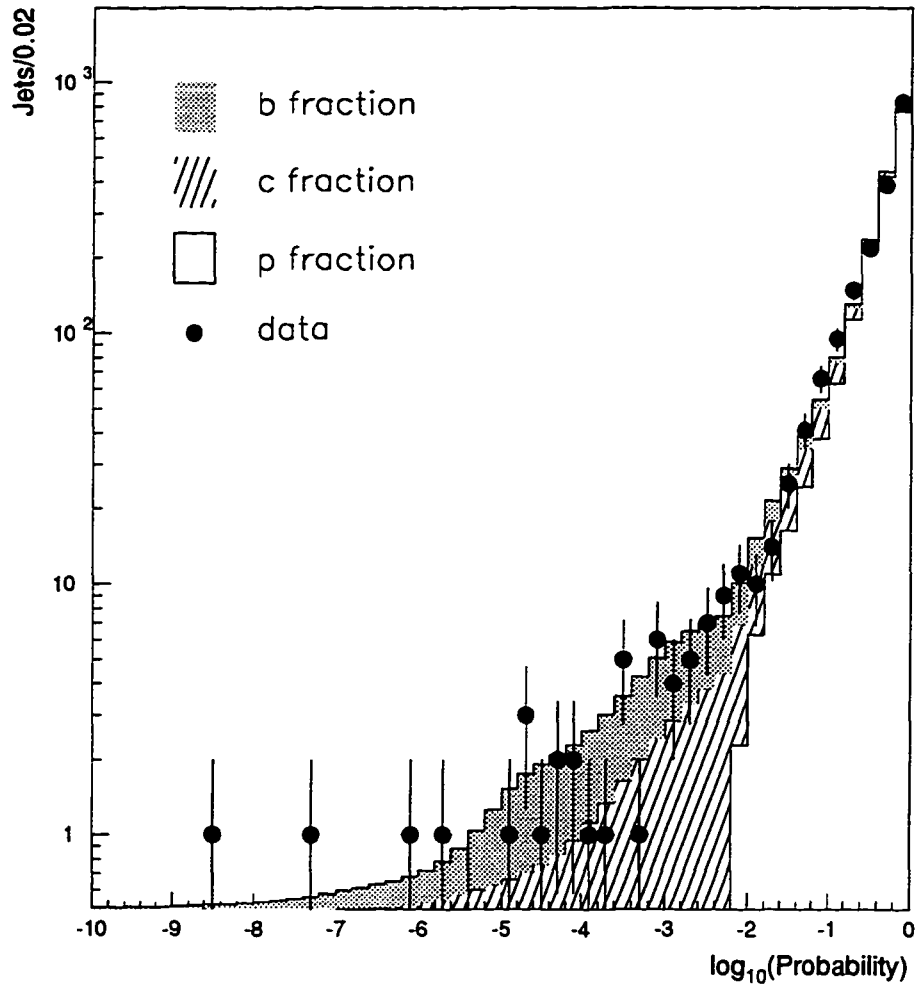
Figure B.8: The run 1B $W + 1$ jet log_{10}(jet probability) distribution overlayed with the fit results. Statistical errors on the data are included.

115
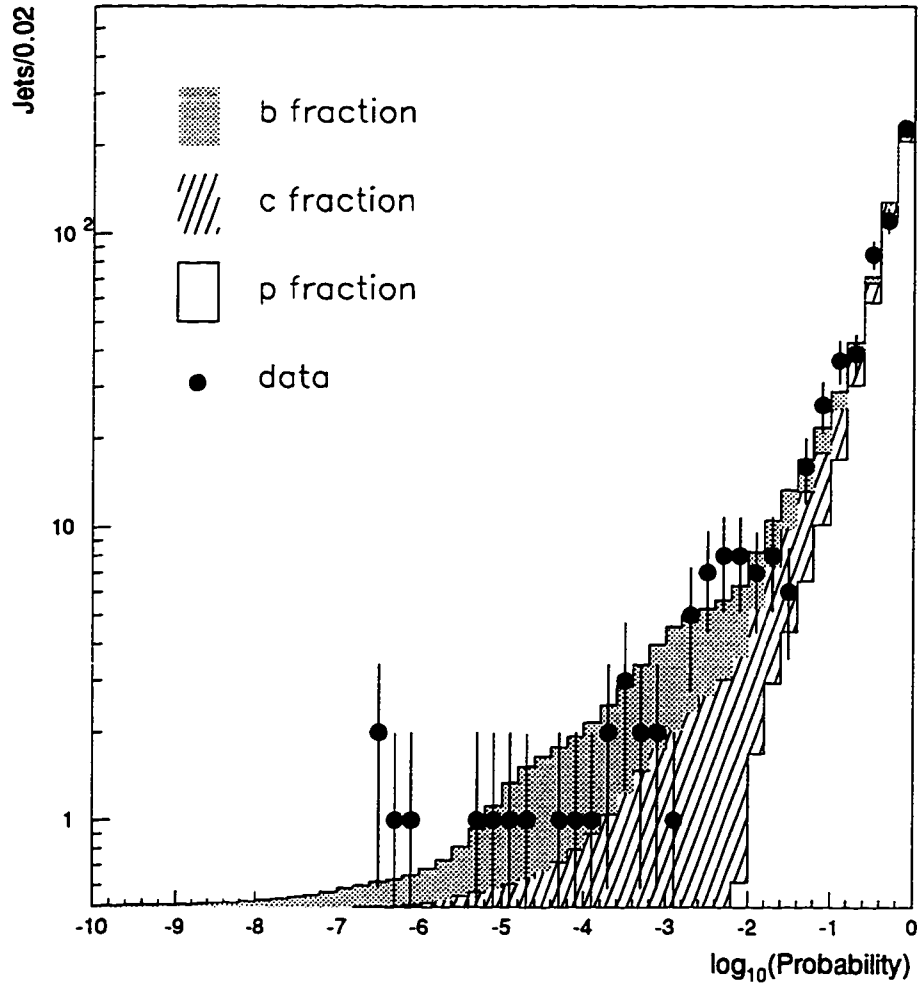
Figure B.9: The run 1B W + 2 jets log_{10}(jet probability) distribution overlayed with the fit results. Statistical errors on the data are included.

116
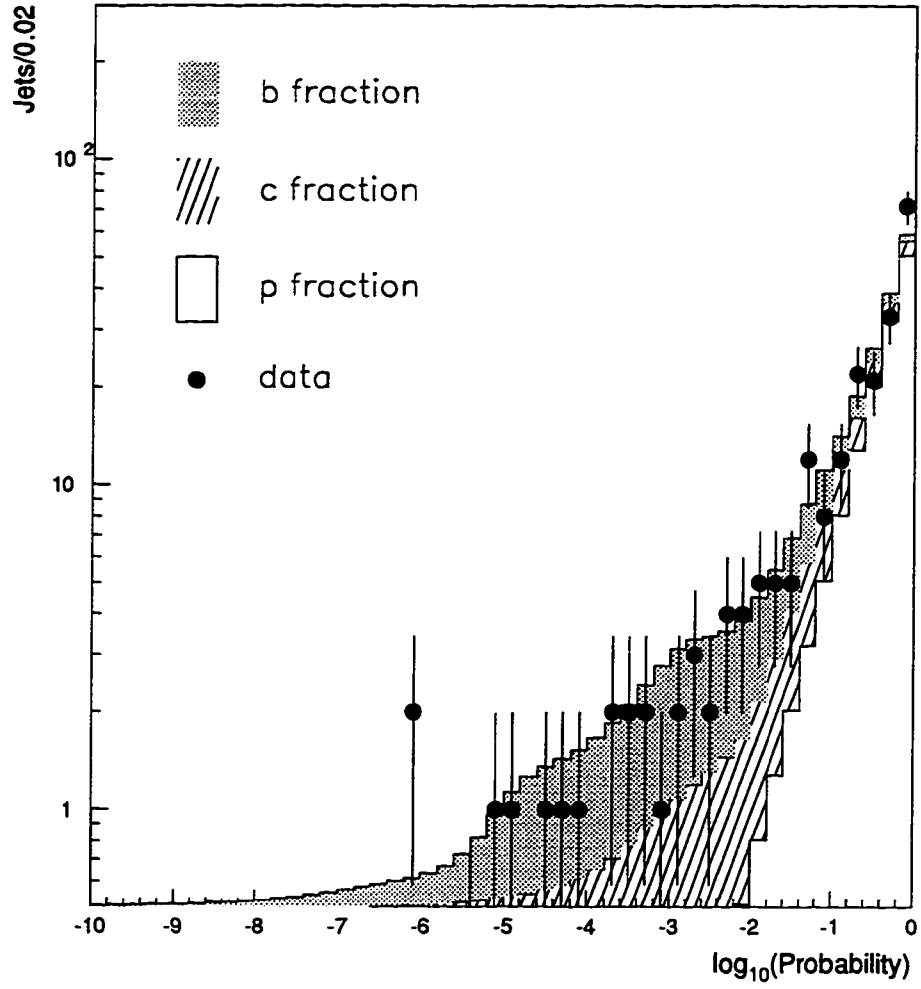
Figure B.10: The run 1B $W + \geq 3$ jets log_{10}(jet probability) distribution overlayed with the fit results. Statistical errors on the data are included.

117

Appendix C

Determination of Systematics for Tracking-finding Degradation

The efficiency of the tagging algorithm used in the search for $t\bar{t}$ signals was determined using a scale factor, the ratio of tagging efficiency between numbers derived from low E_T inclusive electron data and Monte Carlo simulation [3]. Restricted by the low statistics of higher E_T jets in the sample and the different kinematics between semileptonic b decay and the totally inclusive b decay for $t\bar{t}$ events, an improved method using degradation on the track-finding efficiency in the detector simulation program is now used to determine the tagging efficiency directly from $t\bar{t}$ Monte Carlo events. To evaluate the systematic uncertainties for the method, the kinematic features of a $b\bar{b}$ Monte Carlo are compared to those in data. In addition, by checking the changes of the tagging efficiencies resulting from the degradation of the track-finding efficiency in the $t\bar{t}$ Monte Carlo samples, dependences on the jet E_T and top mass are examined.

C.1 Track Multiplicity of b Decays

Comparison of kinematic features between data and Monte Carlo events, such as invariant mass, summed P_T and $c\tau$ of the tagged jets, has been made and well understood. The following studies focus on the comparison of the track multiplicity of the jets between the data and Monte Carlo events with and without the track-finding efficiency degraded.

118

Tracks passing different selection criteria are examined. These include

- SVX tracks: Tracks reconstructed by silicon vertex detector

- Pass 0 tracks: SVX tracks passing the loose selection criteria without impact parameter significance cut described in chapter 4.3

- Pass 1 tracks: Pass 0 tracks passing the impact parameter significance cut

- Vertex tracks: Tracks attached to the secondary vertex in the tagged jets

The run 1B low E_T inclusive electron data is used to make the comparison. The instantaneous luminosity distribution of the sample has been proved to be close to that in W + jets sample. Therefore no additional systematic uncertainty due to the instantaneous luminosity dependence need to be added into the final results. A $b\bar{b}$ data sample is selected from the sample by requiring both electron and away jets in the events are tagged. The same event selection criteria as used in data is applied on the Monte Carlo $b\bar{b}$ sample. Based on the density of the hits around the track, the track-finding efficiency in the simulations has been degraded.

Figure C.1 compares the number of SVX tracks, pass 0 tracks, pass 1 tracks and vertex tracks of the tagged electron jets among the data and Monte Carlo samples. Agreement is seen between the distributions in all E_T bins within the statistic errors. Less than 3% difference is found between data and Monte Carlo events. Note the degradation does not result in significant differences to the track multiplicities in the sample. Apparently modeling ability for the inclusive b decays shown in Figure C.2 is not as good as that in the semileptonic b decays. More tracks are found in the Monte Carlo events. The degradation does decrease the track multiplicities and toward the direction to match the distribution of data inclusive b decays.

The different E_T-dependent modeling ability in Monte Carlo simulation for the semileptonic and inclusive b decays can also be found. Ratios of number of pass 0 tracks to that of SVX tracks, number of pass 1 tracks to that of pass 0 tracks, and number of the

119

vertex tracks to that of pass 1 tracks are shown in figure C.3. Plots indicate a better Monte Carlo modeling in the electron jets, i.e. in the semileptonic b decays. The disagreement is still found even if the degradation has been applied on the inclusive b decays. Results of the comparison explain the reason why the scale factors for the semilepton b decays are always found to be closer to 1.0 than those for the inclusive b decays. Because the tagging efficiency depends on the number of tracks which can be used in the vertexing, differences in the ratio of vertex tracks to the pass 0 tracks between degraded Monte Carlo and data may used to measure the size of the discrepancy still seen in the tagging efficiency. Therefore a 7% systematic uncertainty is assigned to the tagging efficiency measured using the degradation method.

C.2 Tagging Efficiency in the $t\bar{t}$ Events

Applying the degradation results in a lower event tagging efficiency in the Monte Carlo $t\bar{t}$ sample. To investigate the change as a function of the b jet E_T, efficiencies obtained with and without degradation are compared. Figure C.4 shows the b-tagging efficiencies measured in the $t\bar{t}$ sample with top mass set to 175 GeV/c^2. The average b jet tagging efficiency is changed from 0.555 ± 0.004 (stat) for standard simulation to 0.473 ± 0.004 (stat) after the degradation. No significant E_T dependence on the scale factor is seen.

Several $t\bar{t}$ Monte Carlo samples with different top mass are also examined. Figure C.5 shows b jet tagging efficiencies as a function of top mass where little difference is observed. This is expected because the same b decay table is still used in the event generator level, and the degradation is applied on the tracking which is not explicitly related to the jet E_T spectrum. Therefore applying degradation on the track-finding efficiency is proven to achieve a reasonable accuracy for the measurement of tagging efficiency.

120
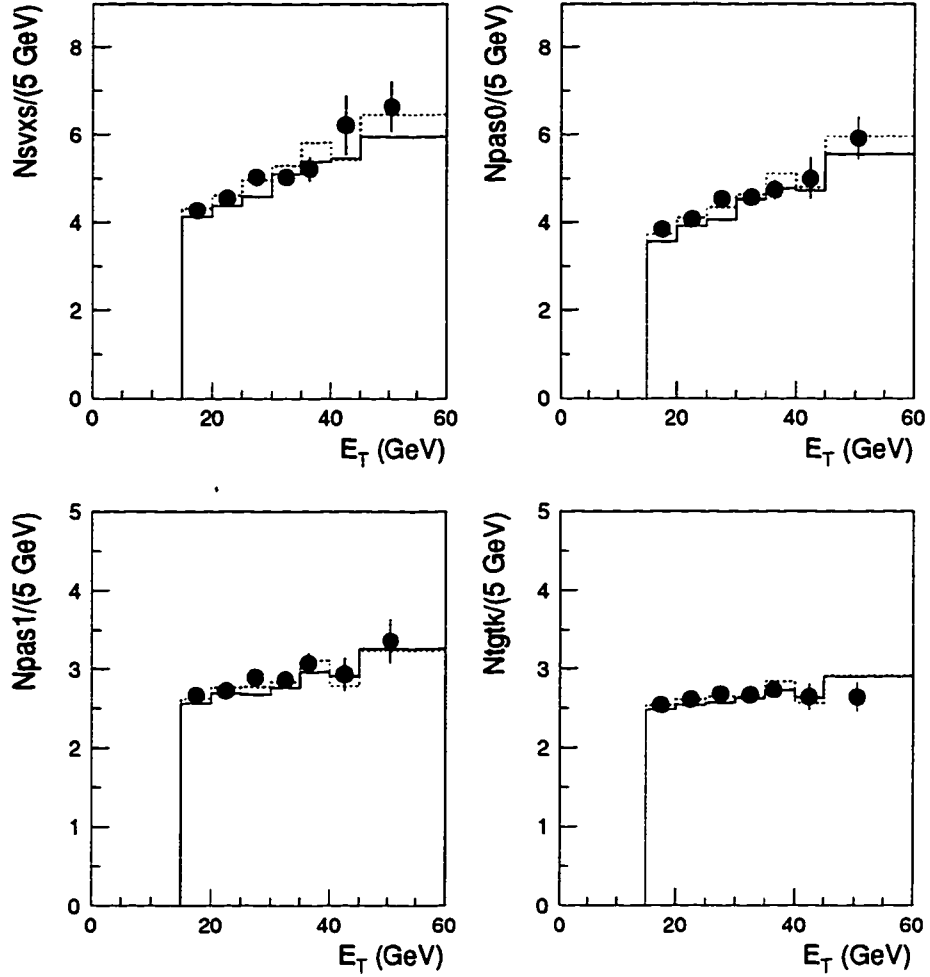
Figure C.1: Distributions of number of SVX tracks, pass 0 tracks pass 1 tracks and the vertex tracks of the tagged *electron* jets observed in data(points), Monte Carlo samples before (dot histogram) and after (solid histogram) track-finding efficiency degraded

121
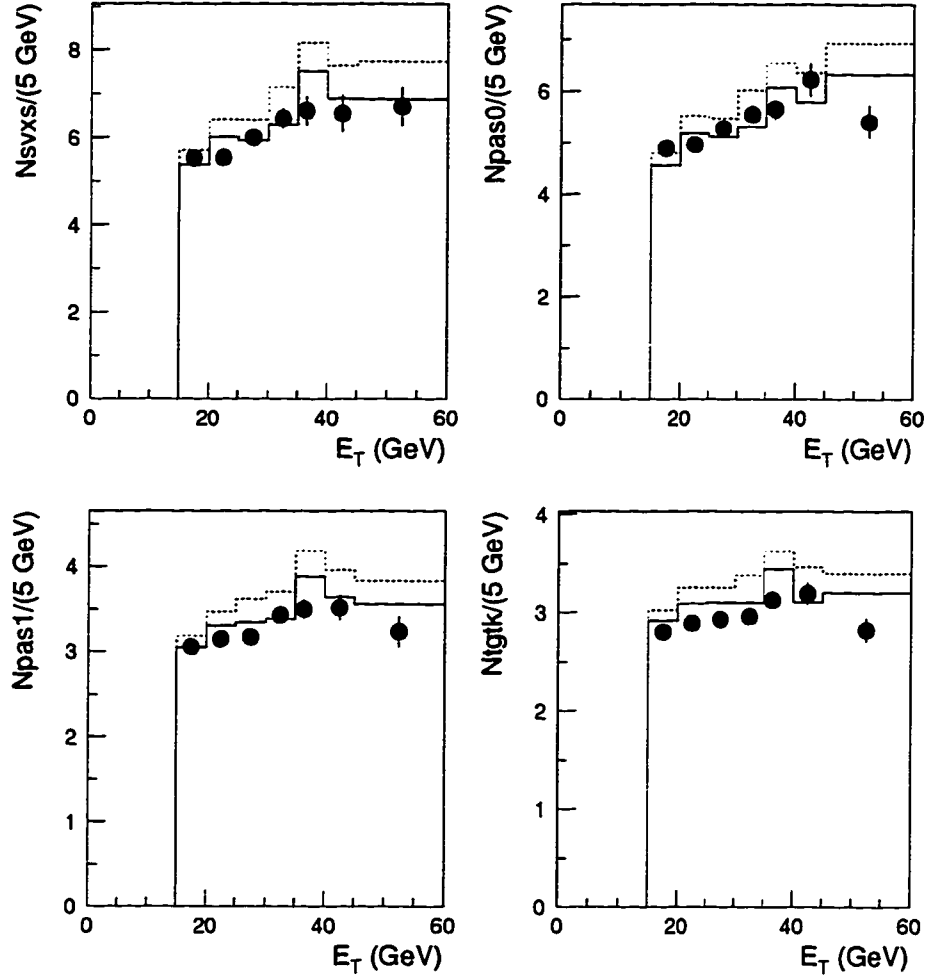
Figure C.2: Distributions of number of SVX tracks, pass 0 tracks pass 1 tracks and the vertex tracks of the tagged *away* jets observed in data(points), Monte Carlo samples before (dot histogram) and after (solid histogram) track-finding efficiency degraded

122
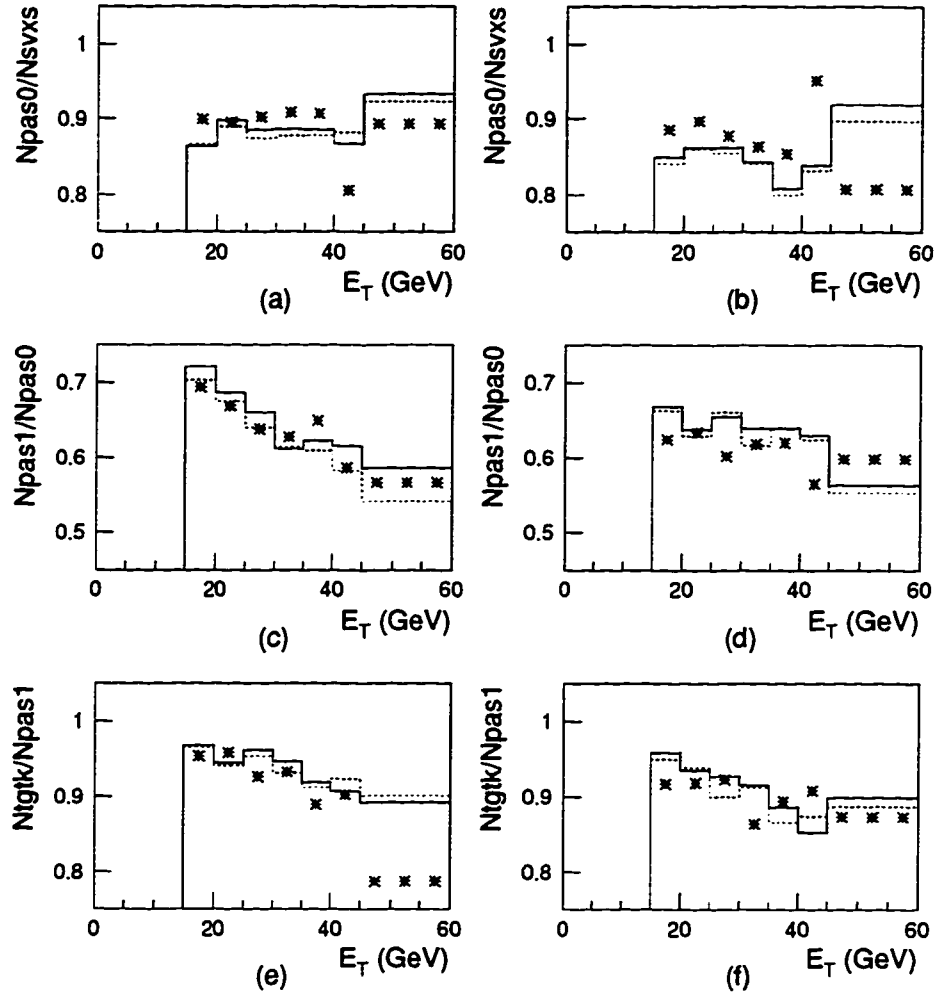
Figure C.3: Fractions of tracks passed the different criteria of selections. (a)(c)(e) for semileptonic b decays and (b)(d)(f) for inclusive b decays observed in data (star), Monte Carlo samples before (dot histogram) and after (solid histogram) track-finding efficiency degraded

123
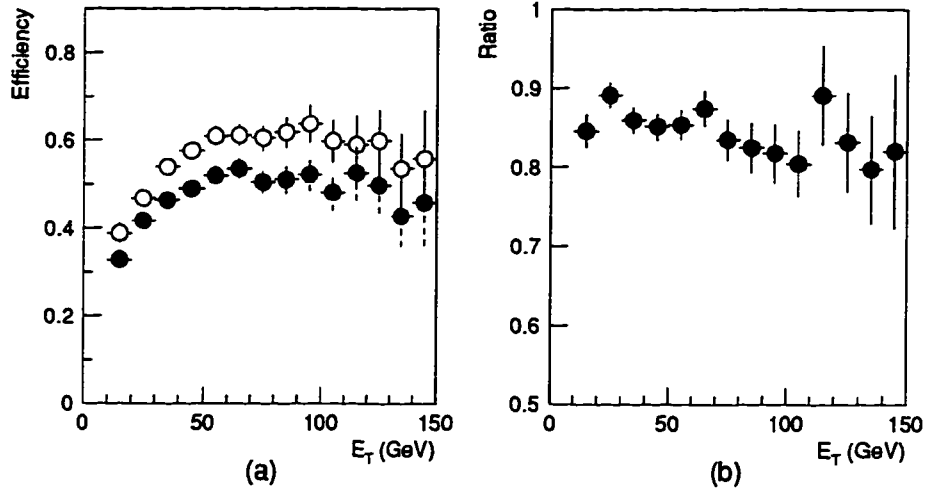
Figure C.4: (a) The jet-tagging efficiency and (b) scale ratios as a function of jet E_T in the $t\bar{t}$ Monte Carlo with top mass set to 175 GeV/c^2.
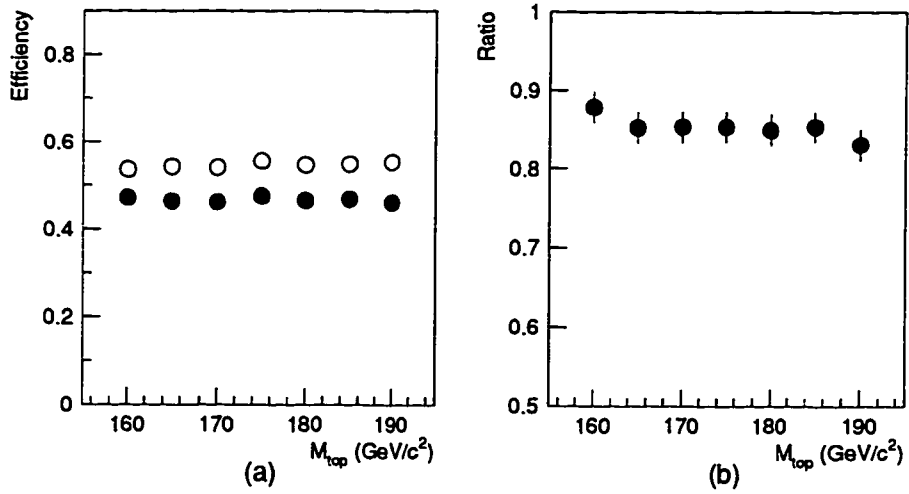
Figure C.5: (a) The jet-tagging efficiency and (b) scale ratios as a function of top mass.

124

Appendix D

The CDF Collaboration

F. Abe,[15] H. Akimoto,[34] A. Akopian,[29] M. G. Albrow,[7] S. R. Amendolia,[25] D. Amidei,[18] J. Antos,[31] C. Anway-Wiese,[4] S. Aota,[34] G. Apollinari,[29] T. Asakawa,[34] W. Ashmanskas,[16] M. Atac,[7] F. Azfar,[24] P. Azzi-Bacchetta,[23] N. Bacchetta,[23] W. Badgett,[18] S. Bagdasarov,[29] M. W. Bailey,[20] J. Bao,[37] P. de Barbaro,[28] A. Barbaro-Galtieri,[16] V. E. Barnes,[27] B. A. Barnett,[14] E. Barzi,[8] G. Bauer,[17] T. Baumann,[10] F. Bedeschi,[25] S. Behrends,[3] S. Belforte,[25] G. Bellettini,[25] J. Bellinger,[36] D. Benjamin,[33] J. Benlloch,[17] J. Bensinger,[3] D. Benton,[24] A. Beretvas,[7] J. P. Berge,[7] J. Berryhill,[5] S. Bertolucci,[8] B. Bevensee,[24] A. Bhatti,[29] K. Biery,[13] M. Binkley,[7] D. Bisello,[23] R. E. Blair,[1] C. Blocker,[3] A. Bodek,[28] W. Bokhari,[17] V. Bolognesi,[2] G. Bolla,[23] D. Bortoletto,[27] J. Boudreau,[26] L. Breccia,[2] C. Bromberg,[19] N. Bruner,[20] E. Buckley-Geer,[7] H. S. Budd,[28] K. Burkett,[18] G. Busetto,[23] A. Byon-Wagner,[7] K. L. Byrum,[1] J. Cammerata,[14] C. Campagnari,[7] M. Campbell,[18] A. Caner,[25] W. Carithers,[16] D. Carlsmith,[36] A. Castro,[23] D. Cauz,[25] Y. Cen,[28] F. Cervelli,[25] P. S. Chang,[31] P. T. Chang,[31] H. Y. Chao,[31] J. Chapman,[18] M. -T. Cheng,[31] G. Chiarelli,[25] T. Chikamatsu,[34] C. N. Chiou,[31] L. Christofek,[12] S. Cihangir,[7] A. G. Clark,[9] M. Cobal,[25] E. Cocca,[25] M. Contreras,[5] J. Conway,[30] J. Cooper,[7] M. Cordelli,[8] C. Couyoumtzelis,[9] D. Crane,[1] D. Cronin-Hennessy,[6] R. Culbertson,[5] T. Daniels,[17] F. DeJongh,[7] S. Delchamps,[7] S. Dell'Agnello,[25] M. Dell'Orso,[25] R. Demina,[7] L. Demortier,[29] B. Denby,[25] M. Deninno,[2] P. F. Derwent,[7] T. Devlin,[30] J. R. Dittmann,[6] S. Donati,[25] J. Done,[32] T. Dorigo,[23] A. Dunn,[18] N. Eddy,[18] K. Einsweiler,[16] J. E. Elias,[7] R. Ely,[16] E. Engels, Jr.,[26] D. Errede,[12] S. Errede,[12] Q. Fan,[27] C. Ferretti,[25] I. Fiori,[2] B. Flaugher,[7] G. W. Foster,[7] M. Franklin,[10] M. Frautschi,[33] J. Freeman,[7] J. Friedman,[17] H. Frisch,[5] T. A. Fuess,[1] Y. Fukui,[15] S. Funaki,[34] G. Gagliardi,[25] S. Galeotti,[25] M. Gallinaro,[23] M. Garcia-Sciveres,[16] A. F. Garfinkel,[27] C. Gay,[10] S. Geer,[7] D. W. Gerdes,[14] P. Giannetti,[25] N. Giokaris,[29] P. Giromini,[8] G. Giusti,[25] L. Gladney,[24] D. Glenzinski,[14] M. Gold,[20] J. Gonzalez,[24] A. Gordon,[10] A. T. Goshaw,[6] K. Goulianos,[29] H. Grassmann,[25] L. Groer,[30] C. Grosso-Pilcher,[5] G. Guillian,[18] R. S. Guo,[31] C. Haber,[16] E. Hafen,[17] S. R. Hahn,[7] R. Hamilton,[10] R. Handler,[36] R. M. Hans,[37] K. Hara,[34] A. D. Hardman,[27] B. Harral,[24] R. M. Harris,[7] S. A. Hauger,[6] J. Hauser,[4] C. Hawk,[30] E. Hayashi,[34] J. Heinrich,[24]

125

K. D. Hoffman,[27] M. Hohlmann,[5] C. Holck,[24] R. Hollebeek,[24] L. Holloway,[12] A. Hölscher,[13]
S. Hong,[18] G. Houk,[24] P. Hu,[26] B. T. Huffman,[26] R. Hughes,[21] J. Huston,[19] J. Huth,[10]
J. Hylen,[7] H. Ikeda,[34] M. Incagli,[25] J. Incandela,[7] G. Introzzi,[25] J. Iwai,[34] Y. Iwata,[11]
H. Jensen,[7] U. Joshi,[7] R. W. Kadel,[16] E. Kajfasz,[23] H. Kambara,[9] T. Kamon,[32]
T. Kaneko,[34] K. Karr,[35] H. Kasha,[37] Y. Kato,[22] T. A. Keaffaber,[27] L. Keeble,[8] K. Kelley,[17]
R. D. Kennedy,[30] R. Kephart,[7] P. Kesten,[16] D. Kestenbaum,[10] R. M. Keup,[12] H. Keutelian,[7]
F. Keyvan,[4] B. Kharadia,[12] B. J. Kim,[28] D. H. Kim,[7a] H. S. Kim,[13] S. B. Kim,[18]
S. H. Kim,[34] Y. K. Kim,[16] L. Kirsch,[3] P. Koehn,[28] K. Kondo,[34] J. Konigsberg,[10] S. Kopp,[5]
K. Kordas,[13] A. Korytov,[17] W. Koska,[7] E. Kovacs,[7a] W. Kowald,[6] M. Krasberg,[18]
J. Kroll,[7] M. Kruse,[28] T. Kuwabara,[34] S. E. Kuhlmann,[1] E. Kuns,[30] A. T. Laasanen,[27]
N. Labanca,[25] S. Lammel,[7] J. I. Lamoureux,[3] T. LeCompte,[1] S. Leone,[25] J. D. Lewis,[7]
P. Limon,[7] M. Lindgren,[4] T. M. Liss,[12] N. Lockyer,[24] O. Long,[24] C. Loomis,[30] M. Loreti,[23]
J. Lu,[32] D. Lucchesi,[25] P. Lukens,[7] S. Lusin,[36] J. Lys,[16] K. Maeshima,[7] A. Maghakian,[29]
P. Maksimovic,[17] M. Mangano,[25] J. Mansour,[19] M. Mariotti,[23] J. P. Marriner,[7] A. Martin,[12]
J. A. J. Matthews,[20] R. Mattingly,[17] P. McIntyre,[32] P. Melese,[29] A. Menzione,[25]
E. Meschi,[25] S. Metzler,[24] C. Miao,[18] T. Miao,[7] G. Michail,[10] R. Miller,[19] H. Minato,[34]
S. Miscetti,[8] M. Mishina,[15] H. Mitsushio,[34] T. Miyamoto,[34] S. Miyashita,[34] N. Moggi,[25]
Y. Morita,[15] J. Mueller,[26] A. Mukherjee,[7] T. Muller,[4] P. Murat,[25] H. Nakada,[34] I. Nakano,[34]
C. Nelson,[7] D. Neuberger,[4] C. Newman-Holmes,[7] M. Ninomiya,[34] L. Nodulman,[1] S. H. Oh,[6]
K. E. Ohl,[37] T. Ohmoto,[11] T. Ohsugi,[11] R. Oishi,[34] M. Okabe,[34] T. Okusawa,[22]
R. Oliveira,[24] J. Olsen,[36] C. Pagliarone,[2] R. Paoletti,[25] V. Papadimitriou,[33] S. P. Pappas,[37]
N. Parashar,[25] S. Park,[7] A. Parri,[8] J. Patrick,[7] G. Pauletta,[25] M. Paulini,[16] A. Perazzo,[25]
L. Pescara,[23] M. D. Peters,[16] T. J. Phillips,[6] G. Piacentino,[2] M. Pillai,[28] K. T. Pitts,[7]
R. Plunkett,[7] L. Pondrom,[36] J. Proudfoot,[1] F. Ptohos,[10] G. Punzi,[25] K. Ragan,[13]
D. Reher,[16] A. Ribon,[23] F. Rimondi,[2] L. Ristori,[25] W. J. Robertson,[6] T. Rodrigo,[25]
S. Rolli,[25] J. Romano,[5] L. Rosenson,[17] R. Roser,[12] W. K. Sakumoto,[28] D. Saltzberg,[5]
A. Sansoni,[8] L. Santi,[25] H. Sato,[34] P. Schlabach,[7] E. E. Schmidt,[7] M. P. Schmidt,[37]
A. Scribano,[25] S. Segler,[7] S. Seidel,[20] Y. Seiya,[34] G. Sganos,[13] M. D. Shapiro,[16]
N. M. Shaw,[27] Q. Shen,[27] P. F. Shepard,[26] M. Shimojima,[34] M. Shochet,[5] J. Siegrist,[16]
A. Sill,[33] P. Sinervo,[13] P. Singh,[26] J. Skarha,[14] K. Sliwa,[35] F. D. Snider,[14] T. Song,[18]
J. Spalding,[7] T. Speer,[9] P. Sphicas,[17] F. Spinella,[25] M. Spiropulu,[10] L. Spiegel,[7] L. Stanco,[23]
J. Steele,[36] A. Stefanini,[25] K. Strahl,[13] J. Strait,[7] R. Ströhmer,[7a] D. Stuart,[7] G. Sullivan,[5]
A. Soumarokov,[31] K. Sumorok,[17] J. Suzuki,[34] T. Takada,[34] T. Takahashi,[22] T. Takano,[34]
K. Takikawa,[34] N. Tamura,[11] B. Tannenbaum,[20] F. Tartarelli,[25] W. Taylor,[13] P. K. Teng,[31]
Y. Teramoto,[22] S. Tether,[17] D. Theriot,[7] T. L. Thomas,[20] R. Thun,[18] M. Timko,[35]
P. Tipton,[28] A. Titov,[29] S. Tkaczyk,[7] D. Toback,[5] K. Tollefson,[28] A. Tollestrup,[7]
J. F. de Troconiz,[10] S. Truitt,[18] J. Tseng,[14] N. Turini,[25] T. Uchida,[34] N. Uemura,[34]
F. Ukegawa,[24] G. Unal,[24] J. Valls,[7a] S. C. van den Brink,[26] S. Vejcik, III,[18] G. Velev,[25]
R. Vidal,[7] M. Vondracek,[12] D. Vucinic,[17] R. G. Wagner,[1] R. L. Wagner,[7] J. Wahl,[5]
N. B. Wallace,[25] A. M. Walsh,[30] C. Wang,[6] C. H. Wang,[31] J. Wang,[5] M. J. Wang,[31]
Q. F. Wang,[29] A. Warburton,[13] T. Watts,[30] R. Webb,[32] C. Wei,[6] C. Wendt,[36] H. Wenzel,[16]
W. C. Wester, III,[7] A. B. Wicklund,[1] E. Wicklund,[7] R. Wilkinson,[24] H. H. Williams,[24]

126

P. Wilson,[5] B. L. Winer,[21] D. Winn,[18] D. Wolinski,[18] J. Wolinski,[19] S. Worm,[20] X. Wu,[9] J. Wyss,[23] A. Yagil,[7] W. Yao,[16] K. Yasuoka,[34] Y. Ye,[13] G. P. Yeh,[7] P. Yeh,[31] M. Yin,[6] J. Yoh,[7] C. Yosef,[19] T. Yoshida,[22] D. Yovanovitch,[7] I. Yu,[7] L. Yu,[20] J. C. Yun,[7] A. Zanetti,[25] F. Zetti,[25] L. Zhang,[36] W. Zhang,[24] and S. Zucchelli[2]

(CDF Collaboration)

[1] Argonne National Laboratory, Argonne, Illinois 60439

[2] Istituto Nazionale di Fisica Nucleare, University of Bologna, I-40126 Bologna, Italy

[3] Brandeis University, Waltham, Massachusetts 02254

[4] University of California at Los Angeles, Los Angeles, California 90024

[5] University of Chicago, Chicago, Illinois 60637

[6] Duke University, Durham, North Carolina 27708

[7] Fermi National Accelerator Laboratory, Batavia, Illinois 60510

[8] Laboratori Nazionali di Frascati, Istituto Nazionale di Fisica Nucleare, I-00044 Frascati, Italy

[9] University of Geneva, CH-1211 Geneva 4, Switzerland

[10] Harvard University, Cambridge, Massachusetts 02138

[11] Hiroshima University, Higashi-Hiroshima 724, Japan

[12] University of Illinois, Urbana, Illinois 61801

[13] Institute of Particle Physics, McGill University, Montreal H3A 2T8, and University of Toronto, Toronto M5S 1A7, Canada

[14] The Johns Hopkins University, Baltimore, Maryland 21218

[15] National Laboratory for High Energy Physics (KEK), Tsukuba, Ibaraki 305, Japan

[16] Ernest Orlando Lawrence Berkeley National Laboratory, Berkeley, California 94720

[17] Massachusetts Institute of Technology, Cambridge, Massachusetts 02139

[18] University of Michigan, Ann Arbor, Michigan 48109

[19] Michigan State University, East Lansing, Michigan 48824

[20] University of New Mexico, Albuquerque, New Mexico 87131

[21] The Ohio State University, Columbus, OH 43210

[22] Osaka City University, Osaka 588, Japan

[23] Universita di Padova, Istituto Nazionale di Fisica Nucleare, Sezione di Padova, I-35131 Padova, Italy

[24] University of Pennsylvania, Philadelphia, Pennsylvania 19104

[25] Istituto Nazionale di Fisica Nucleare, University and Scuola Normale Superiore of Pisa, I-56100 Pisa, Italy

[26] University of Pittsburgh, Pittsburgh, Pennsylvania 15260

[27] Purdue University, West Lafayette, Indiana 47907

[28] University of Rochester, Rochester, New York 14627

[29] Rockefeller University, New York, New York 10021

[30] Rutgers University, Piscataway, New Jersey 08854

[31] Academia Sinica, Taipei, Taiwan 11529, Republic of China

[32] Texas A&M University, College Station, Texas 77843

[33] Texas Tech University, Lubbock, Texas 79409

[34] University of Tsukuba, Tsukuba, Ibaraki 305, Japan

127

[35] *Tufts University, Medford, Massachusetts 02155*

[36] *University of Wisconsin, Madison, Wisconsin 53706*

[37] *Yale University, New Haven, Connecticut 06511*

128

Bibliography

[1] S.L. Glashow, *Partial Symmetries of Weak Interactions*, Nucl. Phys. **22**, 579 (1961); S. Weinberg, *A Model of Leptons*, Phys. Rev. Lett. **19**, 1264 (1967); A Salam, in *Elementary Particle Theory: Relativistic Groups and Analyticity (Nobel Symposium No. 8)*, edited by N. Svartholm (Almqvist and Wiksell, Sweden, 1968), p.357.

[2] S.L. Glashow, J. Illiopoulos and L. Maiani, *Weak Interactions with Lepton-Hadron Symmetry*, Phys. Rev. D. **2**, 1285 (1970); M. Kobayashi and M. Maskawa, *CP Violation in the Renormalizable Theory of Weak Interaction*, Prog. Theor. Phys. **49**, 652 (1973).

[3] CDF Collaboration, F. Abe *et al.*, *Evidence for Top Quark Production in $\bar{p}p$ Collisions at $\sqrt{s} = 1.8$ Tev*, Phys. Rev. D. **50**, 2966 (1994).

[4] CDF Collaboration, F. Abe *et al.*, *Observation of Top Quark Production in $\bar{p}p$ Collisions*, Phys. Rev. Lett. **74**, 2626 (1995)

[5] ALEPH Collaboration, D. Decamp *et al.*, *Measurement of the Forward-Backward Asymmetry in $Z \rightarrow b\bar{b}$ and $Z \rightarrow c\bar{c}$*, Phys. Lett. **B263**, 325 (1991); DELPHI Collaboration, P. Abreu *et al.*, *A Measurement of the $b\bar{b}$ Forward Backward Asymmetry Using the Semileptonic Decay into Muons*, ibid. **276**, 536 (1992); L3 Collaboration, O. Adriani *et al.*, *Measurement of the $e^+e^- \rightarrow b\bar{b}$ and $e^+e^- \rightarrow c\bar{c}$ Forward Backward Asymmetries at the Z^0 Resonance*, ibid. **292**, 454 (1992).

[6] CLEO Collaboration, P. Avery *et al.*, *Upper Limit on Flavor Changing Neutral Current Decays of the B Quark*, Phys. Rev. Lett. **53**, 1309 (1984); CLEO Collaboration, A.

129

Bean *et al.*, *Improved Upper Limit on Flavor Changing Neutral Current Decays of the B Quark*, Phys. Rev. D. **35**, 3533 (1987).

[7] PEP Collaboration, A. Marini *et al.*, *Search for Exclusive Free Quark Production at PEP*, Phys. Rev. Lett. **48**, 1649 (1982).

[8] PETRA Collaboration, B. Adeva *et al.*, *Search for Top Quark and a Test of Models without Top Quark at the Highest PETRA Energies*, Phys. Rev. Lett. **50**, 799 (1983).

[9] UA1 Collaboration, C. Albajar *et al.*, *Search for New Heavy Quarks at the Cern $p\bar{p}$ Collider*, Z. Phys. **C37**, 505 (1988).

[10] CDF Collaboration, F. Abe *et al.*, *A Lower Limit on the Top Quark Mass from Events with Two Leptons in $p\bar{p}$ Collisions at $\sqrt{s}$ = 1.8 Tev*, Phys. Rev. Lett. **68**, 447 (1992); CDF Collaboration, F. Abe *et al.*, *A Limit on the Top Quark Mass From $p\bar{p}$ Collisions AT $\sqrt{s}$ = 1.8 TeV*, Phys. Rev. D. **45**, 3921 (1992).

[11] D0 Collaboration, S. Abachi *et al.*, *Search for the Top Quark in $p\bar{p}$ Collisions at $\sqrt{s}$ = 1.8 Tev*, Phys. Rev. Lett. **72**, 2138 (1994).

[12] M. Veltman, *Limit on Mass Differences in the Weinberg Model*, Nucl. Phys. **B123**, 89 (1977).

[13] J. M. Benlloch, N. Wainer, and W. T. Giele, *On the Search for the Top Quark in the Hadronic Decay Channel*, Phys. Rev. D. **48**, 5226 (1993).

[14] P. Nason, S. Dawson and R. K. Ellis, *The Total Cross-Section for the Production of Heavy Quarks in Hadronic Collisions*, Nucl. Phys. **B303**, 607 (1988).

[15] E. Laenen, J. Smith, and W. L. van Neerven, *Top Quark Production Cross-Section*, Phys. Lett. **B321**, 254 (1994)

[16] E. L. Berger, H. Contopanagos, *Perturbative Gluon Resummation of the Top Quark Production Cross Section*, Phys. Lett. **B361**, 115 (1995).

[17] S. Catani, M. L. Mangano, P. Nason and L. Trentadue, *The Top Cross-Section in Hadronic Collisions*, CERN-TH/96-21, hep-ph/9602208.

[18] R. K. Ellis and S. Parke, *Top Quark Production by W Gluon Fusion*, Phys. Rev. D. 46, 3785 (1992); D. O. Carlson and C.-P. Yuan, *Studying the Top Quark via the W-Gluon Fusion Process*, Phys. Lett. B306, 386 (1993).

[19] R. R. Wilson, *The Tevatron*, Phys. Today 10, 23 (1977).

[20] The CDF Collaboration, F. Abe *et al.*, *The CDF Detector: An Overview*, Nucl. Inst. and Meth. A271, 387 (1988).

[21] CDF cross sectional view diagram courtesy Randy Keup. Diagram first appeared in published form in reference [3].

[22] D. Amidei, *et al.*, *The Silicon Vertex Detector of the Collider Detector at Fermilab*, Nucl. Inst. and Meth. A350, 73 (1994).

[23] S. Cihangir, *et al.*, *SVX': The New CDF Silicon Vertex Detector*, Nucl. Inst. and Meth. A360, 137 (1995).

[24] F. Bedeschi, *et al.*, *Design and Construction of the CDF Central Tracking Chamber*, Nucl. Inst. and Meth. A268, 50 (1988).

[25] *The CDF Vertex Detector*, internal note in progress, to be submitted to Nucl. Inst. and Meth.

[26] L. Balka, *et al.*, *The CDF Central Electromagnetic Calorimeter*, Nucl. Inst. and Meth. A267 272 (1988).

[27] S. Bertolucci, *et al.*, *The CDF Central and Endwall Hadron Calorimeter*, Nucl. Inst. and Meth. A267 301 (1988).

[28] Y. Fukui, *et al.*, *CDF End Plug Electromagnetic Calorimeter Using Conductive Plastic Proportional Tubes*, Nucl. Inst. and Meth. A267, 280 (1988).

[29] *The CDF End Plug Hadronic Calorimeter*, internal note in progress, to be submitted to Nucl. Inst. and Meth.

[30] G. Brandenburg, *et al.*, *An Electromagnetic Calorimeter for the Small Angle Regions of the Collider Detector at Fermilab*, Nucl. Inst. and Meth. **A267**, 257 (1988).

[31] S. Cihangir, *et al.*, *The CDF Forward/Backward Hadron Calorimeter*, Nucl. Inst. and Meth. **A267**, 249 (1988).

[32] G. Ascoli, *et al.*, *CDF Central Muon Detector*, Nucl. Inst. and Meth. **A268**, 33 (1988).

[33] A. Gauthier, *et al.*, *Design and Performance of Drift Chambers for the Central Muon Upgrade of the CDF Detector*, to be submitted to Nucl. Inst. and Meth. .

[34] D. Amidei, *et al.*, *A Two Level Fastbus Based Trigger System for CDF*, Nucl. Inst. and Meth. **A269**, 51 (1988).

[35] G. Ascoli, *et al.*, *CDF Central Muon Level 1 Trigger Electronics*, Nucl. Inst. and Meth. **A269**, 63 (1988).

[36] W. Badgett, *Measurement of $\sigma \cdot B(W \to \mu\nu)$, $\sigma \cdot B(Z^0 \to \mu^+\mu^-)$ and $R_\mu = \sigma \cdot B(W \to \mu\nu)/\sigma \cdot B(Z^0 \to \mu^+\mu^-)$ and Extraction of $BR(W \to \mu\nu)$ and $\Gamma(W)$ in $p\bar{p}$ Collisions at $\sqrt{s} = 1.8\ TeV$*, Ph.D. thesis, University of Michigan (1994).

[37] G. W. Foster, *et al.*, *A Fast Hardware Track Finder for the CDF Central Tracking Chambers*, Nucl. Inst. and Meth. **A269**, 93 (1988).

[38] J.T. Carrol, *et al.*, *The CDF Level 3 Trigger*, Nucl. Inst. and Meth. **A300**, 552 (1991).

[39] E. Barsoti, *et al.*, *Fastbus Data Acquisition for CDF*, Nucl. Inst. and Meth. **A269**, 82 (1988).

[40] C. Miao, *et al.*, *SVX' Tracking Efficiency Study*, CDF Internal Note 2878, November 1994 (unpublished).

132

[41] K. Byrum *et al.* *Shower Maximum Trigger for Electrons and Photons at CDF*, Nucl. Inst. and Meth. **A364**, 144 (1995).

[42] P. Koehn, *Bottom and Charm Quark Production in Jets from $\bar{p}p$ Collisions at $\sqrt{s} = 1.8\ TeV$*, Ph.D. dissertation, University of Rochester (1996).

[43] C. Peterson *et al.*, *Scaling Violations in Inclusive e^+e^- Annihilation Spectra*, Phys. Rev. D. **27**, 105 (1983).

[44] P. Avery, K. Read, G. Trahern, Cornell Internal Note CSN-212, March 25, 1985, (unpublished).

[45] D. Glenzinski, *Observation of the Top Quark in $\bar{p}p$ Collisions at $\sqrt{s} = 1.8\ TeV$*, Ph.D. dissertation, Johns Hopkins University (1995).

[46] G. Marchesini and B.R. Webber, *Monte Carlo Simulation of General Hard Processes with Coherent QCD Radiation*, Nucl. Phys. **B310**, 461 (1988); G. Marchesini *et al.*, *Herwig: A Monte Carlo Event Generator for Simulating Hadron Emission Reactions with Interfering Gluons. Version 5.1 - April 1991*, Comput. Phys. Comm. **67**, 465 (1992).

[47] D. Buskulic, *et al.*, *A Precise Measurement of $\Gamma(Z \rightarrow b\bar{b})/\Gamma(Z \rightarrow hadrons)$*, Phys. Lett. **B313**, 535 (1993).

[48] CDF Collaboration, F. Abe *et al.*, *Measurement of Correlated $\mu - \bar{b}$ Jet Cross-sections in $\bar{p}p$ Collisions at $\sqrt{s} = 1.8\ TeV$*, Phys. Rev. D. **53**, 1051 (1996)

[49] Y. Cen, *et al.*, *Backgrounds for the SVX b-Tag Top Search: Run 1A + 1B*, CDF Internal Note 2965, Febuary 1996. Results first appeared in published form in reference [4].

[50] G. Unal, *Background Summary for the Top SVX Analysis*, CDF Internal Note 3513, Febuary 1996 (unpublished).

[51] W. Yao, *et al.*, *Top Search in Lepton + Jets with SECVTX*, CDF Internal Note 2989, March 1995 (unpublished).

[52] J. Ohnemus, *An Order α_s Calculation of Hadronic $W^- W^+$ Production*, Phys. Rev. D. **44**, 1403 (1991).

[53] J. Ohnemus, *An Order α_s Calculation of Hadronic $W^{\pm}Z$ Production*, Phys. Rev. D. **44**, 3477 (1991).

[54] C. Campagnari, *Background in the W + Jets Sample*, CDF Internal Note 2476, Febuary 1994 (unpublished).

[55] F. Berends, *et al.*, *On the Production of a W and Jets at Hadron Colliders*, Nucl. Phys. **B357**, 32 (1991).

[56] G. Unal, *$Wb\bar{b}$ and $Wc\bar{c}$ Backgrounds in Top SVX Channel*, CDF Internal Note 3389, October 1995 (unpublished).

[57] T. Stelzer, *et al.*, *Single Top Quark Production via $q\bar{q} \to t\bar{b}$*, Phys. Lett. **B357**, 125 (1995); M. Smith, *et al.*, *QCD and YUKAWA Corrections to Single Top Quark Production via $q\bar{q} \to t\bar{b}$*, hep-ph/9604223, to be published.

[58] CDF Collaboration, F. Abe *et al.*, *Measurement of the $p\bar{p}$ Total Cross Section at $\sqrt{s} = 546$ GeV and 1.8 TeV*, Fermilab Preprint FERMILAB-PUB-93-234-E (Nov 1993); Submitted to Phys. Rev. D.

[59] CDF Collaboration, F. Abe *et al.*, *Measurement of Small Angle $p\bar{p}$ Elastic Scattering at $\sqrt{s} = 546$ GeV and 1.8 TeV*, Fermilab Preprint FERMILAB-PUB-93-232-E (Aug 1993); Submitted to Phys. Rev. D.

[60] CDF Collaboration, F. Abe *et al.*, *Measurement of $p\bar{p}$ Single Diffractive Dissociation at $\sqrt{s} = 546$ GeV and 1.8 TeV*, Fermilab Preprint FERMILAB-PUB-93-233-E (Aug 1993); Submitted to Phys. Rev. D.

134

[61] S. Belforte, *et al.*, σ_{BBC} *Derivation and Results*, CDF Internal Note 2361 (March 1994); σ_{BBC} *Updates*, CDF Internal Note 2535 (April 1994). The normalization is first used in published form in reference [3].

[62] M. Contreras, *et al.*, *Lepton Identification Efficiencies for Top Dilepton Analysis*, CDF Internal Note 2883, Novmember 1994. Results first appeared in published form in reference [4].

[63] CDF Collaboration, F. Abe *et al.*, *The Topology of Three Jet Events in p̄p Collisions at* $\sqrt{s} = 1.8\ TeV$, Phys. Rev. D. **45**, 1448 (1992).

[64] R. Roser, *et al.*, *A Measurement of the Level 3 Trigger Efficiency for t̄t Events*, CDF Internal Note 3442, December 1995 (unpublished); T. Liss, *et al.*, *Muon Trigger Simulation Changes and the W* → $\mu\nu$ *Cross Section*, CDF Internal Note 3931, October 1996 (unpublished).

[65] J. Incandela, *et al.*, *Understanding Btag Efficiency Change from Run1a to Run1b*, CDF Internal Note 3017, Febuary 1995. Results first appeared in published form in reference [4].

[66] D0 Collaboration, S. Abachi, *et al.*, *Observation of Top Quark*, Phys. Rev. Lett. **74**, 2632 (1995)

[67] N. Eddy, *et al.*, *Top Mass Results for Winter '96 Conferences*, CDF Internal Note 3608, May 1996 (to be published).

[68] *Future Electro Weak Physics at the Fermilab Tevatron: Report of the tev_2000 Study Group*, edited by D. Amidei and R. Brock.

[69] CDF Collaboration, F. Abe *et al.*, *Measurement of the Average Lifetime of B Hadrons Produced in p̄p Collisions at* $\sqrt{s} = 1.8\ TeV$, Phys. Lett. **71**, 3421 (1993).

ProQuest

2017 ProQuest Distribution Agreement

This Agreement is between the author (Author) and ProQuest LLC, through its ProQuest Dissertation Distribution business (formerly ProQuest/UMI). Under this Agreement, Author grants ProQuest certain rights to preserve, archive and distribute the dissertation or thesis (the Work), abstract, and index terms provided by Author to ProQuest.

Section I. License for Inclusion of the Work in ProQuest Publishing Program

Grant of Rights. Author hereby grants to ProQuest the **non-exclusive**, worldwide right to reproduce, distribute, display and transmit the Work (in whole or in part) in such tangible and electronic formats as may be in existence now or developed in the future. Author further grants to ProQuest the right to include the abstract, bibliography and other metadata in the ProQuest Dissertations & Theses database (PQDT) and in ProQuest Dissertation Abstracts International and any successor or related index and/or finding products or services.

ProQuest Publishing Program - Election and Elements. The rights granted above shall be exercised according to the publishing option selected by Author in Section III, Author Options, and subject to the following additional Publishing Program requirements:

- Distribution of the Work. Except as restricted by Author in the publishing option selected, the rights granted by Author automatically include (1) the right to allow sale and distribution of the Work, in whole or in part, by ProQuest and its sales agents and distributors and (2) the right to make the Abstract, bibliographic data and any meta data associated with the Work available to search engines and harvesters.

- Restrictions. ProQuest will use commercially reasonable efforts to restrict the distribution of the Work as provided under the publishing option selected by Author or *as later elected by Author* through direct contact with ProQuest. Such election is subject to Author's Degree Granting Institution Directives. With respect to restrictions requested after submission of the Work, Author acknowledges that ProQuest cannot recall or amend previously distributed versions of the Work.

- Removal of Work from the Program. ProQuest may elect not to distribute the Work if it believes that all necessary rights of third parties have not been secured. Refer to the website http://www.proquest.com/products_umi/dissertations/ for information about copyright and your dissertation or thesis. If Author's degree is rescinded, and/or the degree-granting institution so directs, ProQuest will expunge the Work from its publishing program in accordance with its then current publishing policies.

- Degree Granting Institution Directives. Author is solely responsible for any conflict between policies and directions of Author's degree-granting institution, Author's choice of publishing model, and/or any restriction Author places on the use of the Work. For the avoidance of doubt, ProQuest is not responsible for access to the Work that is provided by Author's degree-granting institution through its library or institutional repository. Author must work directly with Author's degree granting institution to ensure application of any restrictions to access relating to the Work by Author's degree granting institution.

Delivery of the Work. Author shall provide to ProQuest the Work and all necessary supporting documents during the online submission process, according to the Instructions accompanying this agreement.

Rights Verification. Author represents and warrants that Author is the copyright holder of the Work and has obtained all necessary rights to permit ProQuest to reproduce and distribute third party materials contained in any part of the Work, including all necessary licenses for any non-public, third party software necessary to access, display, and run or print the Work. Author is solely responsible and will indemnify ProQuest for any third party claims related to the Work as submitted for publication.

Open Access Publishing Plus

☐ I want the broadest possible dissemination of my work, and I want to provide free global access to the electronic copy of my work via the internet.

☑ I understand that I will not be eligible to receive royalties.

I want major search engines (e.g. Google, Yahoo) to discover my work. Learn more: http://www.proquest.com/en-US/products/dissertations/google.shtml

☐ Yes
☐ No

Acknowledgment: I have read, understand and agree to this ProQuest Publishing Agreement, including all rights and restrictions included within the publishing option chosen by me as indicated above.

REQUIRED Author's signature _____ Date _7/25/2017_

(Print Name) _Chyi-Chang Miso_

Institution conferring degree _University of Michigan_

This page must accompany your manuscript and the rest of the submission materials

Please check type of manuscript:

___ M (Master's Thesis)

___ D (Dissertation)

Dissertation/Master's Thesis Submission Form
Please print clearly in block letters

Personal Information

Last Name	Miao	Middle Name or Initial	
First Name	Chyi	Country (ies) of Citizenship	US
	Chang		

Degree & Dissertation Information

Title of Dissertation/ Thesis	Measurement of the ttbar production cross section in the lepton plus jets channel in ppbar collisions at sqrt(s) = 1.9 Tev		
Institution conferring degree	The University of Michigan	Degree awarded (abbreviate; e.g., Ph.D.)	Ph.D.
College, School, or Division		Year degree awarded	1997
Department or Program	Physics	Year manuscript completed	1997
Advisor/Committee Chair	Professor I. Wehrley chapman		
Committee Member	Professor Dante Amidei	Committee Member	Professor timothy Chupp
Committee Member	Professor Douglas O. Richstone	Committee Member	Professor York-Peng E. Yan

Committee Member _____ Committee Member _____

Language of manuscript _____ English _____

Primary Subject Category: Enter the 4-digit code and category name from the Subject Category Guide that most closely describes the area of your research. Code __0605__ Category _____ Physics _____

You may suggest two additional subject categories that may aid in the discovery of your work in our digital database.

Category _____ Particle
Code _____ physics _____ Code _____ Category _____

Provide up to 6 keywords or short phrases for citation indices, library cataloging, and database searching.

_____ _____ _____

_____ _____ _____

Current Contact Information Current Email Address _____

Street Address _____

Please provide your postal address if you are interested in receiving royalties on sales of your thesis.

City _____ Province _____ Daytime Phone _____

Country _____ Postal Code _____ Evening Phone _____

Permanent Contact Information Permanent Email Address _____

Street Address (line 1) _____

City _____ Province _____ Future Phone _____

Country _____ Postal Code _____ Alternate Future Phone _____

THIS PAGE MUST ACCOMPANY YOUR MANUSCRIPT AND THE REST OF YOUR SUBMISSION MATERIALS

Subject Categories

The ProQuest Dissertations & Theses (PQDT) database and the ProQuest citation indices are arranged by subject categories. Please select the one category below that best describes your field of research or creative work. You may add one or two additional categories on your submission form that will also be associated with your work as secondary subjects.

Arts, Business, Education, Humanities, and Social Sciences

AREA, ETHNIC, AND GENDER STUDIES

African American studies	0296
African studies	0293
American studies	0323
Asian American studies	0343
Asian studies	0342
Baltic studies	0361
Black studies	0325
Canadian studies	0385
Caribbean studies	0432
Classical studies	0434
East European studies	0437
Ethnic studies	0631
European studies	0440
French Canadian culture	0482
Gender studies	0733
GLBT studies	0492
Hispanic American studies	0737

Holocaust studies	0507
Islamic culture	0512
Judaic studies	0751
Latin American studies	0550
Middle Eastern studies	0555
Native American studies	0740
Near Eastern studies	0559
North African studies	0560
Pacific Rim studies	0561
Regional studies	0604
Scandinavian studies	0613
Slavic studies	0614
South African studies	0654
South Asian studies	0638
Sub Saharan Africa studies	0639
Women's studies	0453

BUSINESS

Accounting	0272
Arts management	0424
Banking	0770
Business	0310
Entrepreneurship	0429
Finance	0508
Management	0454
Marketing	0338
Sports management	0430

COMMUNICATIONS AND INFORMATION SCIENCES

Communication	0459
Information science	0723
Journalism	0391
Library science	0399
Mass communication	0708
Technical communication	0643

Web studies   0646

FINE AND PERFORMING ARTS
Art criticism	0365
Art history	0377
Cinematography	0435
Dance	0378
Design	0389
Film studies	0900
Fine arts	0357
Music	0413
Performing arts	0641
Theater	0465
Theater history	0644

EDUCATION
Adult education	0516
Art education	0273
Bilingual education	0282
Business education	0688
Community college education	0275
Continuing education	0651
Curriculum development	0727
Early childhood education	0518
Education	0515
Education finance	0277
Education policy	0458
Educational administration	0514
Educational evaluation	0443
Educational leadership	0449
Educational psychology	0525
Educational technology	0710
Educational tests & measurements	0288
Elementary education	0524
English as a second language	0441
Foreign language instruction	0444
Gifted education	0445
Health education	0680
Higher education	0745
Higher education administration	0446
History of education	0520
Home economics education	0278
Industrial arts education	0521
Instructional design	0447
Language arts	0279
Mathematics education	0280
Middle school education	0450
Multicultural education	0455
Music education	0522
Pedagogy	0456
Performing arts education	0457
Philosophy of education	0998
Physical education	0523
Reading instruction	0535
Religious education	0527
School counseling	0519
Science education	0714
Secondary education	0533
Social sciences education	0534
Sociology of education	0340
Special education	0529
Teacher education	0530
Vocational education	0747

HUMANITIES

HISTORY
African history	0331
American history	0337
Ancient history	0579
Asian history	0332
Black history	0328
Canadian history	0334
European history	0335
History	0578
History of Oceania	0504
History of science	0585
Latin American history	0336
Medieval history	0581
Middle Eastern history	0333
Military history	0772
Modern history	0582
Russian history	0724
World history	0506

LANGUAGE & LITERATURE
African literature	0316
American literature	0591
Ancient languages	0289
Asian literature	0305
British and Irish literature	0593
Canadian literature	0352
Caribbean literature	0360
Classical literature	0294
Comparative literature	0295
English literature	0593
French Canadian literature	0355
Germanic literature	0311
Icelandic & Scandinavian literature	0362
Language	0679
Latin American literature	0312
Linguistics	0290
Literature	0401
Literature of Oceania	0356
Medieval literature	0297
Middle Eastern literature	0315
Modern language	0291
Modern literature	0298
Rhetoric	0681
Romance literature	0313
Slavic literature	0314

PHILOSOPHY AND RELIGION
Aesthetics	0650
Biblical studies	0321
Canon law	0375
Clerical studies	0319
Comparative religion	0618
Divinity	0376
Epistemology	0393
Ethics	0394
Logic	0395
Metaphysics	0396
Pastoral counseling	0397
Philosophy	0422
Philosophy of Religion	0322
Philosophy of science	0402
Religion	0318
Religious history	0320
Spirituality	0647
Theology	0469